République Algérienne Démocratique et Populaire

Ministère de l'Enseignement Supérieur et de La Recherche Scientifique

École Nationale Polytechnique

المدرسة الوطنية المتعددة التقنيات
Ecole Nationale Polytechnique

L G M D

Département de Génie Mécanique

Laboratory of Green and Mechanical Development -LGMD

Thesis submitted to the Department of
Mechanical Engineering
in partial fulfillment of the requirements for the degree of
Doctor in Mechanical Engineering
Major: Clean and Renewable Energies

Aerodynamic investigations of H-type vertical axis wind turbines

Presented by

Samir Ouchene

Defended on April 25, 2024, in front of a jury composed of:

Chair	Saïd Rechak	Professor, ENP, Algiers, Algeria
Supervisor	Arezki Smaili	Professor, ENP, Algiers, Algeria
Co-supervisor	Hachimi Fellouah	Professor, Université de Sherbrooke, Canada
Examiner	Samir Hanchi	Professor, USTHB, Algiers, Algeria
Examiner	Mahmoud Mekadem	Associate Professor, EMP, Algiers, Algeria
Examiner	Abdelhamid Bouhelal	Associate Professor, ENP, Algiers, Algeria
Invited	Sofiane Khelladi	Professor, ENSAM, Paris, France
Invited	Ali Benmeddour	Research Director, NRC, Canada
Invited	Ahmed Bekhti	Research Associate, CDER, Algiers, Algeria

ENP 2024

République Algérienne Démocratique et Populaire

Ministère de l'Enseignement Supérieur et de La Recherche Scientifique

École Nationale Polytechnique

المدرسة الوطنية المتعددة التقنيات
Ecole Nationale Polytechnique

L G M D

Département de Génie Mécanique

Laboratory of Green and Mechanical Development -LGMD

Thesis submitted to the Department of
Mechanical Engineering
in partial fulfillment of the requirements for the degree of
Doctor in Mechanical Engineering
Major: Clean and Renewable Energies

Aerodynamic investigations of H-type vertical axis wind turbines

Presented by

Samir Ouchene

Defended on April 25, 2024, in front of a jury composed of:

Chair	Saïd Rechak	Professor, ENP, Algiers, Algeria
Supervisor	Arezki Smaili	Professor, ENP, Algiers, Algeria
Co-supervisor	Hachimi Fellouah	Professor, Université de Sherbrooke, Canada
Examiner	Samir Hanchi	Professor, USTHB, Algiers, Algeria
Examiner	Mahmoud Mekadem	Associate Professor, EMP, Algiers, Algeria
Examiner	Abdelhamid Bouhelal	Associate Professor, ENP, Algiers, Algeria
Invited	Sofiane Khelladi	Professor, ENSAM, Paris, France
Invited	Ali Benmeddour	Research Director, NRC, Canada
Invited	Ahmed Bekhti	Research Associate, CDER, Algiers, Algeria

ENP 2024

République Algérienne Démocratique et Populaire

Ministère de l'Enseignement Supérieur et de La Recherche Scientifique

École Nationale Polytechnique

المدرسة الوطنية المتعددة التقنيات
Ecole Nationale Polytechnique

Département de Génie Mécanique

Laboratory of Green and Mechanical Development -LGMD

Thèse soumise au Département de
Génie Mécanique
En vue de l'obtention du grade de
Docteur en Génie Mécanique
Spécialité: Énergies Propres et Renouvelables

Études Aérodynamiques des éoliennes à axe vertical de type H

Présentée par

Samir Ouchene

Soutenue le 25 avril 2024 devant le jury composé de:

Président	Saïd Rechak	Professeur, ENP, Alger, Algérie
Directeur	Arezki Smaili	Professeur, ENP, Alger, Algérie
Co-directeur	Hachimi Fellouah	Professeur, Université de Sherbrooke, Canada
Examinateur	Samir Hanchi	Professeur, USTHB, Alger, Algérie
Examinateur	Mahmoud Mekadem	MCA, EMP, Alger, Algérie
Examinateur	Abdelhamid Bouhelal	MCA, ENP, Alger, Algérie
Invité	Sofiane Khelladi	Professeur, ENSAM, Paris, France
Invité	Ali Benmeddour	Directeur de Recherche, NRC, Canada
Invité	Ahmed Bekhti	Chercheur associé, CDER, Alger, Algérie

ENP 2024

ملخص:

تحظى توربينات الرياح ذات المحور العمودي وخاصة من نوع داريوس، باهتمام متزايد في السنوات الأخيرة كبديل قابل للتطبيق لإنتاج الطاقة. ومع ذلك، فإن التعقيدات الديناميكية الهوائية لهذه الأجهزة، وخاصة عند نسب سرعة الطرف المنخفضة حيث يكون للتوقف الديناميكي تأثير ملحوظ على الأداء، تقدم تحديات مستمرة. تساهم هذه الأطروحة في المجال من خلال مزيج من التحقيقات العددية والتجريبية المركزة على توربين VAWT من نوع H. يتم تنظيم البحث في ثلاث دراسات رئيسية، كل منها يستهدف جانبًا محددًا من الديناميكا الهوائية للتوربينات. تهدف الدراسة الأولى إلى تحديد أنسب نموذج اضطراب Reynolds-Averaged Navier-Stokes (URANS) ضمن إطار OpenFOAM، وتشمل تحليلًا مقارنًا لثلاثة نماذج اضطراب في ظل ظروف التوقف الديناميكي العميق. تركز الدراسة الثانية على تقدير الزاوية والسرعة النسبية لشفرات التوربين باستخدام بيانات ديناميكا السوائل الحسابية، من خلال تطبيق طريقتين داخل OpenFOAM وتطبيقهما في محاكاة URANS ثنائية الأبعاد مقترنة بنماذج SST k-ω ونموذج اضطراب المكونة من أربع معادلات. تدرس الدراسة الثالثة أثر توربين VAWT من نوع H صغير، من خلال دمج المحاكاة العددية باستخدام نماذج توربينات متنوعة في OpenFOAM مع تقنية (PIV) التجريبية لفحص السرعة في أثر التوربين. بشكل عام، تهدف هذه الأطروحة إلى تحسين فهم وأداء الديناميكا الهوائية لـ VAWTs من خلال طرق عددية مفصلة ونهج تجريبية، معالجة القضايا الرئيسية في تشغيلها.

الكلمات المفتاحية: ميكانيك الموائع الرقمية، التوقف الديناميكي، برنامج OpenFOAM، توربينات رياح بمحور عمودي ، مقياس سرعة الجسيمات بالصور، نمذجة اضطرابات الجريان.

Résumé:

Les éoliennes à axe vertical, en particulier le type Darrieus, ont gagné une attention significative ces dernières années comme une alternative viable pour la production d'énergie. Cependant, les complexités aérodynamiques de ces dispositifs, surtout à de faibles rapports de vitesse spécifiques où le décrochage dynamique a un impact notable sur la performance, présentent des défis continus. Cette thèse contribue au domaine à travers une combinaison d'investigations numériques et expérimentales centrées sur une éolienne de type H. La recherche est organisée en trois études principales, chacune ciblant un aspect distinct de l'aérodynamique des éoliennes. La première étude vise à identifier le modèle de turbulence URANS le plus approprié sous OpenFOAM, impliquant une analyse comparative de trois modèles de turbulence dans des conditions de décrochage dynamique profond. La deuxième étude se concentre sur l'estimation de l'angle d'attaque (AoA) et de la vitesse relative des pales des éoliennes en utilisant des données de dynamique des fluides numérique, mettant en œuvre deux méthodes au sein d'OpenFOAM et appliquées dans des simulations URANS 2D couplées avec les modèles k-ω SST et de transition à

quatre équations. La troisième étude examine le sillage d'une petite éolienne de type H, combinant des simulations numériques utilisant divers modèles de turbulence dans OpenFOAM avec la vélocimétrie par images de particules (PIV) expérimentale pour étudier le déficit de vitesse dans le sillage de l'éolienne. Dans l'ensemble, cette thèse vise à améliorer la compréhension et la performance aérodynamique des éoliennes à travers une analyse numérique approfondie et une approche expérimentale, abordant des problèmes critiques dans leur fonctionnement.

Mots-clés: Décrochage Dynamique; Eolienne à axe vertical; CFD ; Equations de Navier-Stokes ; Modélisation de la turbulence ; Sillage ; Essais en soufflerie.

Abstract:

Vertical Axis Wind Turbines (VAWTs), especially the Darrieus type, have gained significant attention in recent years as a viable alternative for energy production. However, the aerodynamic complexities of these devices, particularly at low tip speed ratios where dynamic stall has a notable impact on performance, present ongoing challenges. This thesis contributes to the field through a combination of numerical and experimental investigations focused on an H-type VAWT. The research is organized into three main studies, each targeting a distinct aspect of VAWT aerodynamics. The first study aims to identify the most suitable Unsteady Reynolds-Averaged Navier-Stokes (URANS) turbulence model within the OpenFOAM Framework, involving a comparative analysis of three turbulence models under conditions of deep dynamic stall. The second study focuses on estimating the angle of attack (AoA) and relative velocity of VAWT blades using computational fluid dynamics data, implementing two methods within OpenFOAM, and applied in 2D URANS simulations coupled with k-ω SST and the four-equation transition models. The third study examines the wake of a small H-type VAWT, combining numerical simulations using various turbulence models in OpenFOAM with experimental Particle Image Velocimetry (PIV) to investigate the velocity deficit in the turbine's wake. Overall, this thesis aims to improve the understanding and aerodynamic performance of VAWTs through detailed numerical analysis and experimental approach, addressing critical issues in their operation.

Keywords: Dynamic Stall; Vertical Axis Wind Turbines; Computational Fluid Dynamics; Navier-Stokes equations; Turbulence Modeling; Wake; Wind tunnel testing.

Acknowledgments

I would like to express my sincere gratitude to my thesis supervisor, Pr. Arezki Smaili (Professor, Ecole Nationale Polytechnique, Algiers) for his consistent support, availability, and guidance. His patience and efforts in guiding my project have been necessary for its development. I truly appreciate the time he invested in my project.

I am also deeply grateful to my thesis co-supervisor, Pr. Hachimi Fellouah (Professor, Université de Sherbrooke, Canada) for his helpful guidance, availability, and consistent support. His insightful contributions and facilitation of access to computational resources via Digital Research Alliance of Canada have been fundamental to my project progress.

I am grateful to the examination committee, especially the chair, Pr. Said Rechak and the examiners, Pr. Samir Hanchi, Dr. Mahmoud Mekadem, Dr. Abdelhamid Bouhelal, Pr. Sofiane Khelladi, Dr. Ali Benmeddour, and Dr. Ahmed Bekhti for taking the time to review my work and providing constructive feedback.

This research benefited from the computational resources provided by the Digital Research Alliance of Canada (formerly Compute Canada) and Calcul Québec. I am thankful for these facilities, which were indispensable for the completion of the numerical simulations of my thesis.

I would also like to thank Dr. Fawaz Massouh and Pr. Khelladi Sofiane for hosting me during my internship at ENSAM, Paris, and I thank Dr. Ivan Dobrev for his help with the PIV measurements.

I want to extend my thanks to both current and former PhD candidates at ENP with whom I had the opportunity to interact. Special thanks to A. Madjid, M.M. Amokrane, B. Zakaria, M. Ammar, and K. Hamdani.

Finally, I am deeply grateful to my parents and my wife for their enduring encouragement and support. I also wish to thank my friends and everyone who has contributed to my research with their help or encouragement.

TABLE OF CONTENTS

List of Tables

List of Figures

Nomenclature

Latin letters

a	Induction factor, [-]
A	Turbine swept area, $h \cdot d$ [m^2]
AR	Turbine Aspect ratio, h/d [-]
c	Airfoil chord length, [m]
C_d	Drag coefficient, [-]
$C_{d,\max}$	Maximum drag coefficient, [-]
$C_{d,\min}$	Minimum drag coefficient, [-]
C_l	Lift coefficient, [-]
$C_{l,\max}$	Maximum lift coefficient, [-]
$C_{l,\min}$	Minimum lift coefficient, [-]
C_m	Pitching moment coefficient, [-]
C_P	Power coefficient, [-]
C_q	Blade torque coefficient, [-]
d	Diameter of the rotor, [m]
$\vec{e}_x$	Unit vector in the x-direction, [-]
$\vec{e}_y$	Unit vector in the y-direction, [-]
$\vec{e}_z$	Unit vector in the z-direction, [-]
E	Specific total energy, [$J \cdot kg^{-1}$]
$\vec{F}$	Inviscid flux vector
$\vec{F}^V$	Viscous flux vector
F_d	Drag force, [N]
F_l	Lift force, [N]
h	Blade height, [m]
H	Specific total enthalpy, [$J \cdot kg^{-1}$]
k	Turbulence kinetic energy, [$m^2 \cdot s^{-2}$]
Ma	Mach number, [-]
N	Number of blades, [-]
N_{crit}	Amplification factor of the e^N method, [-]
p	Pressure, [N m^{-2}]
Pr_t	Turbulent Prandtl number, [-]

q^{turb}	Turbulent heat flux vector, [W·kg·m^{-2}]
R	Turbine Radius, [m]
Re_c	Chord-based Reynolds number, [-]
t	Time, [s]
T	Temperature, [K]
TI	Freestream turbulence intensity, [-]
u	x-component of the velocity vector, [m·s^{-1}].
v	y-component of the velocity vector, [m·s^{-1}]
U	Local velocity, [m·s^{-1}]
$U_{\text{d},i}$	Downstream velocity in the i^{th} streamtube, [m·s^{-1}]
$U_{\text{e},i}$	Equilibrium velocity in the i^{th} streamtube, [m·s^{-1}]
$U_{\text{u},i}$	Upstream velocity in the i^{th} streamtube, [m·s^{-1}]
U_{w}	Wake velocity, [m·s^{-1}]
$U_{\text{w},i}$	Wake velocity in the ith streamtube, [m·s^{-1}]
U_{∞}	Freestream velocity, [m·s^{-1}]
U_{rel}	Relative velocity, [m·s^{-1}]
$\vec{u}_{\text{m}}$	Mesh velocity, [m·s^{-1}]
$\vec{W}$	Vector of conservative variables
y^+	Dimensionless wall distance, [-]

Greek letters

α	Angle of attack, [°]
α_1	Oscillation amplitude, [°]
α_m	Mean angle of attack, [°]
α_{geo}	Geometrically-derived angle of attack, [°]
α_{DS}	Dynamic stall angle of attack, [°]
α_{ss}	Static stall angle of attack, [°]
β	Blade pitch angle, [°]
Γ	Vortex strength, [m^3·s^{-1}]
δ_{ij}	Kronecker delta
ε	Dissipation rate of turbulence kinetic energy, [m^2·s^{-3}]
θ	Azimuthal angle, [°]
κ	Reduced frequency, [-]

λ	Tip speed ratio, [-]
μ	Dynamic viscosity, [kg m^{-1} s^{-1}]
μ_t	Turbulent/eddy viscosity, [kg m^{-1} s^{-1}]
ν	Kinematic viscosity, [$m^2 \cdot s^{-1}$]
ρ	Fluid density, [$kg \cdot m^{-3}$]
σ	Turbine solidity, (Nc/d), [-]
τ_{ij}	Viscous stress tensor, [$kg \cdot m^{-1} \cdot s^{-2}$]
τ_{ij}^R	Reynolds stress tensor, [$kg \cdot m^{-1} \cdot s^{-2}$]
ω	Specific dissipation rate of turbulence kinetic energy, [s^{-1}]
ω_z	z-component of the vorticity, [s^{-1}]
Ω	Rotational speed, [$rad \cdot s^{-1}$]

List of Abbreviations

2D	Two-Dimensional
3D	Three-Dimensional
AoA	Angle of Attack
BEM	Blade Element Momentum
CFD	Computational Fluid Dynamics
DES	Detached Eddy Simulation
DMST	Double-Multiple Streamtube
DSV	Dynamic Stall Vortex
HAWT	Horizontal Axis Wind Turbine
LES	Large Eddy Simulation
LEV	Leading edge Vortex
MST	Multiple Streamtube
NACA	National Advisory Committee for Aeronautics
PIV	Particle Image Velocimetry
SB-VAWT	Straight-Blade Vertical Axis Wind Turbine
SCL	Space Conservation Law
TEV	Trailing Edge Vortex
TSR	Tip Speed Ratio
URANS	Unsteady Reynolds-Averaged Navier-Stokes
VAWT	Vertical Axis Wind Turbine
VSM	Viscous Sublayer Model

Introduction

In recent years, the demand for energy worldwide has grown significantly due to factors like population growth, industrial development, and modern living standards. Historically, this demand has been met mainly by fossil fuels such as coal, oil, and natural gas. However, the use of these non-renewable resources has led to serious environmental problems, including the increase of greenhouse gas emissions, which contribute to climate change. The need to address these environmental issues has highlighted the importance of renewable energy sources.

According to the International Energy Agency (IEA) [1], investment in clean energy technologies is growing much faster than spending on fossil fuels. This shift is propelled by both the lower cost and increased reliability of clean energy, which have become particularly important given the challenges posed by the global energy crisis. In 2022, global primary energy consumption amounted to 1833 TWh, up 1.1% from 2021. This increase in demand was driven by emerging economies. Global energy-related CO_2 emissions continued to rebound strongly, reaching a record high of 39.3 billion tonnes of carbon dioxide equivalent, representing a 0.8% increase over 2021. Emissions from energy consumption contributed 87% of global emissions [2].

In response to this growth in energy demand, it is important to explore new locations to capture energy. This has led to the emergence of new market segments, of which wind power is a key asset for the energy transition. By harnessing the power of the wind to generate electricity, this energy source significantly contributes to diversifying the energy mix. According to the Global Wind Energy Council (GWEC) [3], 117 GW of new wind power capacity was installed worldwide in 2023, bringing total installed wind capacity to 1021 GW, a growth of 13% compared with 2022. Moreover, 2022 marked a record year for new onshore wind installations, exceeding 100 GW, and achieved the second highest level for offshore wind installations at 11 GW.

Vertical Axis Wind Turbines (VAWTs) (Figure 1a) represent a promising segment of wind energy technology, distinct from their counterpart, Horizontal Axis Wind Turbines (HAWTs) (Figure 1b). The primary distinction lies in the orientation of the rotor axis. VAWTs have their rotor axis oriented perpendicular to the incoming flow, while HAWTs, in contrast, have

axes of rotation aligned parallel to the incoming flow. Another classification of wind turbines is based on the primary driving force, which can be either lift or drag (Figure 2).

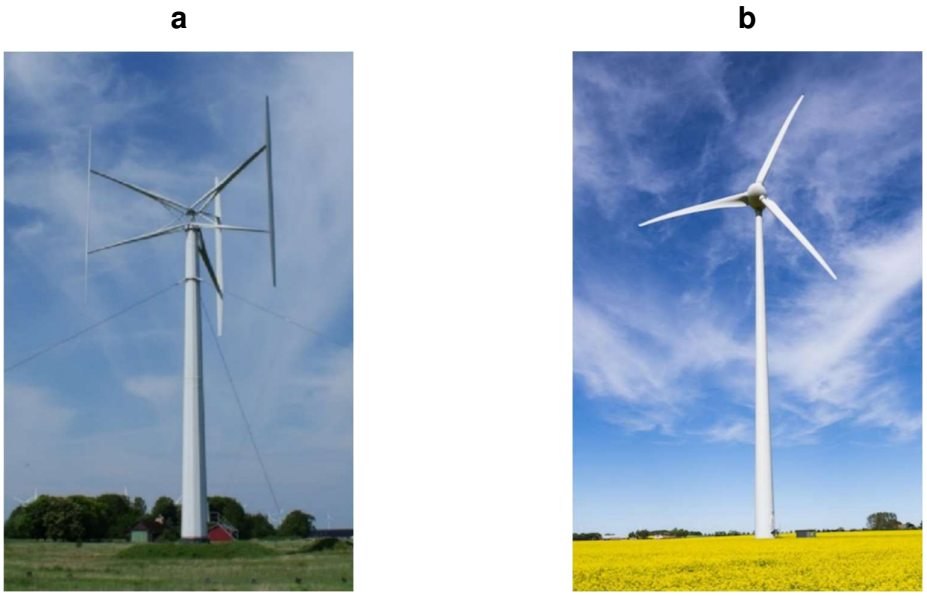

Figure 1: Wind Turbines: (**a**) Vertical Axis Wind Turbine [4], (**b**) Horizontal Axis Wind Turbine.

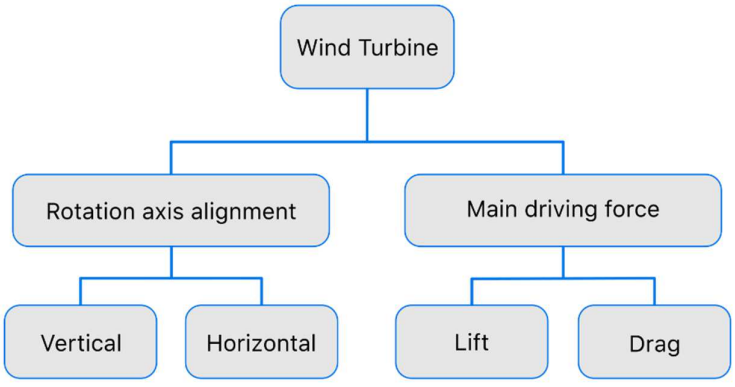

Figure 2: Classification of Wind Turbines.

While HAWTs have traditionally dominated the wind energy market due to their efficiency and mature technology, VAWTs offer distinct advantages that deserve comprehensive investigation. VAWTs eliminate the need for a yaw mechanism, as they can accept wind from any direction, reducing mechanical complexity and potential failure points. They tend to have

a lower center of gravity, which contributes to increased stability and potentially lower installation and maintenance costs. Additionally, they have been found to exhibit higher efficiency in highly turbulent winds, suggesting that VAWTs are well-suited for wind sites characterized by such conditions [5–7]. From an environmental perspective, VAWTs have been preferred in certain project developments to minimize wildlife impacts, especially on avian species [8].

VAWTs also demonstrate increased performance in skewed flows [9], which are common in built environments. The potential for lower manufacturing costs is another advantage; if VAWTs employ simpler straight blades of constant cross-section, they could be more economical to produce than the blades of equivalent HAWTs. Additionally, VAWTs typically operate at lower tip speed ratios, leading to reduced aerodynamic noise, which is beneficial for urban applications and contributes to less acoustic disturbance [10].

Another potential advantage of VAWTs is their operational flexibility in proximity to one another. Due to their ability to harness energy from the vortices shed by upwind turbines, VAWTs can be installed closer together than HAWTs, potentially leading to a considerably higher site power density [11].

Despite these advantages, the aerodynamic behavior of VAWTs is complex and presents challenges that are distinct from those encountered with HAWTs. Critical aerodynamic phenomena associated with VAWTs include dynamic stall and blade-wake interactions, which significantly impact the performance of these turbines. Understanding and addressing these aerodynamic challenges requires a rigorous and systematic approach. Research in this field aims to clarify the underlying aerodynamic mechanisms, develop accurate and reliable models for predicting aerodynamic performance, and propose solutions to improve the efficiency and reliability of VAWTs. This advances wind energy technology and promotes the widespread adoption of VAWTs in various applications. Ultimately, this will enhance the overall contribution of wind energy to the renewable energy industry.

The research presented in this thesis is divided into three main studies, each focusing on different aspects of aerodynamic analysis of VAWTs. These studies are interrelated and build upon each other.

In the first study, the objective is to identify a suitable Reynolds-Averaged Navier-Stokes (RANS) turbulence model within the OpenFOAM Framework for the analysis of the dynamic stall phenomenon of a NACA0015 airfoil undergoing sinusoidal oscillations. The

methodology employed involves conducting numerical simulations using OpenFOAM to evaluate three turbulence models, namely the Launder Sharma k-ε, Spalart-Allmaras, and k-ω SST under deep dynamic stall conditions assuming a fully turbulent boundary layer.

The second study aims to investigate the problem of estimating the angle of attack (AoA) and relative velocity for VAWT blades from computational fluid dynamics (CFD) data. Two methods are implemented as function objects within the OpenFOAM framework for estimating the blade's AoA and relative velocity. For the numerical analysis of the flow around and through the VAWT, 2D Unsteady Reynolds-averaged Navier–Stokes (URANS) simulations are carried out employing two turbulence models: k-ω SST and the γ-Re_θ k-ω SST. The latter considers the laminar-to-turbulent transition.

In the third study, the focus is on investigating the wake of a small H-type VAWT using both numerical simulations and Particle Image Velocimetry (PIV). The numerical analysis is conducted using OpenFOAM employing the k-ω SST, γ-Re_θ k-ω SST, and the Spalart-Allmaras turbulence models. This numerical analysis is complemented by experimental PIV to provide a velocity deficit in the wake of the VAWT.

This research enhances understanding of VAWT aerodynamics and identifies limitations in current modeling approaches, setting the stage for future studies. It lays the groundwork for advanced aerodynamic analysis and potential performance optimization of VAWTs in subsequent research.

The thesis is divided into four chapters, which are outlined below:

Chapter 1 presents a literature review of the main modeling approaches for the aerodynamic analysis of VAWTs, as well as the different relevant unsteady aerodynamic phenomena.

Chapter 2 details the governing equations and the turbulence models used in this thesis. The governing equations in the Arbitrary Lagrangian Eulerian (ALE) Framework are presented together with the URANS formulation of these equations. It then presents the different eddy viscosity turbulence models that are utilized in conjunction with the URANS approach.

Chapter 3 consists of three distinct parts. The first part evaluates fully turbulent eddy viscosity models in the context of predicting deep dynamic stall. The second part focuses on estimating the angle of attack and relative velocity from CFD computations. The third part characterizes the wake of small VAWTs using a combination of numerical computations and experimental data from Particle Image Velocimetry (PIV).

Chapter 4 presents a detailed discussion and analysis of the results from the studies conducted in Chapter 3.

Finally, the main conclusions of this study are presented, and recommendations for future work are provided.

Chapter 1

Literature Review

1.1 Background

Vertical axis wind turbines (VAWTs) are broadly categorized into two types: Darrieus and Savonius. The Darrieus variant exploits the lift force generated by the profiled blades for energy production. In contrast, the Savonius type relies on drag as its principal driving force. Like all drag-based devices, Savonius turbines have a lower tip speed ratio, rendering them less efficient for electricity generation when compared to higher tip speed ratio devices [12]. Within these categories, Darrieus turbines are further divided into straight-blade, curved-blade, and helical-blade models. Similarly, Savonius turbines are available in straight-blade and helical-blade designs, as illustrated in Figure 1.1. For clarity, in the subsequent sections, the acronym "VAWT" will be specifically used to refer to the Darrieus type, particularly the straight-blade VAWTs (SB-VAWTs), also known as H-type VAWT.

The development of VAWTs has seen phases of both progress and stagnation. Initially, the VAWT technology remained largely unexplored until the late 1960s. The first exploratory experiments on the Darrieus turbine were conducted at the National Research Council (NRC) of Canada in 1972, aiming to understand the turbine's fundamental operating principles. The 1970s and 1980s witnessed considerable support and development for VAWTs. Numerous curved-bladed VAWTs were tested, and concurrently, the technology was also developed separately in the UK with straight-bladed designs. These advancements led to the development of commercial turbines, such as those by FloWind, which successfully installed over 500 vertical-axis turbines in California. By 1987, these installations had a combined capacity of approximately 90 MW. Despite this initial progress, the 1990s experienced a considerable decline in interest in VAWTs. While the shift in focus toward HAWTs, which were deemed more competitive, contributed to this decline, limited understanding of blade fatigue properties also played a significant role [13].

The mid-2000s witnessed a renewed interest in multi-megawatt VAWTs, sparked by the high energy cost and the unique design challenges faced by floating offshore HAWT systems. The need for floating foundations in offshore environments highlighted the advantages of VAWTs over HAWTs. This resurgence has been fueled by technological advancements in composite materials, a better understanding of fatigue loads, and developments in floating substructures and control strategies. Despite this progress, the development of floating VAWTs remains in its infancy, with several different concepts being proposed by various research organizations.

The DeepWind consortium, for instance, has been working on a novel 5 MW floating VAWT, aiming to reduce the cost of offshore wind energy generation [13].

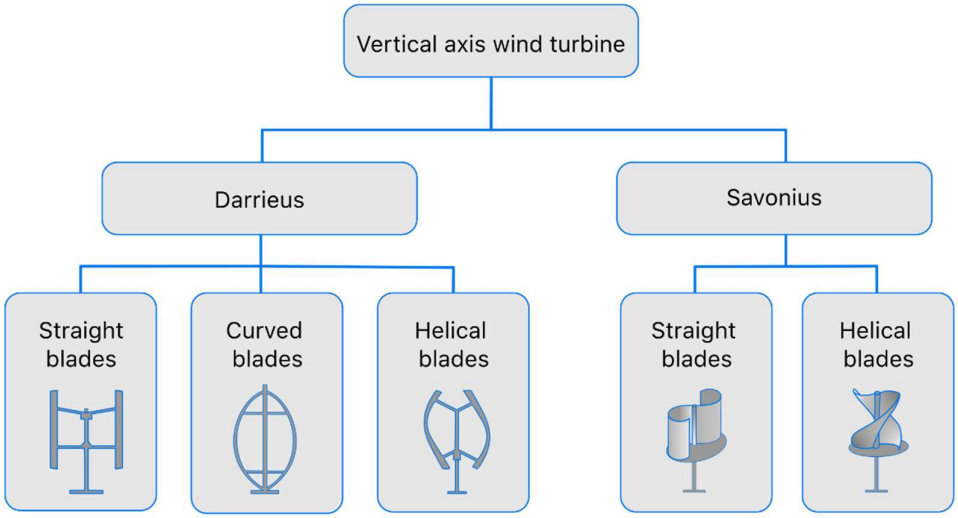

Figure 1.1: Classification of vertical-axis wind turbines.

Figure 1.2 presents a chronological overview of the development of VAWTs with capacities over 100 kW. It includes experimental turbines, prototypes, and commercially produced models. The figure highlights two key periods of VAWT advancements: the first from the 1980s to the 1990s and the second from the mid-2000s to the present. Additionally, the figure shows how the geographical focus of these developments has changed over time. It also demonstrates a renewed interest in the H-type design, which is in contrast to the previous preference for the Φ-rotor design (i.e., with curved blades) [14–16].

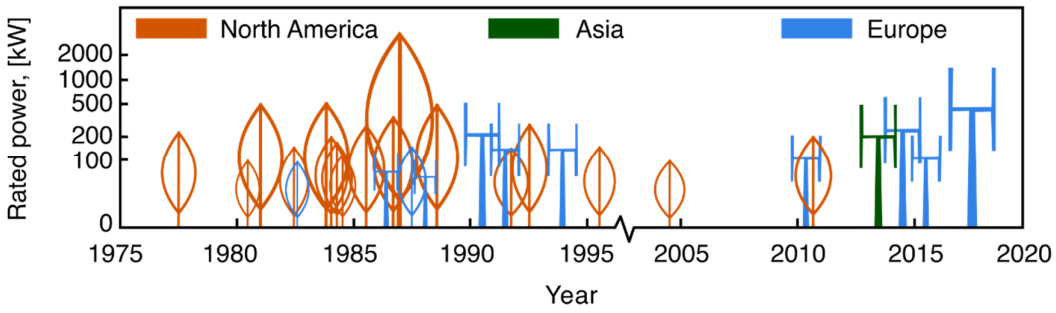

Figure 1.2: Development and installation timeline of VAWTs rated 100 kW and above, highlighting model diversity, regional preferences, and significant growth periods. Redrawn from [15].

Some examples of Darrieus wind turbines are shown in Figure 1.3. The wind turbine in Figure 1.3a is a Darrieus VAWT with straight blades (SB-VAWTs), also known as "H-rotor". Figure 1.3b shows the Éole turbine. This wind turbine was the largest VAWT installed, with a total height of 110 m. The wind turbine in Figure 1.3c is a VAWT with helical blades, also known as Gorlov rotor. The turbine in Figure 1.3d is a Savonius/Darrieus combination that has been patented in Taiwan by Hi-VAWT Technology Corporation.

(a) 12 kW VAWT at Uppsala University[1], Sweden
rotor diameter: 6 m, hub height: 6 m, rated power: 12 kW (at 12m/s).

(b) Éole turbine[2] in Cap-Chat, Québec, Canada
rotor diameter: 64 m, rotor height: 96 m, total height: 110 m, rated power: 3.8 M.

(c) QR6 Turbine, VWT Power Ltd, UK [17]
rotor diameter: 3.1 m, rotor height: 5.1 m, rated power: 7 kW.

(d) Hi-VAWT Technology Corporation, Taiwan [18].
rotor diameter: 2.8 m, rotor height: 3.2 m, rated power: 1.5 KW (at 12 m/s).

Figure 1.3: Some examples of vertical axis wind turbine designs.

[1] S. Apelfröjd, S. Eriksson / Wikimedia Commons / CC BY-SA 4.0
[2] ChristianT/Wikimedia Commons/CC BY-SA 3.0

1.2 VAWT Terminology

The Darrieus turbine employs profiled blades rotating through fluid flow in a plane perpendicular to the axis of rotation. This rotation generates aerodynamic forces, of which the tangential components acting on the blades constitute the primary driving force.

For the 2D analysis of an H-rotor VAWT with N blades and a radius R, we consider the mid-plane xy as shown in Figure 1.4. The blades, with a chord length c, rotate around an axis parallel to the z axis at an angular velocity $\Omega\,\vec{e}_z$, within a uniform freestream velocity field $U_\infty \vec{e}_x$.

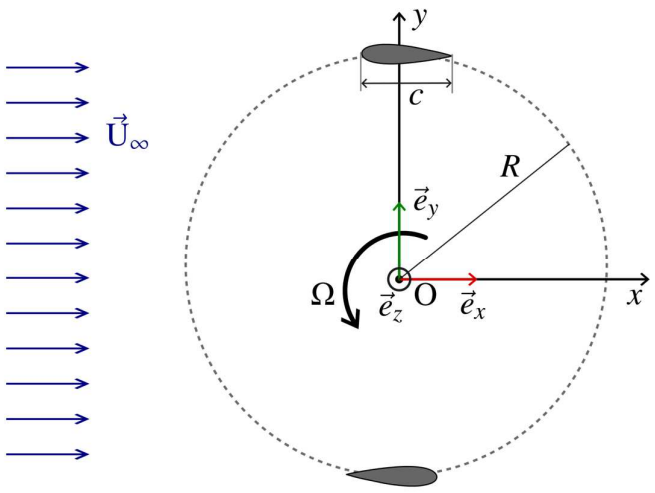

Figure 1.4: Diagram for 2D analysis of an H-rotor VAWT in the mid-plane. The dashed circle represents the trajectory of the blades.

Assuming that the turbine exerts no influence on the incoming freestream velocity, implying no induction effects, the angle of attack (AoA) denoted as α_g, for a VAWT blade can be derived from the geometric relationship between the freestream velocity, $\vec{U}_\infty$, And the velocity experienced by the blade due to rotation given by $-\vec{\Omega} \times \vec{R}$ as depicted in Figure 1.5. This relationship can be expressed as a function of the tip speed ratio, $\lambda = \frac{\Omega R}{U_\infty}$, and the azimuthal angle of the blade, θ, measured relative to the y-axis, as follows:

$$\alpha_g = \arctan\left(\frac{\sin\theta}{\lambda + \cos\theta}\right) + \beta \tag{1.1}$$

In this expression, the assumption is made that the pitch angle, β, is positive when the blade exhibits a positive toe (commonly referred to as toe-in), i.e., the leading edge of the blade is

oriented inward toward the center of rotation of the turbine. The variations in AoA throughout a rotation cycle are plotted in Figure 1.6 for several TSRs.

The expression for the magnitude of the relative velocity experienced by the blade, $\|\vec{U}_{\text{rel}}\|$, is given by:

$$\|\vec{U}_{\text{rel}}\| = U_\infty \sqrt{1 + 2\lambda \cos\theta + \lambda^2} \tag{1.2}$$

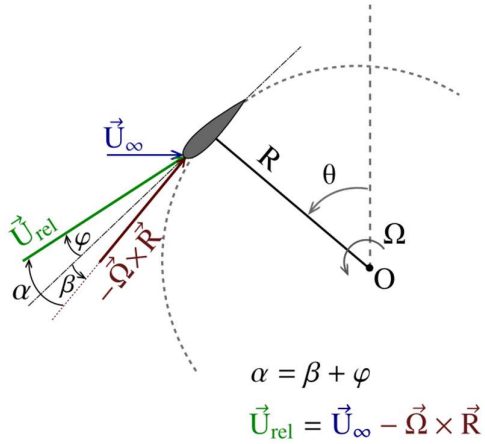

Figure 1.5: Diagram illustrating the velocity triangle for a VAWT blade excluding induction effects.

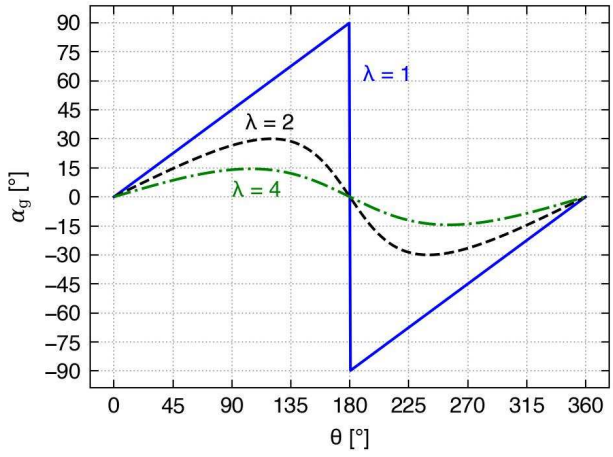

Figure 1.6: The azimuthal variations of VAWT blade's angle of attack during a rotation cycle with the effect of tip speed ratio, λ.

Based on this expression, it could be shown that the relative velocity varies between a maximum value of $U_\infty(\lambda + 1)$ and a minimum value $U_\infty(\lambda - 1)$.

In order to provide a systematic description of the aerodynamics of VAWTs, the following important non-dimensional parameters are presented:

1.2.1 Tip Speed Ratio (TSR)

The tip speed ratio (TSR), λ, is defined as the ratio between the tangential velocity of the blade and the freestream velocity:

$$\lambda = \frac{\Omega R}{U_\infty} \tag{1.3}$$

For low TSRs (typically $\lambda < 4$), the AoA experienced by the blade undergoes substantial variations. These variations significantly exceed the static stall angle, as shown in Figure 1.6. This results in dynamic stall, a phenomenon that will be further explored in section 1.4.2.

Using Eq. (1.1), the maximum AoA can be represented as a function of the TSR as follows:

$$\left|\alpha_g\right|_{max} = \arctan\left(\frac{1}{\sqrt{\lambda^2 - 1}}\right) + |\beta|,$$

at:

$$\begin{cases} \theta = \arccos(-1/\lambda) & \text{if } \beta \geq 0 \\ \theta = 2\pi - \arccos(-1/\lambda) & \text{if } \beta < 0 \end{cases}$$

For higher TSR values, the AoA curve (assuming a constant pitch angle, $\beta = 0$) approaches a sinusoidal curve with low amplitude. This can be expressed as follows:

$$\lim_{\lambda \to \infty} \frac{\alpha_g}{\alpha_{g,max}} = \sin\theta \tag{1.4}$$

1.2.2 Solidity

The solidity for a VAWT is given by:

$$\sigma = \frac{Nc}{2R} \tag{1.5}$$

In addition, the blade solidity, which is also referred to as the curvature parameter, is defined as follows:

$$\sigma_b = \frac{c}{R}$$

1.2.3 Reynolds number

The magnitude of relative velocity given by Eq. (1.2) varies significantly throughout the rotation cycle, resulting in variations in the Reynolds number, Re. However, a constant representative Re is preferred as it simplifies the problem analysis [19].

The average Reynolds number, which is calculated using the average relative velocity, $\bar{U}_{\text{rel}}$, and the blade chord length, c, is given by:

$$\overline{Re}_c = \frac{\bar{U}_{\text{rel}} c}{\nu} \tag{1.6}$$

Where ν is the kinematic viscosity of the fluid. $\bar{U}_{\text{rel}}$ is given by:

$$\bar{U}_{\text{rel}} = \frac{1}{2\pi} \int_0^{2\pi} \left\| \vec{U}_{\text{rel}} \right\| \, \mathrm{d}\theta = \frac{2}{\pi} (\lambda + 1) U_\infty E\left(\frac{4\lambda}{(\lambda + 1)^2} \right) \approx \lambda U_\infty \tag{1.7}$$

In this expression, $E(m)$ function represents the complete elliptic integral of the second kind. By substituting Eq. (1.7) into Eq. (1.6), the following expression can be obtained:

$$\overline{Re}_c \approx \frac{\lambda U_\infty c}{\nu} = \frac{\Omega R c}{\nu} \tag{1.8}$$

1.2.4 Mach number

The Mach number provides information on whether the flow is compressible or incompressible. Similar to the approach used with the Reynolds number above, where a characteristic velocity value is used to derive a dimensionless parameter for a specific operating condition, the Mach number, Ma, is obtained by comparing the characteristic velocity with the speed of sound a_0:

$$\text{Ma} = \frac{\Omega R}{a_0} = \frac{\lambda U_\infty}{a_0} \tag{1.9}$$

1.2.5 Reduced frequency

Throughout a rotation cycle, the AoA and the relative velocity experienced by the blade exhibit periodic variations, as shown previously (See Eq. (1.1) and Eq. (1.2)). This unsteady behavior has a significant impact on the non-linearity of the aerodynamic characteristics of

the blade. To quantify the level of unsteadiness in the flow relative to the blade, the reduced frequency parameter, κ, is defined. For oscillating airfoils, it is given by [20]:

$$\kappa = \frac{\omega c}{2U_{\text{ref}}} \tag{1.10}$$

In this formula, ω denotes the oscillation frequency of the airfoil and U_{ref} is a reference velocity. It is generally accepted that unsteady effects are notable when $\kappa > 0.05$. Specifically for VAWT analysis, ω is employed to denote the blade's angular velocity and U_{ref} refers to the relative velocity [21]:

$$\kappa = \frac{\omega c}{2U_{\text{rel}}} \approx \frac{\omega c}{2\omega R} = \frac{c}{2R} = \frac{\sigma_b}{2} \tag{1.11}$$

However, this formula does not consider the specific nature of AoA variation in Darrieus blades. A formulation that more accurately reflects these conditions was developed by Laneville and Vittecoq [22], which is presented as follows:

$$\kappa = \frac{c\dot{\alpha}_{\max}}{2R\omega\Delta\alpha_{\max}} \tag{1.12}$$

By substituting $\dot{\alpha}_{\max}$ and $\Delta\alpha_{\max}$ expressions, we get:

$$\kappa = \frac{\sigma_b}{2} \times \frac{1}{(\lambda - 1)\arctan\left(\frac{1}{\sqrt{\lambda^2 - 1}}\right)} \tag{1.13}$$

In the present thesis, a simpler version of this formulation that has a relative error of less than 1.8% for all $\lambda > 1.5$ is suggested. It is given as follows:

$$\kappa = \frac{\sigma_b}{2} \times \frac{\lambda - \pi/30}{(\lambda - 1)} \tag{1.14}$$

Both Eq. (1.13) and its equivalent, Eq. (1.14), indicate that the reduced frequency for a blade executing a Darrieus motion depends on blade solidity, σ_b and TSR, λ. The relationship showing inverse proportionality between the TSR and reduced frequency implies that lower values of λ correspond to higher degrees of flow unsteadiness. This is in alignment with the behavior of separated flows, such as dynamic stall, which typically occur under similar conditions.

It should be highlighted that reliance on Eq. (1.11) might result in inaccurate assumptions regarding the level of flow unsteadiness experienced by the blade. Therefore, for accurate VAWT analysis, it is advisable to use Eq. (1.13) or (1.14) instead.

1.3 Different levels of modeling

Various aerodynamic models are available in the literature for the study of VAWT performance, each with different levels of complexity. Conceptually, the turbine can be studied at three different levels: the rotor level (viewing the turbine as a basic energy-capturing device), the blade level (viewing the turbine as a device having blades for harvesting wind energy), and the local level on the blade surfaces (the turbine is seen as a device having blades that interact with the flow to generate a force, through pressure distribution, and extract energy from the wind) [23].

1.3.1 Momentum Models

Momentum models are based on the Blade Element Momentum theory (BEMT), which combines actuator disk theory, commonly referred to as momentum theory, with blade element theory. This approach was first applied to propellers by Glauert [24]. In the context of VAWTs, three main models can be identified: Single Streamtube (SST), Multiple Streamtube (MST), and the Double-Multiple Streamtube model (DMST).

1.3.2 Single Streamtube

The work of Templin [25] in the 1970s led to the development of the single streamtube model for VAWTs. This model simplifies the VAWT into a single actuator disk within a streamtube, as shown in Figure 1.7a, where the change in streamwise fluid momentum is balanced by the streamwise forces exerted on the VAWT blades.

The uniform velocity across the actuator disk, U, is the average of the freestream velocity, U_∞, and the wake velocity, U_w (i.e., $U = 1/2\,(U_\infty + U_\mathrm{w})$). By defining the induction factor, $a = 1 - U/U_\infty$, we can define U, and U_w through a as $U = (1-a)U_\infty$ and $U_w = (1-2a)U_\infty$. Complementing this analysis with the blade element method leads to a non-linear algebraic equation for the unknown induction factor, a, that can be solved iteratively. Consequently, the velocity U is determined, which allows for the computation of the torque and the power of the VAWT by integration of the aerodynamic forces over a full rotation.

Although this approach can predict the overall performance of the VAWT reasonably well for lightly loaded blades, it does not consider the variation of the streamwise forces with the azimuthal position of the blades, a limitation of the uniform velocity assumption across the rotor. These variations become more pronounced at high TSRs, λ, and at high turbine solidities, σ.[26].

1.3.3 Multiple Streamtube

To address the uniform velocity limitations in the previous model, Wilson and Lissaman [27] and later Strickland [28] proposed to split the control volume into a series of adjacent and independent parallel streamtubes, each with its own velocity, U_i, across the actuator disk as shown in Figure 1.7b. The same principle as used by Templin is applied to each of the streamtubes. This approach, referred to as Multiple Streamtube (MST), provides a more accurate representation of the distribution of aerodynamic forces on the blades and is capable of incorporating wind shear effects. The model demonstrated enhancements in predicting performance compared to Templin's model [28].

Despite these improvements, a notable aspect remains to consider: following their trajectory, the blades typically intersect the streamtubes twice. Therefore, using a single actuator disk for both phases oversimplifies the actual aerodynamic interactions. To address this issue, Lapin [29] proposed the implementation of two actuator disks in tandem.

1.3.4 Double-Multiple Streamtube

Building upon the concept of two actuator disks in tandem and the multiple streamtube model, Paraschivoiu [30] introduced the double-multiple streamtube (DMST) model shown in Figure 1.7c. Each streamtube is divided into two distinct halves: upstream and downstream. The analysis is carried out separately for each half. In the first half, the upstream induced velocity, $U_{\mathrm{u},i}$, is determined in a streamtube with inlet velocity U_∞ and an equilibrium velocity, $U_{\mathrm{e},i}$, at its exit. Subsequently, $U_{\mathrm{e},i}$ is used as inlet for the streamtube of the second half to determine the downstream induced velocity, $U_{\mathrm{d},i}$. This model acknowledges the importance of the relative power contributions from both the upstream and downstream portions of the turbine rotation cycle. Nevertheless, the model relies on the assumption that conflicts with the principle of mass conservation: it assumes a constant cross-sectional area for the streamtube traversing the upstream and downstream regions. However, this is inconsistent with the expectation that the velocity should decrease along the streamtube

within the rotor, which would require the streamtube to expand in order to satisfy the continuity equation. In 1985, Paraschivoiu et al. [31] modified the model to incorporate the streamtube expansion effects. These modifications have been implemented in the computer code known as CARDAXX.

Despite these improved models, Momentum-based models have fundamental limitations in the aerodynamic analysis of VAWTs beyond the general shortcomings described previously. These models rely on 2D airfoil data, which are in most cases, unreliable, and the predicted aerodynamic performances have a strong dependence on the chosen database [32]. Furthermore, they become invalid at high TSRs and are not suitable for high-solidity turbines. Ferreira [33] concludes in his study that momentum models are inappropriate for VAWT analysis and should be discontinued.

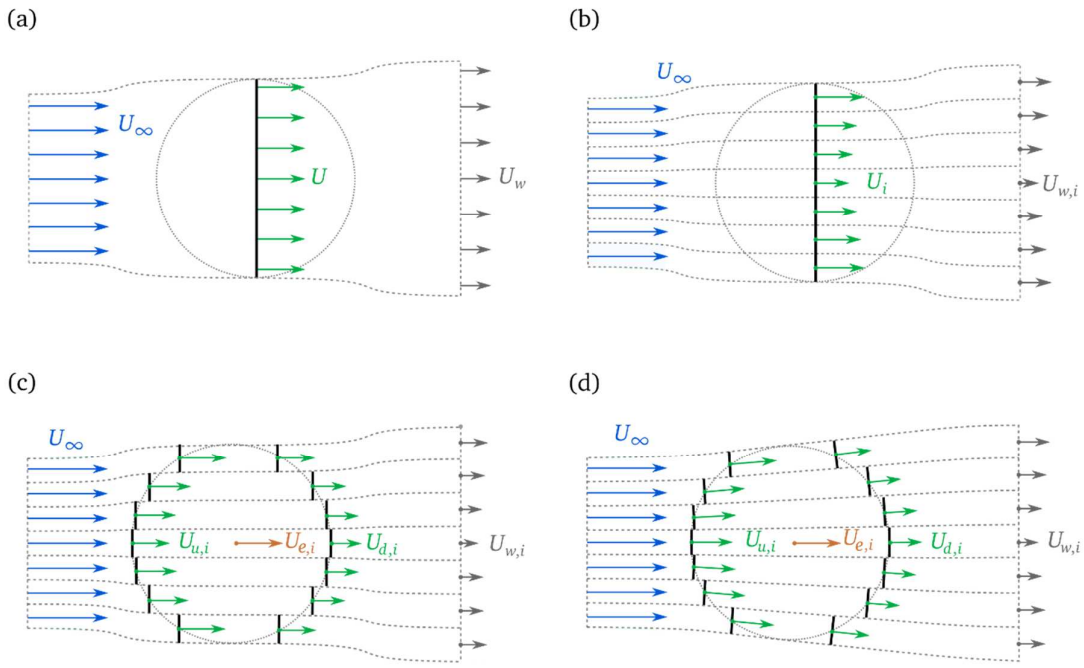

Figure 1.7 : Momentum Models for Vertical Axis Wind Turbine Analysis: (a) Single Stream tube Model, (b) Multiple-Streamtube Model, (c) Double-Multiple Streamtube (DMST), and (d) DMST Model with streamtubes expansion through the rotor.

1.3.5 Cascade model

The cascade model, originally applied to VAWTs by Hirsch and Mandal [34], is based on the cascade theory commonly used in turbo-machinery design. This model conceptualizes the turbine blades as being arranged on a cascade in a plane surface, with equal spacing

determined by the rotor's circumference divided by the number of blades, as shown in Figure 1.8. An extension of this model by Mandal and Burton [35] introduced refinements to account for flow curvature and dynamic stall, enhancing its ability to accurately predict blade forces and power generation, especially aligning well with experimental data.

While relatively more computationally intensive than its momentum model counterparts, the cascade model offers relatively better accuracy for both low and high solidity rotors. It also avoids convergence issues encountered by momentum models in turbines with high solidities at high TSRs [14,36]. However, the cascade model, similar to momentum models, is based on the assumption of steady-state flows, which is inadequate in real-world situations where unsteady flows are prevalent. Moreover, the model's effectiveness depends on empirical parameters and is limited to airfoils with established characteristics [10,14].

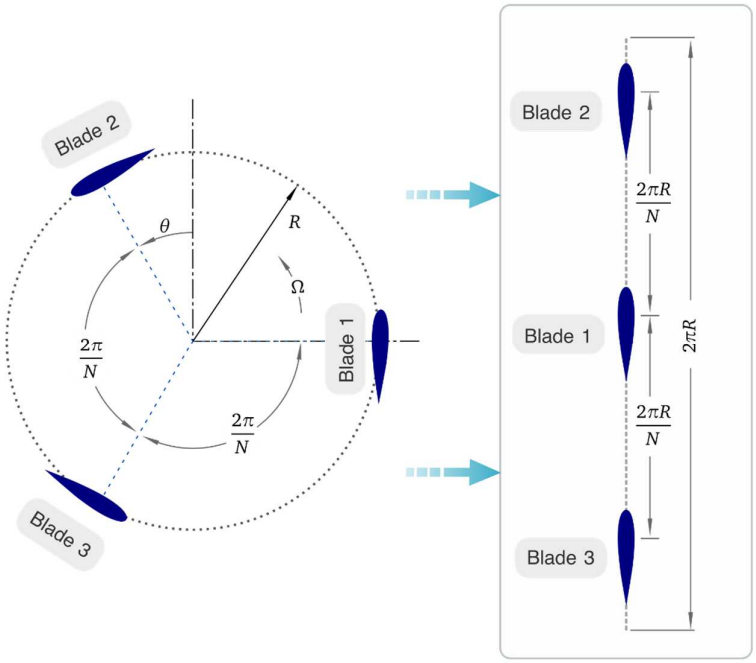

Figure 1.8: Cascade configuration of VAWT blades.

1.3.6 Vortex models

In contrast to previous models that primarily operate at the rotor scale, vortex models are characterized by their relatively higher level of detail, enabling specific modeling of wind turbines at the scale of the blades. In the vicinity of the blades, significant velocity gradients

are present and make the potential flow assumption locally invalid. It is essential to distinguish between the regions where viscosity plays a substantial role, such as boundary layers and blade wakes, and the majority of the fluid domain, which is constituted by irrotational flow [23].

Vortex models combine blade and wake analysis. Blades are modeled using a distribution of singularities, and depending on the level of detail required, different methods can be used, namely lifting line theory (Figure 1.9a), lifting surface theory (Figure 1.9b), or panel methods (Figure 1.9c).

A detailed modeling approach of the turbine wake, mainly consisting of vorticity, involves predicting the location and circulation strength, Γ, of the vortical elements carrying the vorticity, shed from the blades and their convection downstream into the wake (See Figure 1.10 for an example illustrating the vortex lattice in the lifting line model). The wake convection velocity at each location is computed as the vectorial sum of the freestream velocity and the induced velocities by the vortical elements on each other by applying the Biot-Savart law. At each time step, the induced velocities need to be calculated. This is known as *a free-wake method*, which is computationally intensive [37]. According to Snel [37], the computation times required in the *free-wake* method are four orders of magnitude larger than those required for momentum models.

For this reason, numerous *prescribed-wake* methods have been developed, wherein the wake's structure is either fixed or defined by a set of parameters dictating its shape. Although these methods enable faster computations, they are limited in scope compared to the *free-wake* method [38]. Additionally, the so-called hybrid models have also been devised to incorporate the *free-wake* method for the near wake, while the rest of the wake is treated as a *prescribed-wake* [37].

The earliest vortex models for VAWTs were initially formulated in the 1970s by Larsen [39]. These foundational models were further developed by Fanucci and Walter [40] and Wilson [41], among others. While these early models laid the groundwork for the vortex method, their application was somewhat restricted due to various assumptions. These included limitations such as blade AoA being constrained to low values to ignore stall and lightly loaded rotors [36].

The first 3D vortex model (based on lifting-line free-wake formulation) was introduced by Strickland et al. [42]. Additional improvements [43] included incorporating dynamic stall, pitching circulation, and added mass. The model demonstrated a good agreement with experimental results in terms of the instantaneous blade forces and near-wake velocities. Further improvements to this model by Cardona [44] include the integration of curvature effects. It is worth noting that among the vortex models, the free-wake panel method is considered the most accurate. This is because it provides a better representation of the blade geometry [26].

To illustrate these concepts, Figure 1.11 provides a visualization of the lifting line free-wake method, showing the wake structure behind a VAWT.

1.3.7 CFD

A high-fidelity modeling approach for VAWTs employs Computational Fluid Dynamics (CFD). CFD is based on discretizing the fluid domain into a computational mesh and offers the flexibility to include the precise geometry of the blades and the other turbine parts, such as the shaft and struts, enabling selective inclusion/exclusion of specific features as required. The computational mesh allows for resolving the complex flow physics around blades and through the rotor. Modified forms of Navier-Stokes equations are solved on the computational domain using numerical methods, such as finite differences, finite elements, or, more commonly, the finite volume method [45]. Due to the inherent unsteadiness introduced by the rotation of VAWT blades, the simulations must model the transient flow behavior. To account for the motion of the blades within the computational domain, a sliding mesh approach is typically employed. Here, the overall domain encompasses both stationary and rotating sub-domains connected through sliding interfaces. An alternative is to use overset (also known as Chimera) meshes where overlapping stationary and rotating mesh zones exchange information through interpolation.

CFD simulations differ mainly in their choice of turbulence modeling. The Direct Numerical Simulations (DNS) are the most accurate. However, they require exceptionally high spatial and temporal resolutions to resolve all turbulence scales. These requirements make them infeasible for most engineering applications. A more feasible approach that is commonly used is Reynolds Averaged Navier-Stokes (RANS) simulations, in which flow quantities are decomposed into mean and fluctuating parts. However, the averaging process introduces unknown terms that require models to provide closure [46].

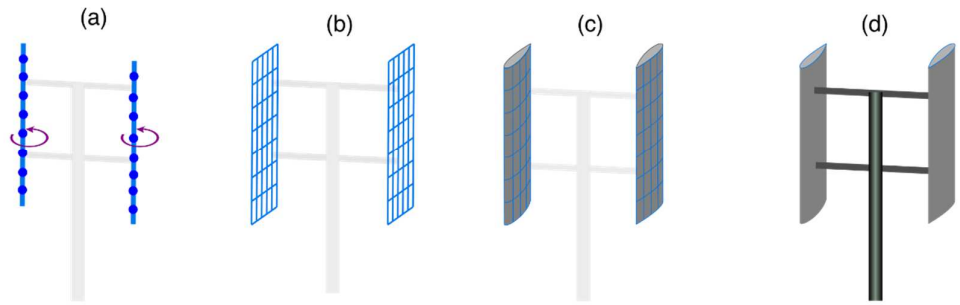

Figure 1.9: Different approaches for the modeling of the turbine blades: (a) lifting line model, (b) lifting surface model, and (c) panel method. (d) a reference VAWT shown for comparative purposes.

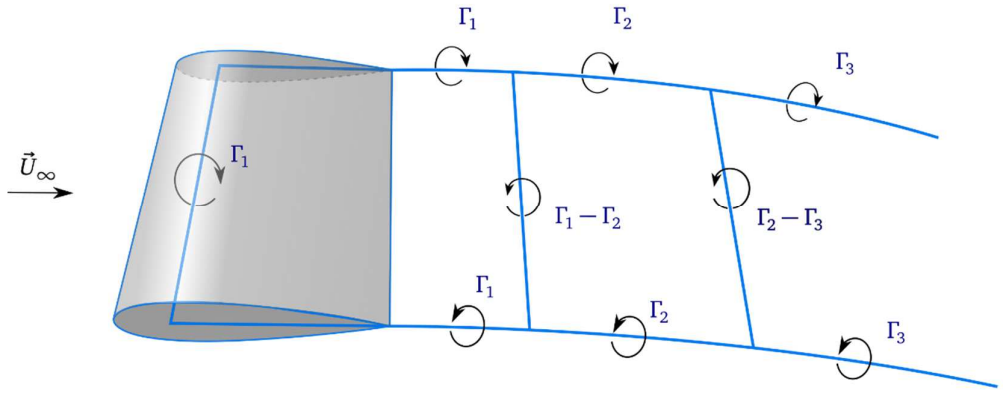

Figure 1.10: Vortex lattice in the wake of lifting line model.

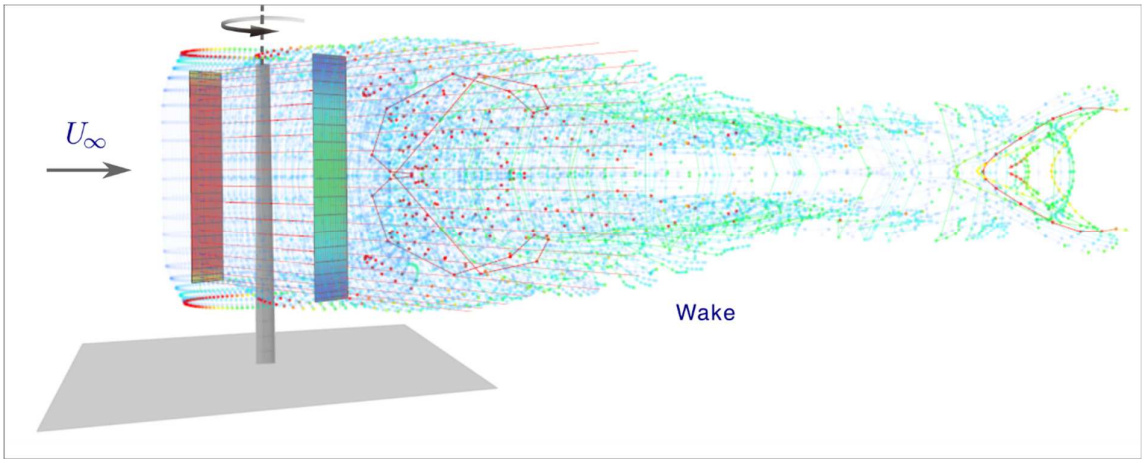

Figure 1.11: A Simulation of the flow around a VAWT with 2 blades using a Free Vortex Wake model at $U_\infty = 10$ m/s, TSR = 4. The blades are modeled using the Lifting Line theory.

Another approach that is computationally expensive compared to RANS is the Large Eddy Simulations (LES). In LES, a filtered version of Navier-Stokes equations is employed to

resolve large eddies, whereas smaller ones are modeled using sub-grid models [47]. In the literature, the use of LES is still limited due to its large computational resource requirements. A promising approach is to use hybrid RANS/LES models [48]. Examples of these models include Detached Eddy Simulations (DES), Delayed DDES (DDES), Improved DDES (IDDES), Scale Adaptive Simulations (SAS), and Partially Averaged Navier-Stokes (PANS) [47].

The application of CFD enables the exploration of complex flow features inherent to the operation of VAWTs. This includes phenomena such as dynamic stall, which typically occurs at low tip speed ratios and blade vortex interactions. Table 1.1 provides an overview of turbulence models applied in VAWT research. It highlights a range of studies with a diversity of approaches within the field. This overview is not exhaustive and serves as a representative sample of the existing literature. For comprehensive reviews of the CFD models employed for the study of VAWTs, one might refer to [45,49–52].

It should be noted that hybrid models that combine low-order models and CFD exist. These models do not employ the exact geometry of the blades. Among these methods, the Actuator Line Method (ALM) [53] is an example worth mentioning.

Table 1.1: Overview of Turbulence models applied in VAWT research.

Reference	**Year**	**Turbulence model**	**CFD Modeling**	**Reynolds Number**	**Purpose/Topic**
Amet et al. [54]	2009	k-ω	2D	3×10^3	Investigation of Blade–vortex interactions
Howell et al. [55]	2010	RNG k-ε	2D and 3D	2.1 to 3.7 $\times 10^4$	VAWT performance
Untaroiu et al. [56]	2011	Standard k-ε	2D and 3D	3.4×10^4	Self-starting behavior of VAWTs
Castelli et al. [57]	2011	Realizable k-ε	2D	5.2×10^4	Turbine performance
Mohamed [58]	2012	Realizable k-ε	2D	N/A	Impact of different airfoils on VAWT performance
Mohamed [59]	2014	Realizable k-ε	2D	N/A	Aero-acoustics noise of VAWT
Daróczy et al. [60]	2015	Several eddy viscosity models	2D	2.0×10^4 to 2.7×10^5	Optimizing H-Darrieus Rotor Airfoil Shapes
Lee & Lim [61]	2015	RNG k-ε	3D	8.1×10^4 to 1.62×10^5	Design Optimization of VAWT
Joo et al. [62]	2015	Realizable k-ε	3D	1.61×10^5	Effect of solidities and rotating speeds on VAWT performance

Edwards et al. [63]	2012	SST k-ω	2D	1.8×10^4	Performance analysis of VAWT
Castelli et al. [64]	2013	SST k-ω	3D	5.2×10^4	Aerodynamic and inertial contributions to VAWT blade deformation
Danao et al. [65]	2014	SST k-ω and Transition SST k-ω	2D	N/A	Influence of freestream fluctuations on VAWT performance
Almohammadi et al. [66]	2015	SST k-ω	2D	2.83×10^5	Dynamic stall
Bhargav et al. [67]	2016	SST k-ω	3D	$\approx 3.04 \times 10^5$	Influence of freestream fluctuations on VAWT performance
Meana-Fernandez et al. [68]	2018	SST k-ω	2D	6.8×10^4 to 1.01×10^5	Impact of design parameters on VAWT performance
McLaren et al. [69]	2012	Transition SST k-ω	2D	3.6×10^5	Blade-vortex interactions
Rossetti & Pavesi [70]	2013	Transition SST k-ω	2D and 3D	3.4×10^4	Start-up behavior of VAWT
Lam & Peng [71]	2016	Transition SST k-ω	2D and 3D	3.8×10^4	Characteristics of VAWT wake
Alireza et al. [72]	2017	Transition SST k-ω	2D	4.7 to 16.9 $\times 10^4$	Start-up behavior and performance of VAWT
Balduzzi et al. [73]	2017	Transition SST k-ω	3D	5.2×10^4	3D effects on VAWT performance
Rezaeiha et al. [74]	2017	Transition SST k-ω	2D and 2.5D	3.8×10^4	Guidelines for CFD simulations of VAWTs
Wekesa et al. [75]	2017	Transition SST k-ω	2D	3.0×10^4	Effect of unsteady winds on VAWT performance
Rezaeiha et al. [76,77]	2018	Transition SST	2D and 2.5D	3.8×10^4	Influence of operational parameters on VAWT performance
Zhu et al. [78]	2023	SST k-ω and transition SST	2D	10^5 to 7×10^5	Impact of the Reynolds number and reduced frequency on VAWT performance
Li et al. [79]	2013	SST k-ω and LES	2D and 2.5D	3×10^5	Accuracy of 2.5D LES in VAWT Aerodynamic Analysis
Ghasemian & Nejat [80]	2015	LES	3D	2.1×10^4 to 1.2×10^5	Aero-acoustic prediction of VAWT noise
Peng & Lam [81]	2016	LES	3D	1.3×10^4 to 3.6×10^4	Turbulence effects on VAWT performance and wake characteristics
Lei et al. [82]	2017	IDDES	3D	1.62×10^5 to 2.89×10^5	Turbine performance and comparison of IDDES and SST k-ω models
Patil et al. [83]	2018	LES	3D	8×10^4	Flow field around a VAWT using LES

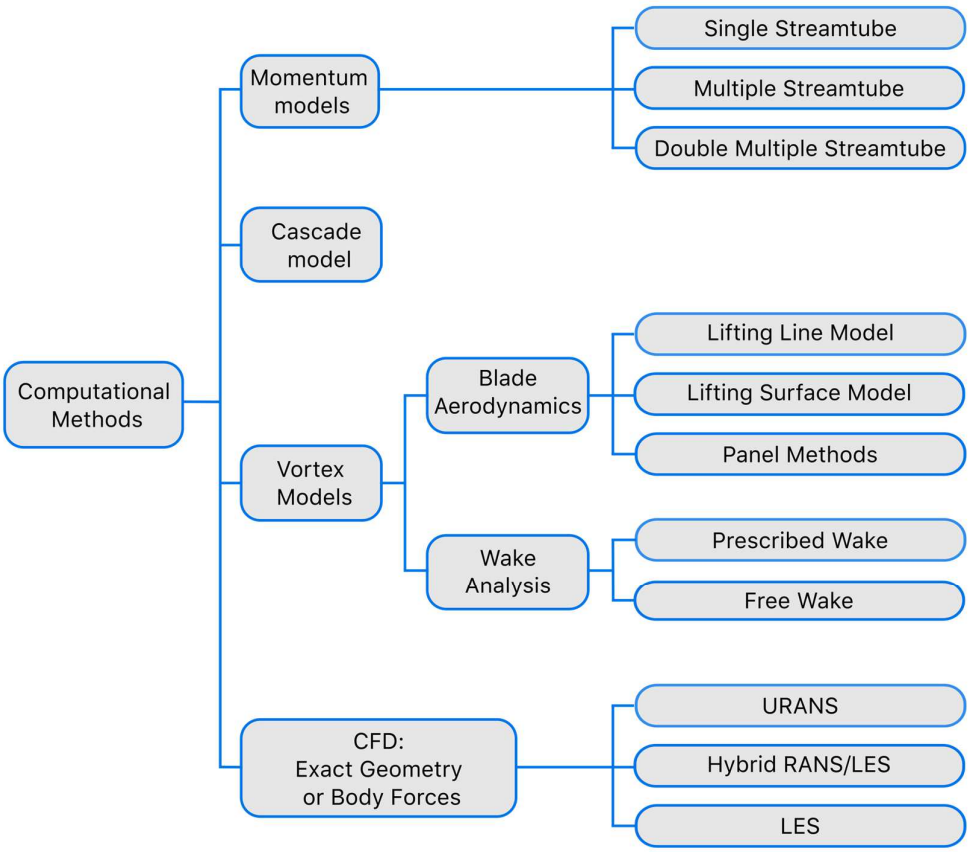

Figure 1.12: Computational methods for the analysis of VAWTs performance.

The computational methods used in the aerodynamic analysis of VAWTs, as discussed above, are summarized in Figure 1.12.

1.4 Unsteady aerodynamics

1.4.1 Flow Curvature

Due to the rotational motion inherent in the operation of VAWTs, their blades are subject to curvilinear flow. This aspect of their motion results in aerodynamic behaviors that are considerably different from those experienced in rectilinear flow. The circular motion trajectory of the blades creates a flow asymmetry between the inner and outer surfaces of the blades, as well as between the front and rear of the profile [23]. Migliore et al. [84] showed through conformal mapping that a symmetrical airfoil in curvilinear flow can be transformed into an equivalent virtual cambered airfoil with a virtual AoA (Figure 1.13). It was also shown that curvature effects become more pronounced as the solidity of the blade, c/R,

increases. In models that rely on conventional airfoil data, such as momentum models, and cascade model, corrections should be incorporated to take into account the curvature effect in VAWT motion. These corrections lead to enhanced prediction of these models [10].

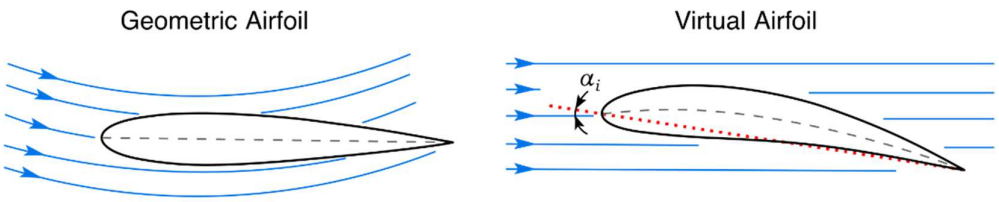

Figure 1.13: Curvature effects. Redrawn from [84].

1.4.2 Dynamic stall

Dynamic stall occurs on airfoils and other lifting surfaces undergoing unsteady motions like pitching or plunging when the AoA exceeds the static stall value [20]. Unlike static stall, flow separation is delayed to angles considerably beyond the static stall angle, producing lift coefficients well above static counterparts. Dynamic stall critically impacts diverse engineering systems like helicopter rotors and wind turbines [85]. VAWT blades operating at low TSRs exhibit dynamic stall due to the large variations of the AoA during the rotation cycle, as shown in Figure 1.6. For this reason, dynamic stall is inherent to their operational state. Accurately modeling dynamic stall is essential for predicting the power generation as well as estimating the cyclic loading and consequent fatigue damage that could occur.

The AoA variation throughout a rotation cycle resembles that of a sinusoidal pitching airfoil, the latter configuration is extensively studied and for which a large number of experimental investigations addressing dynamic stall phenomenon exist [86]. For an oscillating airfoil, the dynamic stall process can be characterized by a sequence of events outlined as follows [87]:

- When the AoA exceeds the static stall angle, a thin reversed flow layer forms at the bottom of the boundary layer. In trailing-edge stalling airfoils, this layer originates at the rear of the airfoil and progresses upstream toward the leading edge. Conversely, in leading-edge stalling airfoils, the separation region forms immediately downstream of the suction peak.
- Within the separated region near the leading edge, a vortex starts to form and enlarges while being convected downstream at a slower speed than the freestream. As a result,

the lift coefficient continues to rise until the vortex moves past the mid-chord point, while there is a sharp drop in the moment coefficient and a considerable increase in the drag coefficient.

- As the vortex reaches the trailing edge, the flow becomes fully separated.
- As the AoA decreases, the flow begins to reattach over the surface of the airfoil starting from the leading edge toward the trailing edge.

These events are illustrated below in Figure 1.14.

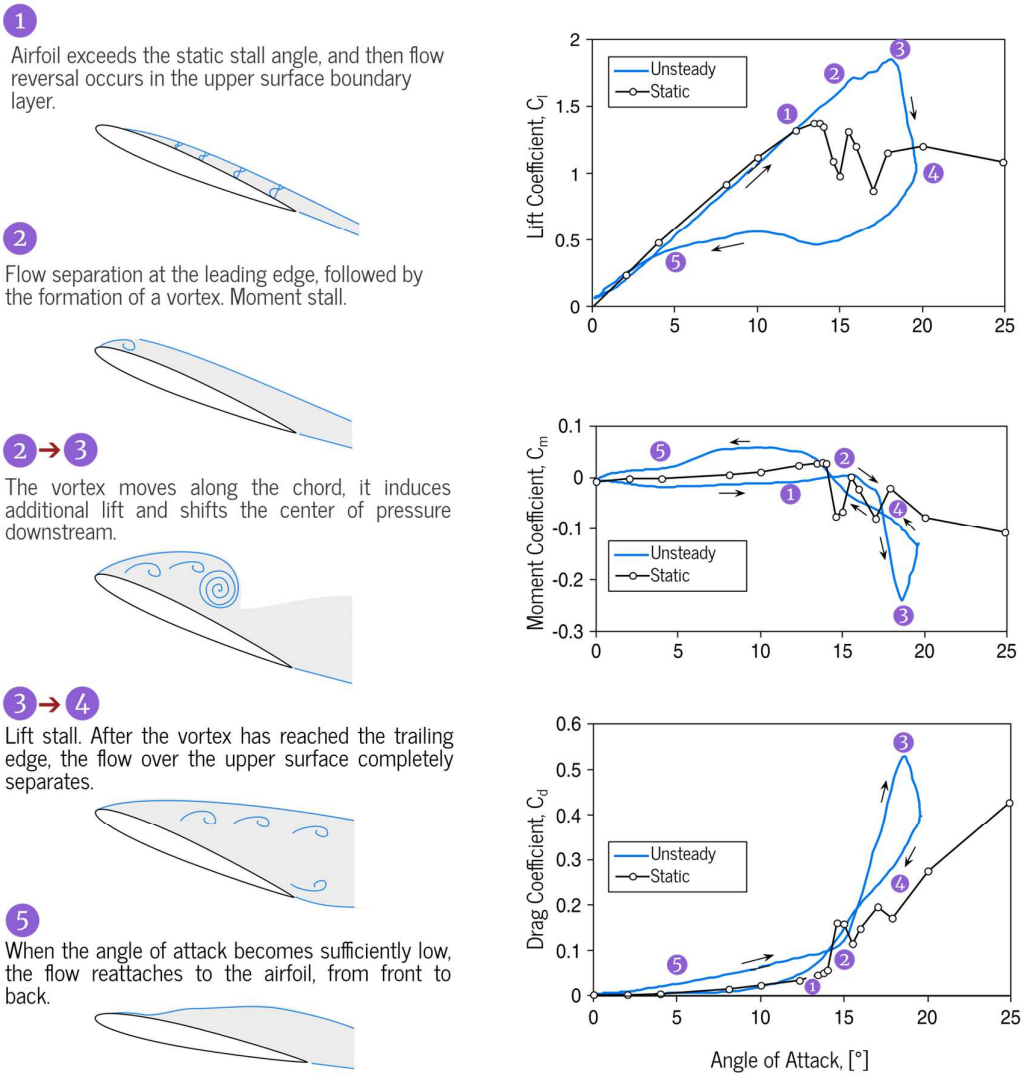

Figure 1.14: Events characteristic of dynamic stall on an airfoil. Redrawn from [38].

In the studies conducted by Carr et al. [88] on airfoils undergoing sinusoidal pitching, three primary mechanisms initiating dynamic stall were identified: (a) the gradual upstream spread of trailing-edge separation reaching the leading-edge, (b) sudden turbulent separation near the leading-edge, and (c) the "bursting" of a leading-edge laminar separation bubble (LSB). Additionally, McCroskey et al. [89] observed another mechanism involving the breakdown of flow near a mid-chord location of the initial boundary layer separation, which extends both downstream and upstream along the suction side of the airfoil. These experiments, focusing on 2D airfoil sections, encompassed a broad spectrum of unsteady flow conditions and variables, such as variations in airfoil leading-edge shape, Reynolds number, and the amplitude and frequency of oscillation. Notably, the dynamic stall onset mechanism showed sensitivity to these tested parameters, yet no alteration in the qualitative nature of dynamic stall was observed when the airfoil entered a deep-stall regime.

Extensive experimental research following these findings has significantly enhanced the understanding of factors influencing the dynamic stall process, particularly concerning stall onset. It has become evident that this phenomenon is influenced by a complex interplay of various parameters. These include reduced frequency [90,91], Mach number [92], mean angle of attack, oscillation amplitude [93,94], type of motion [95], freestream velocity profile [96], and Reynolds number [97].

In the late 1970s, experimental research initiated the exploration of the fundamental physical aspects of dynamic stall, leading numerous researchers to develop semi-empirical models for predicting stall behavior. The complexity of these models varies, particularly in their treatment of the elementary phenomena occurring at different stages of dynamic stall [23]. Notable among these models are the Onera model [98], the Boeing-Vertol model [99], and the Leishman-Beddoes model [100]. These models, initially designed for aeronautical applications, have been adapted for wind turbine research and have found widespread use. However, their reliance on experimental data to calibrate model coefficients for specific airfoil sections limits their applicability primarily to conventional airfoil designs.

Recent advancements in computational power, computational methods, and turbulence modeling have enabled the computation of complex unsteady flows using the full unsteady Navier-Stokes equations. This approach helps to address the limitations inherent in semi-empirical methods. Nonetheless, the selection of the turbulence model is a critical factor that significantly impacts the accuracy of these computational methods [101,102].

1.5 VAWT design parameters

Beyond the unsteady aerodynamic phenomena discussed earlier, there are several critical design parameters that significantly influence the performance of VAWTs. Key among these are solidity, blade airfoils, Reynolds number, strut design, number of blades, blade orientations, blade aspect ratio, blade pitch angles, and blade-strut connections, as depicted in Figure 1.15. For comprehensive analysis, one might refer to the review by Hand et al. [103].

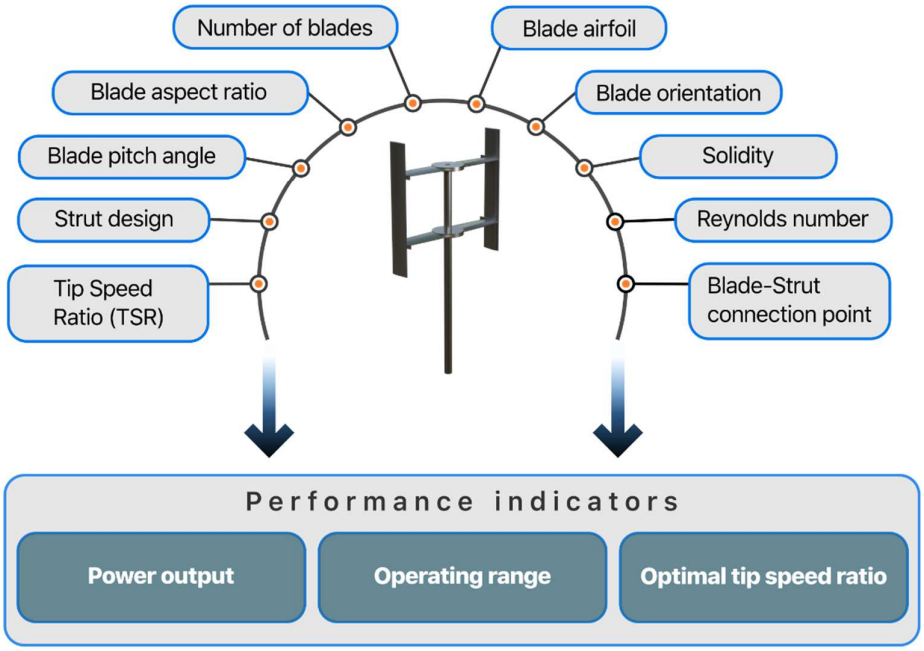

Figure 1.15: Various design parameters influencing the performance of VAWTs.

1.6 Summary

In this chapter, we presented various aerodynamic analysis models for VAWTs, including the momentum models, cascade model, vortex models, and CFD models. Additionally, we discussed specific unsteady aerodynamic phenomena related to VAWTs, such as curvature effects and dynamic stall. Examination of the literature indicates that the use of simplified models like the momentum models and cascade models has become notably limited. While vortex models are still employed, their usage is reduced compared to the comprehensive application of CFD. Thus, CFD emerges as the predominant tool for VAWT analysis.

In CFD studies of VAWTs, most investigations are limited to 2D URANS simulations due to the significant computational resources required for 3D simulations. LES studies, although

used to a certain extent, most of them appear to use coarse meshes and large time steps, leading to results whose accuracy is subject to question. Despite these extensive studies, the complex aerodynamics of VAWTs are still far from being fully understood, necessitating further in-depth research to gain insights into various phenomena.

The following chapter will present the required methodologies for CFD analysis of VAWTs, detailing the governing equations and various turbulence models.

.

Chapter 2

Governing Equations and Turbulence Modeling

2.1 Introduction

Recognizing the limitations of simplified methods discussed in the previous chapter in capturing the full complexity of flow around VAWTs and the associated unsteady phenomena, CFD stands as a critical tool for detailed and accurate analysis. This chapter focuses on presenting the governing equations for fluid flow within CFD for the analysis of VAWTs. These equations, in an absolute frame of reference, are adapted to suit the specific computational domain, which comprises both rotating and stationary regions. The same governing equations are applicable to the study of oscillating airfoils with appropriate modifications to incorporate the oscillation motion instead of pure rotation.

These equations are solved using a URANS approach. Accordingly, the Reynolds averaging procedure is presented, followed by an overview of the different eddy viscosity models employed in this work for turbulence modeling. While these equations and turbulence models are presented independently of any specific solver and are applicable to most CFD solvers, it is important to note that the solver used in this thesis is OpenFOAM. Therefore, the presentation of the turbulence models is implicitly focused on their implementation in OpenFOAM unless stated otherwise.

2.2 Governing equations

The governing equations for the 2D compressible, unsteady flow of a viscous fluid consist of the Navier-Stokes equations (mass and momentum conservation) alongside the energy equation (energy conservation). These equations together provide a complete mathematical framework for the analysis of fluid dynamics. In simulations that involve moving meshes with rigid body motion, both the overset (Chimera) and sliding mesh techniques are possible options, with the latter being more commonly used. The sliding mesh approach divides the computational mesh into rotating and stationary regions connected through an interface.

To account for the relative motion between the rotating and stationary regions, the governing equations are expressed in the Arbitrary Lagrangian-Eulerian form [104,105]:

$$\frac{\partial \vec{W}}{\partial t} + \frac{\partial\left(\vec{F}_x - \vec{F}_x^V\right)}{\partial x} + \frac{\partial\left(\vec{F}_y - \vec{F}_y^V\right)}{\partial y} = \vec{0} \tag{2.1}$$

where $\vec{W}$ is the vector of conservative variables. $\vec{F} = (\vec{F}_x,\ \vec{F}_y)$ and $\vec{F}^V = (\vec{F}_x^V,\ \vec{F}_y^V)$ are the inviscid flux and viscous flux vectors, respectively. These vectors are given by:

$$\vec{W} = \begin{bmatrix} \rho \\ \rho u \\ \rho v \\ \rho E \end{bmatrix} \qquad \vec{F}_x = \begin{bmatrix} \rho u - \rho u_{\mathrm{m}} \\ \rho u^2 + p - \rho u v_{\mathrm{m}} \\ \rho u v - \rho v u_{\mathrm{m}} \\ \rho u H - \rho E u_{\mathrm{m}} \end{bmatrix} \qquad \vec{F}_y = \begin{bmatrix} \rho v - \rho v_{\mathrm{m}} \\ \rho u v - \rho u v_{\mathrm{m}} \\ \rho v^2 + p - \rho v v_{\mathrm{m}} \\ \rho v H - \rho E v_{\mathrm{m}} \end{bmatrix} \tag{2.2}$$

where:

- u, and v are the x and y velocity components, respectively.
- $E = p/[\rho(\gamma - 1)] + \frac{1}{2}\left(u^2 + v^2\right)$, is the specific total energy, assuming a calorifically perfect gas. The pressure p is given by the equation of state $p = \rho RT$, with ρ representing the density, R the specific gas constant, and T is the temperature. γ is the specific heat ratio.
- $H = E + p/\rho$ is the specific total enthalpy.
- $\vec{u}_{\mathrm{m}} = (u_{\mathrm{m}}, v_{\mathrm{m}}) = \vec{\Omega} \times \vec{r}$ is the mesh velocity. $\vec{\Omega}$ is the angular velocity, and $\vec{r}$ is the position vector relative to the rotating center. In the stationary region, $\vec{u}_m = \vec{0}$.

The viscous fluxes are given by:

$$\vec{F}_x^V = \begin{bmatrix} 0 \\ \tau_{xx} \\ \tau_{xy} \\ u\tau_{xx} + v\tau_{xy} - q_x \end{bmatrix} \qquad \vec{F}_y^V = \begin{bmatrix} 0 \\ \tau_{xy} \\ \tau_{yy} \\ u\tau_{xy} + v\tau_{yy} - q_y \end{bmatrix} \tag{2.3}$$

- $\vec{q} = \left(q_x, q_y\right)$ is the thermal conduction flux.
- The viscous stresses are defined as:

$$\tau_{xx} = 2\mu \frac{\partial u}{\partial x} - \frac{2}{3}\mu \left(\frac{\partial u}{\partial x} + \frac{\partial v}{\partial y}\right)$$
$$\tau_{yy} = 2\mu \frac{\partial v}{\partial y} - \frac{2}{3}\mu \left(\frac{\partial u}{\partial x} + \frac{\partial v}{\partial y}\right)$$
$$\tau_{xy} = \mu \left(\frac{\partial u}{\partial y} + \frac{\partial v}{\partial x}\right)$$

where μ is the dynamic viscosity of the fluid.

When considering incompressible isothermal flow, the expressions for the governing equations are simplified as follows:

$$\vec{W} = \begin{bmatrix} 0 \\ u \\ v \end{bmatrix} \qquad \vec{F}_x = \begin{bmatrix} \rho u - \rho u_{\mathrm{m}} \\ \rho u^2 + p - \rho u u_{\mathrm{m}} \\ \rho u v - \rho v u_{\mathrm{m}} \end{bmatrix} \qquad \vec{F}_y = \begin{bmatrix} \rho v - \rho v_{\mathrm{m}} \\ \rho u v - \rho u v_{\mathrm{m}} \\ \rho v^2 + p - \rho v v_{\mathrm{m}} \end{bmatrix} \tag{2.4}$$

$$\vec{F}_x^V = \begin{bmatrix} 0 \\ \mu \dfrac{\partial u}{\partial x} \\ \mu \dfrac{\partial v}{\partial x} \end{bmatrix} \qquad \vec{F}_y^V = \begin{bmatrix} 0 \\ \mu \dfrac{\partial u}{\partial y} \\ \mu \dfrac{\partial v}{\partial y} \end{bmatrix} \tag{2.5}$$

2.3 Finite volume formulation

The finite volume method discretizes the governing equations for $\phi_i = W_i/\rho$ over an arbitrary moving volume, V, bounded by closed control surface A. These equations, in their integral form formulated in the ALE framework, are presented as follows [106,107]:

$$\frac{\partial}{\partial t}\int_V \rho\phi_i \,\mathrm{d}V + \oint_A \rho\vec{n} \bullet (\vec{u} - \vec{u}_{\mathrm{m}})\phi_i \,\mathrm{d}A = \oint_A \Gamma_{\phi_i}\vec{n} \bullet \nabla\phi \,\mathrm{d}A + \int_V S_{\phi_i} \,\mathrm{d}V \tag{2.6}$$

where $\vec{n}$ represents the unit normal vector that points outward on the boundary surface. Γ_{ϕ_i} is the diffusion coefficient, and S_{ϕ_i} is the source term of ϕ_i.

The variation in the control volume is connected to the mesh velocity via the space conservation law (SCL):

$$\frac{\partial}{\partial t}\int_V \mathrm{d}V = \oint_A \vec{u}_{\mathrm{m}} \cdot \vec{n} \,\mathrm{d}A$$

In the special case of sliding meshes where the mesh cells undergo rigid motion without deformation, the SCL simplifies to:

$$\oint_A \vec{u}_{\mathrm{m}} \cdot \vec{n} \,\mathrm{d}A = 0$$

2.4 Reynolds Averaging

The solution of the 3D version of the governing equations through direct numerical simulations is generally infeasible for most engineering applications, primarily due to the extensive computational requirements [108].

LES, which solve filtered versions of the governing equations, offer greater accuracy than URANS models but are not yet extensively employed in engineering applications due to their substantial computational costs. On the other hand, URANS models are more commonly employed because of their relatively lower computational demands. Benefiting from advances in computing power, URANS models have been effectively applied to a variety of complex problems, demonstrating their importance in the field of CFD analysis [46].

In the URANS approach, Reynolds-averaging is applied to decompose the flow variables ϕ_i into a mean value, $\bar{\phi}_i$, and a fluctuating one, ϕ_i' :

$$\phi_i = \bar{\phi}_i + \phi_i' \tag{2.7}$$

The mean value is obtained by time-averaging, assuming that time variations in ϕ_i are very slow compared to the turbulent fluctuations' time scale and short in comparison to the unsteadiness in the mean flow [109]:

$$\bar{\phi}_i(x, y, t) = \frac{1}{T} \int_{t}^{t+T} \phi(x, y, t) \mathrm{d}t \tag{2.8}$$

Where T in this expression denotes the averaging interval.

Note that in compressible flows, the Favre averaging (density-weighted time-averaging) is typically used instead of the classical Reynolds averaging. According to Cress et al. [110], the difference between the two approaches is less than 1.5% for Mach numbers below 3. In the present work, the Mach numbers are much lower; therefore, the two averaging approaches are interchangeable.

These decomposed flow variables in Eq. (2.7) are then substituted into the original governing equations. After this substitution, the equations are time-averaged. This procedure effectively captures the mean flow behavior. However, it also introduces more unknowns than the

available equations, leading to a situation known as the closure problem. This problem arises because the time-averaging process adds additional terms related to the fluctuations, thereby necessitating further modeling to resolve the system. The additional terms in the momentum equations, known as the Reynolds stress tensor, represent the interaction between the turbulence and the mean flow [111]. For compressible flows, several terms are introduced in the energy equation, namely turbulent heat fluxes and terms related to molecular diffusion and turbulent transport.

The concept of *eddy viscosity* was introduced by Boussinesq in 1877 to establish a relationship between the Reynolds stresses and the mean velocity gradients. Likewise, in compressible flows, the turbulent heat fluxes are related to the mean temperature gradients [109]:

- Reynolds stress tensor in index notation:

$$\tau_{ij}^{R} \equiv -\overline{\rho u_i' u_i'} = \mu_t \left(\frac{\partial \bar{u}_i}{\partial x_j} + \frac{\partial \bar{u}_j}{\partial x_i} \right) - \frac{2}{3} \left(\bar{\rho} k + \mu_t \frac{\partial \bar{u}_k}{\partial x_k} \right) \delta_{ij} \tag{2.9}$$

  where μ_t is the eddy viscosity, $k = \frac{1}{2}\overline{u_i' u_i'}$ is the turbulent kinetic energy and δ_{ij} is the Kronecker delta.

- Turbulent heat flux vector:

$$q_j^{\text{turb}} = c_p \overline{\rho u_j' T'} = -\frac{\mu_t c_p}{Pr_t} \frac{\partial \bar{T}}{\partial x_j} \tag{2.10}$$

where Pr_t is the turbulent Prandtl number, c_p is the heat capacity at constant pressure.

- The terms associated with the molecular diffusion and turbulent transport are often grouped together and commonly approximated as:

$$\overline{\tau_{ij} u_i'} - \frac{1}{2} \overline{\rho u_j' u_i' u_i'} \approx \left(\mu + \frac{\mu_t}{\sigma_k} \right) \frac{\partial k}{\partial x_j}$$

where σ_k is a coefficient associated with the modeled equation of k. These terms are usually ignored for flows with low Mach numbers [109].

In what follows, the overbar notation for mean quantities is omitted in the equations of turbulence models, to simplify the notation.

2.5 Turbulence Models

The primary goal of turbulence modeling is to develop models to close the mean flow equations obtained by the averaging process. Closure models consist of empirical formulas and equations that are designed to balance the number of equations with the number of unknowns. These models often employ transport equations for fields of turbulence variables. These variables may be specific to the model and might not have a clear physical interpretation. Among these closure models, the eddy viscosity models are particularly popular. Examples include the k-ε, k-ω, and Spalart-Allmaras models [46].

For wall-bounded turbulent flows, the treatment of near wall regions holds equal importance to the formulation of the turbulence model itself [112]. Near walls, the flow variables have large gradients, and thus resolving viscous sublayer within the boundary layer requires fine meshes with dimensionless wall distances, y^+, of around 1 or less, which is computationally expensive. The models that are based on the viscous sublayer formulation are historically termed *low-Reynolds number* models. Nonetheless, as noted by Menter [112], this terminology is misleading because the Reynolds number refers to the turbulent Reynolds number $R_T = \mu_t/\mu$, not to the global Reynolds number. Therefore, the terminology VSM (Viscous Sublayer Model) is preferred.

Wall functions are commonly used in CFD to reduce computational costs by avoiding the need to resolve the near-wall region. However, the wall function approaches rely on the assumption of universal wall behavior. Though this assumption is reasonably accurate for attached boundary layers with mild pressure gradients, it breaks down for complex flows [108].

Because the fidelity of the numerical simulations is significantly impacted by the near-wall treatment, accurate modeling of these regions is required. For complex unsteady separated flows considered in this thesis, the wall function approach is clearly not suitable. For this reason, we consider a consistent treatment based on viscous sublayer modeling, and as a result, only compatible turbulence models (i.e., models that can be integrated through the viscous sublayer) are used.

For convenience, the equations presented below are not expressed in the ALE form. To recover this formulation, the mesh velocity fluxes should be subtracted from the convection terms.

2.5.1 Spalart-Allmaras

The Spalart-Allmaras model [113] is a one-equation model that involves solving a transport equation for a modified kinematic eddy viscosity, $\tilde{\nu}$. The model is originally a VSM model, that requires resolving the viscosity-affected region within the boundary layer. The transport equation is given by:

$$\frac{\partial \tilde{\nu}}{\partial t} + u_j \frac{\partial \tilde{\nu}}{\partial x_j} = c_{b1}(1 - f_{t2})\tilde{S}\tilde{\nu} - \left[c_{w1} f_w - \frac{c_{b1}}{\kappa^2} f_{t2}\right]\left(\frac{\tilde{\nu}}{d}\right)^2 + \frac{1}{\sigma}\left[\frac{\partial}{\partial x_j}\left((\nu + \tilde{\nu})\frac{\partial \tilde{\nu}}{\partial x_j}\right) + c_{b2}\frac{\partial \tilde{\nu}}{\partial x_i}\frac{\partial \tilde{\nu}}{\partial x_i}\right] \quad (2.11)$$

The eddy viscosity is computed from:

$$\mu_t = \rho \tilde{\nu} f_{v1} \quad (2.12)$$

where

$$f_{v1} = \frac{\chi^3}{\chi^3 + c_{v1}^3}, \qquad \chi = \frac{\tilde{\nu}}{\nu}$$

and $\nu = \mu/\rho$ is the kinematic viscosity of the fluid. The additional terms are given by

$$\tilde{S} = \sqrt{2\widehat{\Omega}_{ij}\widehat{\Omega}_{ij}} + \frac{\tilde{\nu}}{\kappa^2 d^2} f_{v2}, \qquad \widehat{\Omega}_{ij} = \frac{1}{2}\left(\frac{\partial u_i}{\partial x_j} - \frac{\partial u_j}{\partial x_i}\right), \qquad f_{v2} = 1 - \frac{\chi}{1 + \chi f_{v1}}$$

$$f_w = g\left[\frac{1 + c_{w3}^6}{g^6 + c_{w3}^6}\right]^{\frac{1}{6}}, \qquad g = r + c_{w2}\left(r^6 - r\right), \qquad r = \min\left(\frac{\tilde{\nu}}{\tilde{S}\kappa^2 d^2}, 10\right)$$

$$f_{t2} = c_{t3} \exp\left(-c_{t4}\chi^2\right)$$

d is the distance from the nearest wall to the field point.

The boundary conditions of $\tilde{\nu}$ are [114]:

$$\tilde{\nu}_{\text{wall}} = 0, \qquad \tilde{\nu}_\infty = 3\nu_\infty \text{ to } 5\nu_\infty.$$

The model constants are:

$c_{b1} = 0.1355$ $\quad \sigma = 2/3$ $\quad c_{b2} = 0.622$ $\quad \kappa = 0.41$ $\quad c_{w2} = 0.3$

$c_{w3} = 2$ $\quad c_{v1} = 7.1$ $\quad c_{t3} = 1.2$ $\quad c_{t4} = 0.5$ $\quad c_{w1} = \frac{c_{b1}}{\kappa^2} + \frac{1 + c_{b2}}{\sigma}$

Note that the OpenFOAM implementation ignores the f_{t2} term, i.e., $c_{t3} = 0$ instead of 1.2. According to Rumsey [115], there is a negligible difference between this version and the standard model, especially at high Reynolds numbers.

2.5.2 Low-Re $k - \varepsilon$ model

The standard k-ε model [116] is degenerate near walls [108], necessitating the use of wall functions. To eliminate the need for wall functions and enable integration of the model down to the wall, a VSM version is required. The simplest approach to achieve this is through the implementation of damping functions. These models can be cast in the following form [117]:

- Turbulent kinetic energy, k, equation:

$$\frac{\partial(\rho k)}{\partial t} + \frac{\partial\left(\rho k u_j\right)}{\partial x_j} = P_k + \frac{\partial}{\partial x_j}\left[\left(\mu + \frac{\mu_t}{\sigma_k}\right)\frac{\partial k}{\partial x_j}\right] - \rho\tilde{\varepsilon} - \rho D \tag{2.13}$$

  Where $P_k = \tau_{ij}^R \frac{\partial u_i}{\partial x_j}$ is the production rate of the turbulent kinetic energy.

- Modified dissipation rate, $\tilde{\varepsilon} = \varepsilon - D$, equation:

$$\frac{\partial(\rho\tilde{\varepsilon})}{\partial t} + \frac{\partial\left(\rho\tilde{\varepsilon} u_j\right)}{\partial x_j} = (C_{\varepsilon 1} f_1 P_k - C_{\varepsilon 2} f_2 \rho\tilde{\varepsilon})\frac{\tilde{\varepsilon}}{k} + \frac{\partial}{\partial x_j}\left[\left(\mu + \frac{\mu_t}{\sigma_\varepsilon}\right)\frac{\partial\tilde{\varepsilon}}{\partial x_j}\right] + \rho E \tag{2.14}$$

The eddy viscosity is computed with the following expression:

$$\mu_t = C_\mu f_\mu \rho \frac{k^2}{\tilde{\varepsilon}} \tag{2.15}$$

One example of these models is the Launder Sharma $k - \varepsilon$ model [118], which uses the following damping functions:

$$f_1 = 1$$
$$f_2 = 1 - 0.3\exp\left(-R_T^2\right), \quad R_T = \frac{k^2}{\nu\tilde{\varepsilon}}$$
$$f_\mu = \exp\left[\frac{-3.4}{(1 + R_T/50)^2}\right]$$

The terms D and E are given by:

$$D = 2\nu\left(\nabla\sqrt{k}\right)^2 = 2\nu\frac{\partial\sqrt{k}}{\partial x_j}\frac{\partial\sqrt{k}}{\partial x_j}$$

$$E = 2\nu\nu_t\left\|\nabla^2\vec{u}\right\|^2 = 2\nu\nu_t\left(\frac{\partial^2 u_i}{\partial x_j\partial x_j}\right)\left(\frac{\partial^2 u_i}{\partial x_l\partial x_l}\right)$$

At solid walls, the boundary conditions are:

$$k_{\text{wall}} = 0, \qquad \tilde{\varepsilon}_{\text{wall}} = 0$$

The model constants are as follows:

$$C_\mu = 0.09 \qquad C_{\varepsilon 1} = 1.44 \qquad C_{\varepsilon 2} = 1.92 \qquad \sigma_k = 1.0 \qquad \sigma_\varepsilon = 1.3$$

2.5.3 SST $k-\omega$ model

The SST k-ω model, developed by Menter [119], is a two-equation eddy-viscosity turbulence model. This model combines the features of both the k-ω and k-ε models. The k-ω model is used in the inner parts of the boundary layer, allowing the SST model to be integrated down to the wall through the viscous sublayer. In contrast, the k-ε model is applied in the outer part of the boundary layer to take advantage of its freestream independence and to mitigate the shortcomings of the k-ω model regarding its high sensitivity to the freestream value of ω. Other modifications include the eddy viscosity limiter to enhance the prediction of separated flows. Another slight variation of the model was introduced in 2003 [120], which is presented below:

- Turbulent kinetic energy, k, equation:

$$\frac{\partial(\rho k)}{\partial t} + \frac{\partial\left(\rho u_j k\right)}{\partial x_j} = \tilde{P}_k - \beta^*\rho k\omega + \frac{\partial}{\partial x_j}\left[(\mu + \sigma_k\mu_t)\frac{\partial k}{\partial x_j}\right] \tag{2.16}$$

- Specific dissipation rate, ω, equation:

$$\frac{\partial(\rho\omega)}{\partial t} + \frac{\partial\left(\rho u_j\omega\right)}{\partial x_j} = \alpha\frac{\tilde{P}_k}{\nu_t} - \beta\rho\omega^2 + \frac{\partial}{\partial x_j}\left[(\mu + \sigma_\omega\mu_t)\frac{\partial\omega}{\partial x_j}\right] + 2(1 - F_1)\frac{\rho\sigma_{\omega 2}}{\omega}\frac{\partial k}{\partial x_j}\frac{\partial\omega}{\partial x_j} \tag{2.17}$$

Where the blending function F_1 is given by:

$$F_1 = \tanh\left\{\left\{\min\left[\max\left(\frac{\sqrt{k}}{\beta^*\omega y}, \frac{500\nu}{y^2\omega}\right), \frac{4\rho\sigma_{\omega 2}k}{\mathrm{CD}_{k\omega}y^2}\right]\right\}^4\right\}$$

With y being the distance to the nearest wall. The cross-diffusion term is given by:

$$\mathrm{CD}_{k\omega} = \max\left(2\rho\sigma_{\omega 2}\frac{1}{\omega}\frac{\partial k}{\partial x_j}\frac{\partial \omega}{\partial x_j}, 10^{-10}\right)$$

In the near wall region, $F \to 1$, the cross-diffusion term vanishes, and k-ω model is recovered. Away from the wall, $F \to 0$, the cross-diffusion term is active, and the standard k-ε model is recovered with the change of variable $\omega = \varepsilon/(k\beta^*)$.

The turbulent eddy viscosity is computed from:

$$\mu_t = \frac{\rho a_1 k}{\max(a_1\omega, \mathrm{S}F_2)} \tag{2.18}$$

Where $a_1 = 0.31$ is a constant, and S is the invariant measure of the strain rate:

$$S = \sqrt{2S_{ij}S_{ij}}$$
$$S_{ij} = \frac{1}{2}\left(\frac{\partial u_i}{\partial x_j} + \frac{\partial u_j}{\partial x_i}\right)$$

The second blending function, F_2, is defined by:

$$F_2 = \tanh\left[\left[\max\left(\frac{2\sqrt{k}}{\beta^*\omega y}, \frac{500\nu}{y^2\omega}\right)\right]^2\right]$$

The turbulent kinetic energy production is limited:

$$\tilde{P}_k = \min(P_k, 10\beta^*\rho k\omega)$$

The production limiter is required to prevent the excessive production of turbulence in stagnation regions [112], also known as “Stagnation-point anomaly” [108].

The constants of the model are computed as a blend between C_1 (coefficients of $k-\omega$) and C_2 (coefficients of $k-\varepsilon$ model):

$$C = F_1C_1 + (1 - F_1)C_2$$

- k-ω coefficients:

$$\alpha_1 = 5/9 \qquad \beta_1 = 3/40 \qquad \sigma_{k1} = 0.85 \qquad \sigma_{\omega 1} = 0.5 \qquad \beta^* = 0.09 \qquad \kappa = 0.41$$

- $k-\varepsilon$ coefficients:

$$\alpha_2 = 0.44 \qquad \beta_2 = 0.0828 \qquad \sigma_{k2} = 1.0 \qquad \sigma_{\omega 2} = 0.856 \qquad C_\mu = \beta^* = 0.09 \qquad \kappa = 0.41$$

The boundary conditions of the model are [114]:

$$\frac{U_\infty}{L} < \omega_\infty < \frac{10U_\infty}{L}, \qquad \frac{10^{-5}U_\infty^2}{Re_L} < k_\infty < \frac{10^{-1}U_\infty^2}{Re_L}, \qquad k_{\text{wall}} = 0, \qquad \omega_{\text{wall}} = 10\frac{6\nu}{\beta_1(\Delta y_1)^2}$$

where L represents the approximate length of the computational domain and Δy_1 is the distance from the wall to the next cell center.

2.5.4 The 4-equation transitional SST model

The transition SST k-ω [121] model is referred to as $\gamma - \hat{R}e_{\theta t}$ (or simply, γ-Re_θ), is a local correlation-based model that includes two additional transport equations for the intermittency, γ, and the transition momentum thickness Reynolds number, $\hat{R}e_{\theta t}$. These equations are coupled with the SST k-ω model equations to enable the prediction of laminar-turbulent transition in wall-bounded flows. The model is capable of predicting the natural, bypass, and separation-induced transition. However, in free shear flows, the model treats the flow as being fully turbulent. The model equations are:

- Turbulent kinetic energy equation:

$$\frac{\partial(\rho k)}{\partial t} + \frac{\partial\left(\rho u_j k\right)}{\partial x_j} = \hat{P}_k - \hat{D}_k + \frac{\partial}{\partial x_j}\left[(\mu + \sigma_k \mu_t)\frac{\partial k}{\partial x_j}\right] \tag{2.19}$$

- The specific dissipation rate equation:

$$\frac{\partial(\rho\omega)}{\partial t} + \frac{\partial\left(\rho u_j \omega\right)}{\partial x_j} = P_\omega - D_\omega + \frac{\partial}{\partial x_j}\left[(\mu + \sigma_\omega \mu_t)\frac{\partial \omega}{\partial x_j}\right] + 2(1 - F_1)\frac{\rho\sigma_{\omega 2}}{\omega}\frac{\partial k}{\partial x_j}\frac{\partial \omega}{\partial x_j} \tag{2.20}$$

- The intermittency, γ, equation:

$$\frac{\partial(\rho\gamma)}{\partial t} + \frac{\partial\left(\rho u_j \gamma\right)}{\partial x_j} = P_\gamma - E_\gamma + \frac{\partial}{\partial x_j}\left[\left(\mu + \frac{\mu_t}{\sigma_f}\right)\frac{\partial \gamma}{\partial x_j}\right] \tag{2.21}$$

  The intermittency ranges from 0 to 1. A value of 0 indicates laminar flow, while a value of 1 indicates turbulent flow. Values in between represent transition.

- The equation for the transition momentum-thickness Reynolds number, $\hat{R}e_{\theta t}$:

$$\frac{\partial\left(\rho\hat{R}e_{\theta t}\right)}{\partial t}+\frac{\partial\left(\rho u_j\hat{R}e_{\theta t}\right)}{\partial x_j}=P_{\theta t}+\frac{\partial}{\partial x_j}\left[\sigma_{\theta t}(\mu+\mu_t)\frac{\partial\hat{R}e_{\theta t}}{\partial x_j}\right] \tag{2.22}$$

The source terms in the k equation of the SST model (i.e., $\tilde{P}_k$ and $D_k=\beta^*\rho k\omega$ in eq. (2.16)) are modified to introduce the effects of the laminar-turbulent transition (The subscript 'SST' is added for clarity):

$$\begin{aligned}
&\hat{P}_k=\gamma_{\text{eff}}\tilde{P}_{k,\text{SST}}\\
&\hat{D}_k=\min(\max(\gamma_{\text{eff}},0.1),1.0)D_{k,\text{ SST}}\\
&\gamma_{\text{eff}}=\max\left(\gamma,\gamma_{\text{sep}}\right)\\
&\gamma_{\text{sep}}=\min\left(s_1\max\left[0,\left(\frac{Re_V}{3.235Re_{\theta c}}\right)-1\right]F_{\text{reattach}},2\right)F_{\theta t}\\
&F_{\text{reattach}}=\exp\left(-\left(\frac{R_T}{20}\right)^4\right)
\end{aligned}$$

The blending function F_1 in the SST model is modified as well:

$$\begin{aligned}
R_y&=\frac{\rho y\sqrt{k}}{\mu}\\
F_3&=\exp\left[-\left(\frac{R_y}{120}\right)^8\right]\\
F_1&=\max\left(F_{1,\text{SST}},F_3\right)
\end{aligned}$$

The source terms for the intermittency equation are defined as:

$$\begin{aligned}
P_\gamma&=F_{\text{length}}c_{a1}\rho S\left[\gamma F_{\text{onset}}\right]^{0.5}(1-c_{e1}\gamma)\\
E_\gamma&=c_{a2}\rho\Omega\gamma F_{\text{turb}}(c_{e2}\gamma-1)
\end{aligned}$$

with

$$\begin{aligned}
Re_V&=\frac{\rho S y^2}{\mu}\\
F_{\text{onset}}&=\frac{Re_V}{2.193Re_{\theta c}}
\end{aligned}$$

$$Re_{\theta c}=\begin{cases}\left[\hat{R}e_{\theta t}-\left(396.035\cdot10^{-2}+\left(-120.656\cdot10^{-4}\right)\hat{R}e_{\theta t}+\right.\right.\\ \left.+\left(868.230\cdot10^{-6}\right)\hat{R}e_{\theta t}^2+\left(-696.506\cdot10^{-9}\right)\hat{R}e_{\theta t}^3+\right.\\ \left.\left.+\left(174.105\cdot10^{-12}\right)\hat{R}e_{\theta t}^4\right)\right], & \hat{R}e_{\theta t}\le1870\\ \left[\hat{R}e_{\theta t}-\left(593.11+\left(\hat{R}e_{\theta t}-1870.0\right)\cdot0.482\right)\right] & \hat{R}e_{\theta t}>1870\end{cases}$$

$$
\begin{aligned}
F_{\text{onset2}} &= \min\left(\max\left(F_{\text{onset1}}, F_{\text{onset1}}^4\right), 2.0\right) \\
R_T &= \frac{\rho k}{\mu \omega} \\
F_{\text{onset3}} &= \max\left[1 - \left(\frac{R_T}{2.5}\right)^3, 0\right] \\
F_{\text{onset}} &= \max(F_{\text{onset2}} - F_{\text{onset3}}, 0) \\
F_{\text{turb}} &= \exp\left[-\left(\frac{R_T}{4}\right)^4\right] \\
F_{\text{length}} &= F_{\text{length1}}\left(1 - F_{\text{sublayer}}\right) + 40.0 F_{\text{sublayer}} \\
F_{\text{sublayer}} &= \exp\left[-\left(\frac{Re_\omega}{200}\right)^2\right] \\
Re_\omega &= \frac{\rho \omega y^2}{\mu}
\end{aligned}
$$

$$
F_{\text{length1}} = \begin{cases}
39.8189 + \left(-119.270 \cdot 10^{-4}\right)\hat{R}e_{\theta t} + \left(-132.567 \cdot 10^{-6}\right)\hat{R}e_{\theta t}^2, & \hat{R}e_{\theta t} < 400; \\
263.404 + \left(-123.939 \cdot 10^{-2}\right)\hat{R}e_{\theta t} + \left(194.548 \cdot 10^{-5}\right)\hat{R}e_{\theta t}^2 + & \\
+\left(-101.695 \cdot 10^{-8}\right)\hat{R}e_{\theta t}^3, & 400 \le \hat{R}e_{\theta t} < 596; \\
0.5 - \left(3.0 \cdot 10^{-4}\right)\left(\hat{R}e_{\theta t} - 596.0\right), & 596 \le \hat{R}e_{\theta t} < 1200; \\
0.3188 & 1200 \le \hat{R}e_{\theta t}
\end{cases}
$$

The source term in the $\hat{R}e_{\theta t}$is defined as follows:

$$
\begin{aligned}
P_{\theta t} &= c_{\theta t} \frac{\rho}{\tau}\left(Re_{\theta c} - \hat{R}e_{\theta t}\right)(1.0 - F_{\theta t}) \\
\tau &= \frac{500\mu}{\rho U^2} \\
U &= \sqrt{u_k u_k} \\
F_{\theta t} &= \min\left[\max\left(F_{\text{wake}} \exp\left(-\left(\frac{d}{\delta}\right)^4\right), 1.0 - \left(\frac{c_{e2}\gamma - 1}{c_{e2} - 1}\right)^2\right), 1.0\right] \\
F_{\text{wake}} &= \exp\left[-\left(\frac{Re_\omega}{10^5}\right)^2\right] \\
\delta &= \frac{375 \Omega \mu \hat{R}e_{\theta t} y}{\rho U^2}
\end{aligned}
$$

$$\lambda_\theta = \frac{\rho\theta_t^2}{\mu}\frac{\mathrm{d}U}{\mathrm{d}s}$$
$$\frac{\mathrm{d}U}{\mathrm{d}s} = \frac{u_m u_n}{U^2}\frac{\partial u_m}{\partial x_n}$$
$$\mathrm{TI} = 100\frac{\sqrt{2k/3}}{U}$$

$$Re_{\theta t}^{\mathrm{eq}} = \begin{cases} \left(1173.51 - 589.428\mathrm{TI} + 0.2196(\mathrm{TI})^{-2}\right)F(\lambda_\theta), & \mathrm{TI} \le 1.3 \\ 331.50(\mathrm{TI} - 0.5658)^{-0.671}F(\lambda_\theta), & \mathrm{TI} > 1.3 \end{cases}$$

$$F(\lambda_\theta) = \begin{cases} 1 + \left[12.986\lambda_\theta + 123.66\lambda_\theta^2 + 405.689\lambda_\theta^3\right]\exp\left[-\left(\frac{\mathrm{TI}}{1.5}\right)^{1.5}\right], & \lambda_\theta \le 0 \\ 1 + 0.275\left[1 - \exp(-35.0\lambda_\theta)\right]\exp\left(-\frac{\mathrm{TI}}{0.5}\right) & \lambda_\theta > 0 \end{cases}$$

The model constants are:

$c_{a1} = 2.0$	$c_{a2} = 0.06$	$c_{e1} = 1.0$	$c_{e2} = 50$
$c_{\theta t} = 0.03$	$s_1 = 2$	$\sigma_f = 1.0$	$\sigma_{\theta t} = 2.0$

The boundary conditions for the two additional equations, γ and $\hat{R}e_{\theta t}$ are:

$$\gamma_\infty = 1$$
$$\left.\frac{\partial\gamma}{\partial n}\right|_{\mathrm{wall}} = 0$$
$$\left.\frac{\partial\hat{R}e_{\theta t}}{\partial n}\right|_{\mathrm{wall}} = 0$$
$$\hat{R}e_{\theta t,\infty} = \begin{cases} \left(1173.51 - 589.428\mathrm{TI}_\infty + 0.2196(\mathrm{TI}_\infty)^{-2}\right), & \mathrm{TI}_\infty \le 1.3 \\ 331.50(\mathrm{TI}_\infty - 0.5658)^{-0.671}, & \mathrm{TI}_\infty > 1.3 \end{cases}$$

To ensure numerical stability, the subsequent constraints are applied:

$$-0.1 \le \lambda_\theta \le 0.1 \qquad \mathrm{TI} \ge 0.027 \qquad Re_{\theta t}^{\mathrm{eq}} \ge 20$$

The governing equations and turbulence models presented in this chapter form the mathematical foundation for fluid flow analysis. These numerical methods are applied in the next chapter to study the dynamic stall and related unsteady aerodynamic phenomena in more detail.

Chapter 3

Numerical Modeling and Experimental Studies

3.1 Introduction

Building upon the computational framework established in the previous chapter, here we present the application of these methodologies for the investigation of the complex unsteady aerodynamic phenomena relevant to VAWTs operation, particularly at low tip speed ratios, focusing on the dynamic stall phenomenon. Following this, these methodologies are also applied to the study of VAWT wake dynamics. The first section evaluates various RANS turbulence models in predicting dynamic stall. The subsequent section tackles the estimation of the AoA and the relative velocity on VAWT blades from CFD computations, providing a better comprehension of VAWT aerodynamic performance in relation to airfoil characteristics. This includes considering the impact of laminar-turbulent transition in the simulations. Finally, the chapter presents a study where multiple RANS models are employed in numerical simulations alongside PIV experiments to characterize the wake dynamics of VAWTs.

3.2 Evaluating RANS models for deep dynamic stall prediction

3.2.1 Motivation

As previously discussed in section 1.4.2, much of the research on dynamic stall has concentrated on oscillating airfoils. This is particularly relevant to VAWTs, where the variation in the AoA of the blades resembles a sine-curve. This similarity provides a rationale for exploring dynamic stall in VAWTs by studying oscillating airfoils. It is important to note, however, that the motion of VAWT blades includes elements not present in the oscillating airfoil model, such as plunging motion. Despite these differences, the study of dynamic stall in oscillating airfoils remains relevant and valuable for understanding the aerodynamic behavior of VAWT blades [122].

In the context of dynamic stall modeling, relying on simplified models offers very limited usefulness. Dynamic stall is characterized by complex flow phenomena such as flow separation, recirculation, and the formation of vortices, which cannot be adequately captured by simplified aerodynamic models. For accurate modeling of dynamic stall, Leishman [123] concluded that this phenomenon can be accurately modeled only through the application of full Navier-Stokes equations, complemented by an appropriate turbulence model.

VAWTs often employ thicker airfoils such as NACA 0015, which are necessary for improved blade stiffness and maintaining uniform blade loading during oscillation between negative and positive AoAs [124]. Despite their importance in VAWTs, the aerodynamic performance of these thicker airfoils in deep dynamic stall has not been as extensively studied as relatively thinner airfoils like NACA0012 [107]. Furthermore, most of numerical studies examining dynamic stall have utilized commercial software, including Ansys Fluent (Refs. [85,125]) or in-house codes (Refs. [126,127]). Addressing those gaps, the current study employs the open-source software OpenFOAM [128] to assess the effectiveness of three URANS turbulence models: k-ω SST, Spalart-Allmaras, and Launder-Sharma k-ε models, to predict the complex unsteady flow of deep dynamic stall [107].

3.2.2 Problem description

The present study focuses on a NACA0015 airfoil subjected to a sinusoidal pitching motion about an axis located at a one-quarter chord from its leading edge. The AoA follows a prescribed function, $\alpha(t) = 17 + 5\sin(\Omega t)$, at a reduced frequency, $\kappa = \Omega c/2U_\infty = 0.1$. The freestream Reynolds number, based on the airfoil chord, is $Re_c = 1.95 \times 10^6$, with a Mach number of $Ma = 0.278$. These conditions replicate the most severe testing conditions in the experimental investigations of Piziali [94] conducted in the 7-by-10-foot subsonic wind tunnel at the NASA Ames Research Center. The boundary layer is tripped at the leading edge of the airfoil to ensure its transition to a fully turbulent state over the airfoil.

2D URANS simulations were conducted using the three aforementioned turbulence models to study the deep dynamic stall. Additionally, 18 steady-state simulations were carried out using k-ω SST model under the same freestream conditions of the dynamic cases to determine the static stall angle of the NACA0015 airfoil. The details are provided below.

3.2.3 Dynamic cases

The 2D computational domain for the unsteady simulations is divided into two zones, as depicted in Figure 3.1. It includes an oscillating circular zone with a radius of 2.5c, which is linked to a static rectangular zone through a sliding interface. In OpenFOAM, this is achieved using the Arbitrary Mesh Interface (AMI). The dimensions of the computational domain are $40c$ in width and $130c$ in length. The inlet is positioned $30c$ upstream from the airfoil's leading edge, and the outlet is situated $100c$ downstream. The top and bottom boundaries are

positioned 20*c* away from the center of the oscillating zone. These distances are adequately large to prevent the artificial influence of the boundaries being too close to the airfoil and to permit the wake to develop completely downstream of the airfoil. To guarantee a high-quality grid for URANS computations, especially in the oscillating region, considerable attention was devoted to the mesh generation process. This involved using both hyperbolic and elliptic methodologies, supplemented by Radial Basis Functions (RBF). Initially, the grid surrounding the airfoil was created using the hyperbolic marching technique. This method offers multiple advantages; notably, it is significantly quicker (by a factor of 10 to 100) than the elliptic method and yields almost orthogonal grids [129].

Table 3.1: Main parameters of the dynamic stall computations.

Parameter	**Value**
Airfoil	NACA 0015
Chord length, c	0.3048 m
Oscillation amplitude, α_1	5°
Mean angle of attack, α_m	17°
Angular frequency, Ω	20 π rad/s
Reduced Frequency, κ	0.1
Reynolds number, Re_c	1.95×10^6
Mach number, Ma	0.278

However, precisely defining the outer boundary to create an exact circular zone, required for the sliding mesh method, is not straightforward. To resolve this difficulty, Radial Basis Functions [130] were applied to adjust the grid into a precise circular shape. Afterward, a custom elliptic solver was utilized to further improve the quality of the grid.

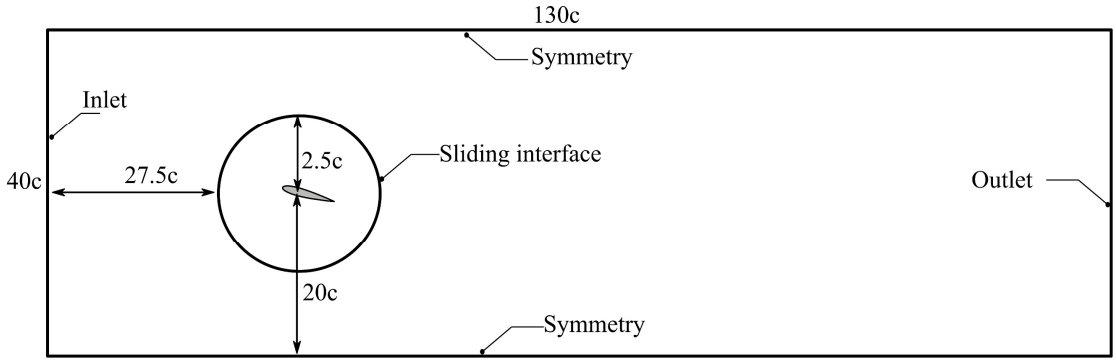

Figure 3.1: The computational domain.

In the reference grid, 500 grid points were used along the airfoil's surface and clustered at both leading and trailing edges. The height of the first cell layer, normal to the wall, was set to $5.65 \times 10^{-6}c$ to adequately resolve the boundary layer keeping a y^+ values below one. The growth rate of cells normal to the airfoil surface was fixed at 1.1. The reference grid is depicted in Figure 3.2a, which includes detailed views of the oscillating zone (Figure 3.2b), the grid around the airfoil (Figure 3.2c), and near the leading edge of the airfoil (Figure 3.2d), and a view of the rounded trailing-edge as shown in Figure 3.2e. The grid referenced in the figures is, in fact, a coarser version selected for clearer representation in these illustrations.

3.2.4 Boundary conditions

Consistent with the 2D experiments conducted by Piziali [94], the present URANS simulations employ a NACA0015 airfoil with a chord length of $c = 0.3048$ m. This airfoil undergoes a sinusoidal oscillation around its quarter-chord axis ($x/c = 25\%$). The mean angle of attack, α_m, is set at 17°, with an amplitude of 5°, hence $\alpha(t) = 17 + 5\sin(\Omega t)$. The reduced frequency is 0.1.

At the inlet of the domain, the freestream Mach number is $\mathrm{Ma} = 0.278$, and the Reynolds number computed based on the airfoil's chord length is $Re_c = 1.95 \times 10^6$. Although the freestream turbulence intensity was not reported in the experiment, according to Storms et al. [131], the longitudinal turbulence level is 0.25% in the wind tunnel at $\mathrm{Ma} = 0.22$. Therefore, this value is used in the present study. These parameters are summarized in Table 3.1.

With the assumption that there is no variation in flow variables and that the flow remains parallel at both the top and bottom of the computational domain, symmetry boundary conditions are applied along these edges. A no-slip moving wall condition is imposed on the airfoil surface. The circular zone enclosing the airfoil is set to undergo a sinusoidal motion using the *oscillatingRotatingMotion* function in OpenFOAM.

A similar configuration is employed for the case wherein the airfoil undergoes oscillatory pitching about its mid-chord axis.

3.2.5 Static cases

For the determination of the static stall AoA of the NACA0015 airfoil under the same freestream conditions of the dynamic cases, 2D steady RANS computations were conducted.

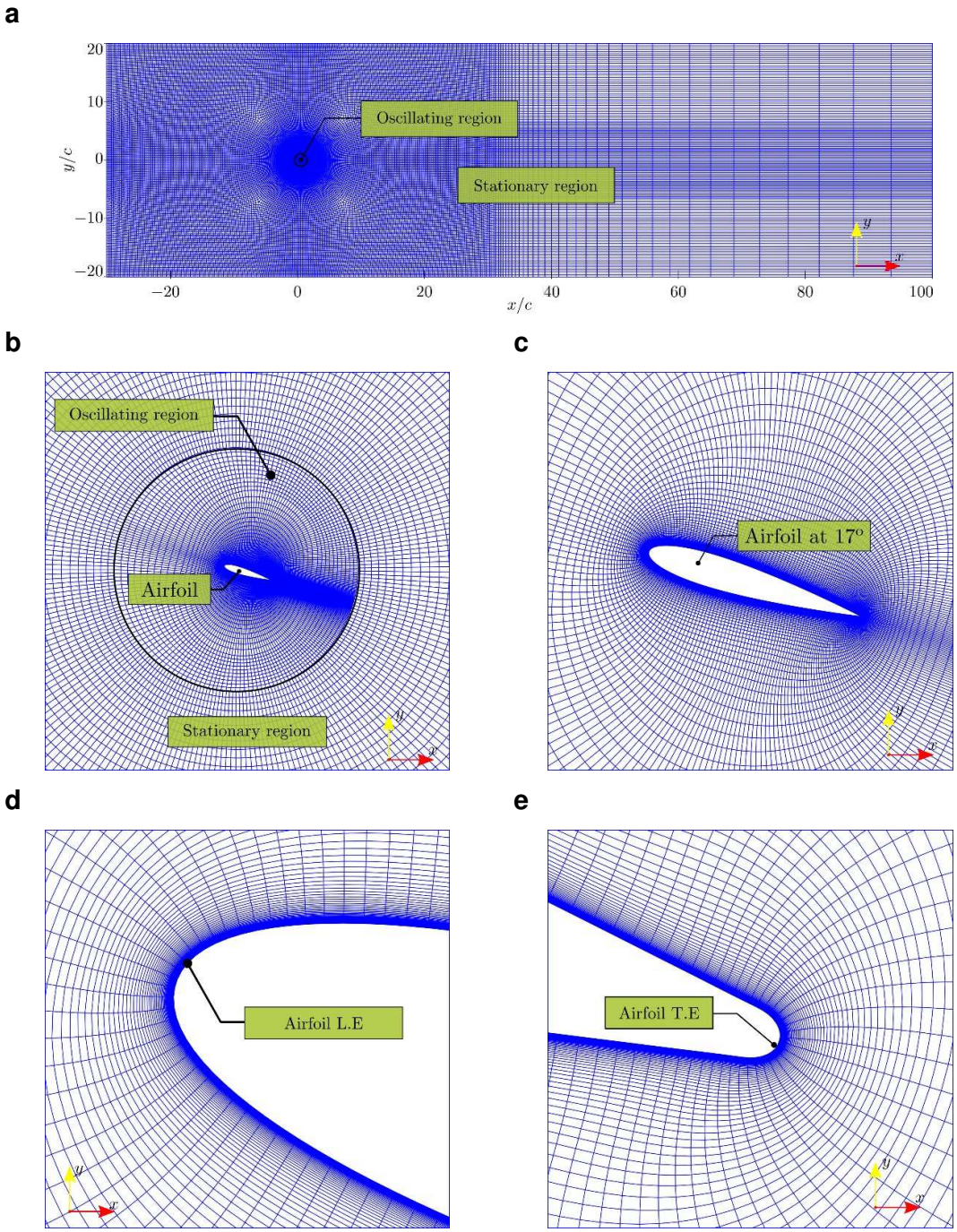

Figure 3.2: Computational grid used in the simulations. (a) Dimensions of computational domain. (b) view of the grid around the oscillating zone. (c) Layout of the grid in the vicinity of the airfoil. (d) and (e): The grid layout near the leading and trailing edges respectively. For static simulations, an identical grid is employed, but without grid motion.

The AoA is varied from 0° to 18° in 1° increments. The results of these simulations are validated against the experimental measurement of Piziali [94]. In these experiments, a NACA0015 airfoil with a tripped boundary layer at its leading edge is pitched at a reduced frequency low enough to categorize the stall as static. The computational domain used was static for each AoA, identical to the one employed in the dynamic case simulations but with the appropriate boundary conditions.

3.2.6 Numerical procedure

It is well established by experimental investigations [101,132,133] that compressibility effects in dynamic stall phenomenon become important for freestream Mach numbers greater or equal to 0.2. The flow acceleration that occurs around the leading edge of the airfoil can result in velocities much greater than the freestream values. Therefore, we opted to utilize a compressible solver for this study. The governing equations of 2D compressible flows, presented in Chapter 2, are solved using a URANS approach coupled with the turbulence models mentioned earlier. These equations are discretized and integrated through the finite volume method within OpenFOAM. For steady-state and unsteady simulations involving dynamic mesh, *rhoSimpleFoam,* and *rhoPimpleFoam* solvers are employed, respectively. The pressure-velocity-energy coupling in the simulations is achieved using the PIMPLE algorithm, a hybrid of the PISO [134] and SIMPLE [135] algorithms. To ensure stability, all unsteady computations initially employed first-order schemes during the initial time steps, subsequently transitioning to second-order accurate schemes for the temporal and spatial terms. The time step is automatically adjusted to maintain a maximum Courant number of 0.6, a value determined based on sensitivity analysis using maximum Courant numbers of 0.5, 0.6, and 0.7. The choice of 0.6 for all computations is made after observing no significant changes between 0.5 and 0.6. These simulations are executed on 92 AMD OpteronTM 6174 2.2 GHz cores within the Mammouth Parallèle II cluster, part of the Compute Canada network.

3.2.7 Convergence of the simulations

To conduct a grid convergence study for the unsteady computations, four grids, labeled Grid 1 through Grid 4 (see Table 3.2), were created, each maintaining identical topology and dimensions of the computational domain of Figure 3.1. The number of cells in each grid varies by a factor of $\sqrt{2}$ along both streamwise and normal directions. This approach led to the creation of three additional grids besides the reference grid (Grid 3), which contains

296748 cells: Grid 1 with 124866 cells, Grid 2 with 187650 cells, and Grid 4 with 478476 cells. The rate at which the cell size increases from the airfoil surface is consistent across all grids.

Table 3.2: Details of the different computational grids.

Grid	y_1	**Growth rate**	**Points on airfoil**	**No. cells**
Grid 1	1.13×10^{-5} c	1.1	250	124866
Grid 2	8.00×10^{-6} c	1.1	354	187650
Grid 3	5.65×10^{-6} c	1.1	500	296748
Grid 4	4.00×10^{-6} c	1.1	708	478476

The ensemble-averaged hysteresis loops of the airfoil's lift coefficient, C_l, over the last five cycles are depicted in Figure 3.3. These results from URANS computations, using the k-ω SST model on the four grids, are compared with the experimental findings of Piziali [94]. The C_l predictions using Grid 1 exhibit notable variances from those of the other grids during both the upstroke and downstroke phases of the oscillation cycle. Particularly in the post-stall regime of the downstroke phase, the results from Grid 1 and Grid 2 significantly diverge from those obtained with Grid 3 and Grid 4. Conversely, during the upstroke phase, the lift coefficient values from Grids 2, 3, and 4 align closely, showing nearly identical trends. Upon detailed analysis of the flow fields from Grid 3 and Grid 4, no substantial differences are discerned, although minor discrepancies in C_l are noted immediately following stall, attributed to the complex unsteady flow behavior during post-stall [136]. As the AoA decreases, the discrepancy in C_l between Grid 3 and Grid 4 diminishes, suggesting that a grid-independent solution is effectively achieved with Grid 3. This grid offers a balance between computational efficiency and accuracy. Therefore, Grid 3 is also selected for subsequent simulations utilizing the Spalart-Allmaras (SA) and Launder-Sharma k-ε models.

Table 3.3: Convergence of lift and pitching moment coefficients between consecutive oscillation cycles.

Std. deviation, σ (%)	σ_1	σ_2	σ_3	σ_4	σ_5	σ_6
Lift coefficient	6.17	0.02	0.011	0.011	0.01	0.01
Moment coefficient	4.32	0.01	0.01	0.00	0.00	0.00

Figure 3.4 illustrates the variation of the moment coefficient, C_m , over time. The convergence of the computations is assessed by comparison of the standard deviation of the aerodynamic

coefficients, specifically C_l and C_m, between consecutive oscillation cycles, as detailed in Table 3.3. While there is a discernible difference in the aerodynamic coefficients between the first and second oscillation cycles, this difference diminishes in subsequent cycles starting from the second. This pattern suggests the attainment of a statistically steady-state. The aerodynamic coefficients are averaged over five oscillation cycles, where the period is given by $T = 2\pi/\Omega$. However, it is worth mentioning that the experimental results of Piziali [94] were ensemble-averaged over 20 cycles.

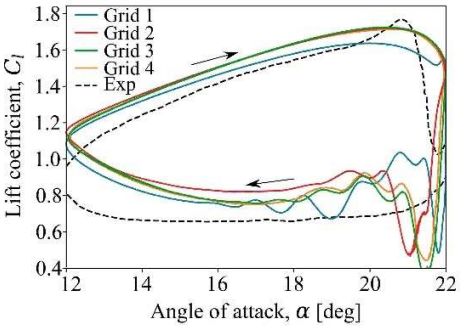

Figure 3.3: Lift coefficient obtained using different grid densities employing the *k-ω* SST model.

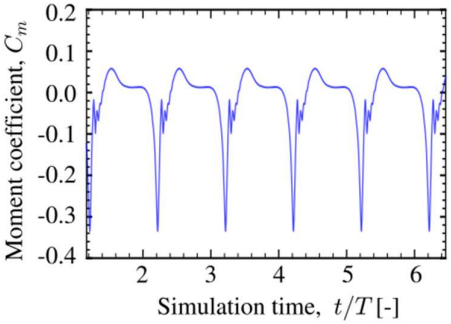

Figure 3.4: history of pitching moment coefficient over time, *t/T* using the reference Grid with *k-ω* SST model.

3.3 Estimating VAWT Blade AoA and relative velocity from CFD Data

3.3.1 Motivation

The primary motivation of this study is to elucidate the complex aerodynamics associated with the operation of VAWTs. As mentioned in Chapter 1, the blades of VAWTs exhibit continuously changing AoA with alternating signs during their rotations. This leads to dynamic stall when the static stall angles are exceeded and to potential blade-vortex interactions in the downwind side of the rotation [137]. Since CFD computations are required for such complex flows, the calculation of the aerodynamic forces acting on the blades is straightforward through the integration of pressure and shear forces. However, resolving these forces in terms of lift and drag is more practical, which requires the definition of the blade's AoA. Knowledge of the relative velocity is essential to express these forces as non-dimensional coefficients. Many studies accomplish this by assuming a geometric relationship

(see Eq. 1.1) between the blade's tangential velocity and the freestream velocity vectors. This simple approach does not consider the turbine thrust force on the incoming freestream velocity and the blade-wake interactions. Neglecting to consider these effects leads to an inaccurate representation of the lift and drag forces of the blades.

Edwards et al. [63] proposed an approach for estimating the VAWT blade's AoA based on an averaged velocity field from 36 different blade locations throughout a full turbine rotation. This also requires the interpolation of the flow fields after removing the circumferential region in the vicinity of the blades. Bianchini et al. [138] used a method combining virtual camber theory and an airfoil in curved flow to match pressure distribution. Nevertheless, this is not applicable across the full rotation. Rezaeiha et al. [77] implemented a method based on sampling flow velocity on a virtual circle shifted upstream by 20% of the turbine diameter. This distance is determined through trial and error such that the bound circulation on the blade has the slightest impact on the incoming velocity. Gosselin [139] proposed a method to sample the velocity at a virtual point on the blade trajectory, located two chord lengths from the blade. Elsakka et al. [140] suggested a method that samples the velocity at two reference points, each one chord length away on either side of the blade and half a chord length ahead.

Most of these methods require several intermediate steps to implement, and relatively extensive post-processing efforts are required to estimate the AoA and relative velocity. The last two methods are implemented as *function objects* within OpenFOAM to:

- Automate the process of AoA and relative velocity estimations.
- Facilitate the evaluation of the effectiveness of these methods.
- Gain insight into the complex flow characteristics associated with VAWT operation, specifically focusing on the dynamic stall and blade-vortex interactions.
- Evaluate the URANS turbulence models to simulate low-Reynolds number flows with laminar-to-turbulence transition in the boundary layers.
- Evaluate the applicability of OpenFOAM for simulating these flows, considering that the majority of studies in the literature have relied on commercial software such as Ansys Fluent and StarCCM+.

For this analysis, 2D URANS simulations were conducted to study the blade aerodynamics of a small VAWT at TSR = 2.08 and an average freestream Reynolds number based on the blade

chord, $Re_c \approx 2.26 \times 10^4$. The simulations were coupled with the two turbulence models: k-ω SST and the four-equation model with transition γ-Re_θ models [141].

3.3.2 Analysis with induction effect

The thrust force exerted by the VAWT decreases the incoming velocity, U_∞, and causes expansion of the streamtube. Consequently, the induced velocity, U_{ind}, is non-zero (refer to Figure 3.5). The relative velocity vector is determined by the vector sum of the freestream velocity, the velocity of the blade, and the induced velocity [142].

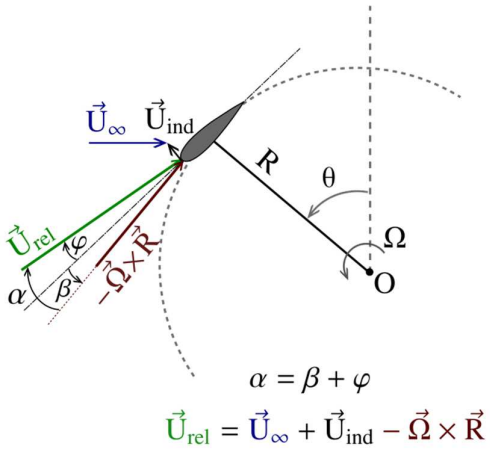

Figure 3.5: The actual velocity triangle on a VAWT blade, considering the influence of induction.

As previously discussed, the precise determination of the AoA and the relative velocity magnitude cannot be obtained through basic aerodynamic analysis. Consequently, comprehensive CFD data is necessary for a reasonable estimation of these quantities. In this study, two methods are employed for this purpose: Gosselin [139] (denoted by method 1) and Elsakka et al. [140] (denoted by method 2) methods are implemented. The underlying principles of these methods are outlined below.

3.3.3 Estimation of AoA from CFD data

The approach for calculating the blade's AoA, as suggested by Gosselin [139], is depicted in Figure 3.6. This technique determines the AoA by monitoring the average velocity along the blade's trajectory at a virtual location at least two blade chord lengths ahead.

The approach proposed by Elsakka et al. [140] determines the blade's AoA based on the average velocity monitored at two reference points. These points are positioned one chord

length from each side of the blade and half a chord upstream. The location of the reference points, P_1 and P_2, are shown in Figure 3.7.

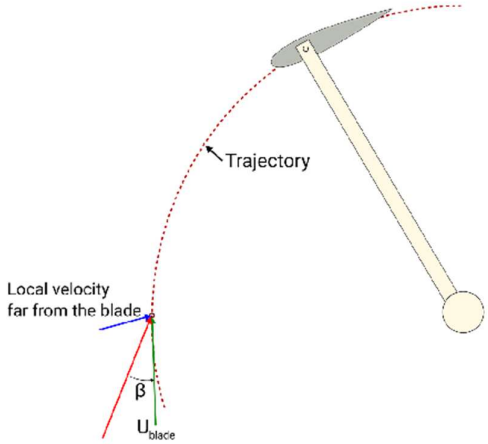

Figure 3.6: The approach proposed by Gosselin [139] for the determination of AoA. Redrawn from the same reference.

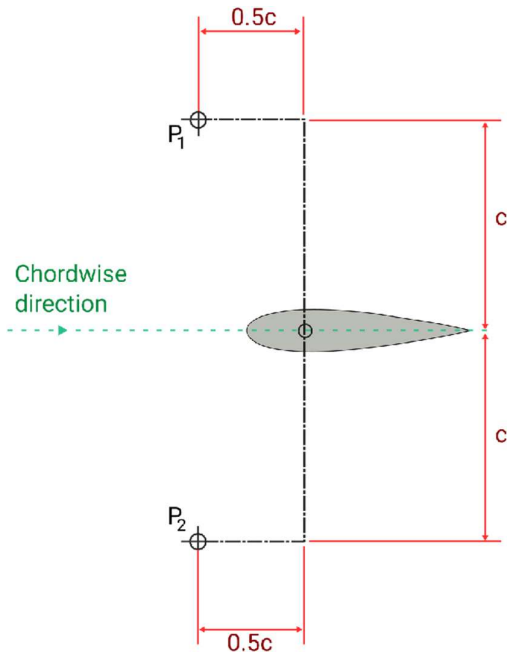

Figure 3.7: The approach proposed by Elsakka et al. [140] for the determination of AoA. Redrawn from same reference.

Implementing these two methods as *function objects* within OpenFOAM enables real-time and post-simulation monitoring of the blade's AoA and relative velocity magnitude. This

allows to resolve the aerodynamic forces exerted on the blades into lift, F_l, and drag, F_d, forces. Consequently, the lift and drag coefficients could also be computed throughout the full rotation cycle. The 2D coefficients, expressed per unit span, are defined as follows:

- Dynamic lift coefficient:

$$C_l = \frac{2F_l}{\rho c U_{\text{rel}}^2} \tag{3.1}$$

Where ρ is the fluid density.

- Dynamic drag coefficient:

$$C_d = \frac{2F_d}{\rho c U_{\text{rel}}^2} \tag{3.2}$$

The torque coefficient per unit span, C_q, of the blade about the turbine axis is given by:

$$C_q = \frac{Q}{\rho U_\infty^2 R^2} \tag{3.3}$$

where Q is the blade' torque.

The execution of the implemented function object is controlled through input parameters in a textual format, similar to the typical workflow in OpenFOAM (see Figure 3.8).

3.3.4 Numerical Simulations

3.3.4.1 Modeled VAWT

In the present study, a small VAWT with two blades ($N = 2$) is considered. This VAWT has a radius $R = 0.125$ m and a blade chord length $c = 0.04$ m, which results in a turbine solidity $\sigma = Nc/2R = 0.32$. The blades utilize a symmetric NACA0018 airfoil and are pitched at an angle of $\beta = -2°$. The average Re calculated based on the chord length is $Re_c = 2.26 \times 10^4$.

The selected configuration has a relatively high solidity and low TSR ($\lambda = 2.08$), ensuring that the blade encounters dynamic stall conditions and potential blade-vortex interactions.

```
type              VAWT_AoA; // Name of the FunctionObject.
libs              ("libVAWT_AoAFunctionObject.so"); // Name of the library.
enabled           true; // Toggle the function object on or off.
method            <method name>; // Name of the method.
toeInPitchSign    <sign>; // positive or negative.
radius            0.125; // Radius of the VAWT in meters.
pitchAngle        2.0; // Pitch angle of the blades in degrees.
CofR              (0 0 0.005); // Rotation center of the VAWT.
omegaRPM          650; // Set the angular velocity of the VAWT in RPM.
cellZone          <cell zone name>; // Name of the cell zone for probing.
log               false; // Enable/disable printing of basic information.
debug             false; // Enable/disable verbose output.
writeDebugFields false; // Enable/disable writing of fields for debugging.
```

Figure 3.8: The required input for the function object.

The 2D simulations are performed in the mid-plane cross-section of the turbine, considering the presence of the rotor shaft. The geometric parameters of the turbine and the operating conditions are presented in Table 3.4.

Table 3.4: Geometric parameters and operating conditions of the mini-VAWT.

Parameter	**Value**
Airfoil	NACA0018
Number of blades, N [-]	2
Aspect ratio, h/d [-]	1
Shaft diameter [m]	0.015
Chord, c [m]	0.04
Diameter, d [m]	0.25
Solidity, σ [-]	0.32
Tip speed ratio, λ [-]	2.08
Rotational speed, Ω [rpm]	650
Freestream velocity, U_∞[m/s]	4.09
Freestream turbulence intensity, TI [%]	0.5

3.3.4.2 Computational domain and grid

The computational domain (illustrated in Figure 3.9) consists of two regions: an inner rotating region with a diameter of $2d$ and an outer stationary region with dimensions of $40d$ by $7d$.

The two regions are connected through a sliding interface boundary condition. The inlet and outlet boundaries are located at distances of 10d and 30d, respectively, from the rotation axis of the VAWT. Following the convention of Ferreira [33], the azimuthal angle, θ, is divided into four quadrants: windward ($315° \leq \theta < 45°$), upwind ($45° \leq \theta < 135°$), leeward ($135° \leq \theta < 225°$), and downwind ($225° \leq \theta < 315°$).

Figure 3.10 depicts the computational grid, which utilizes a structured multi-block grid with quadrilateral cells. To fully resolve the boundary layers on the airfoils and the rotor shaft, y^+ values below one are maintained. A grid sensitivity study is performed to obtain solutions that are independent of the grid resolution.

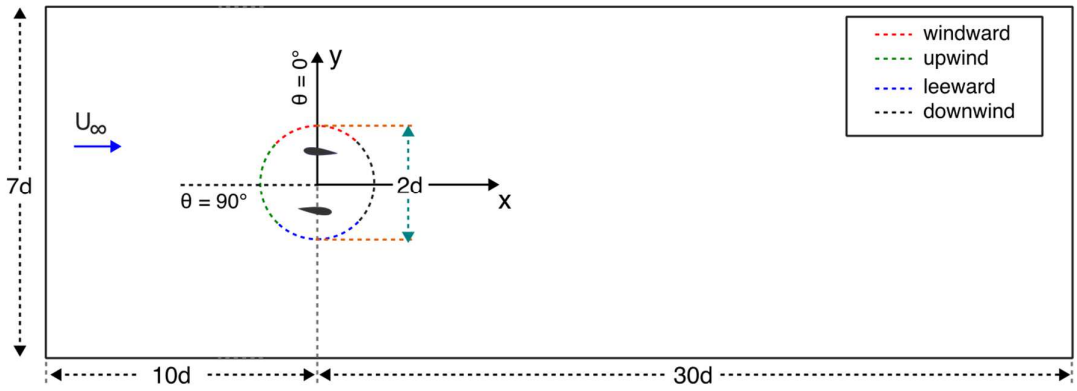

Figure 3.9: Schematic of the computational domain. The blade that is initially at $\theta = 0°$ is referred to as "blade 1". Dimensions are not to scale.

3.3.4.3 Numerical setup

In this study, numerical simulations are performed using *pimpleFoam* solver within the OpenFOAM v2106 framework based on the finite-volume method. The discretized form of the incompressible URANS equations is solved using second-order accurate schemes for temporal and spatial terms. The coupling between pressure and velocity is handled through the PIMPLE algorithm. This algorithm is configured to execute up to 30 outer correction iterations, governed by convergence criteria set at 10^{-6} for all flow variables.

At the inlet boundary, a constant velocity is prescribed, while a zero-gauge pressure condition is applied at the domain outlet. The lateral boundaries of the domain are treated as symmetry planes. The moving non-slip conditions are imposed on the airfoils and the turbine shaft.

The two-equation k-ω SST and the four-equation transition γ-Re_θ k-ω SST models are employed for turbulence closure. At the inlet boundary, a freestream turbulence intensity of 0.5% is specified. In the subsequent discussions, The CFD results corresponding to each turbulence model are denoted as SST and SSTLM, respectively (see Table 3.5).

To obtain statistically converged results, the simulations are carried out for an extended duration, spanning 26 full turbine revolutions.

Table 3.5: The models used for turbulence closure in the numerical simulations.

Turbulence model	**Abbreviation**	**Number of equations**	**Transition modeling**
k-ω SST	SST	2	No
γ-Re_θ k-ω SST	SSTLM	4	Yes

3.3.4.4 Static stall

The XFOIL software [143] is used to determine the static stall angle, α_{ss}, of the NACA0018 airfoil under comparable flow conditions. For this static stall analysis, an average Re_c is considered only over the windward quadrant, as the AoA range of interest falls within that quadrant., as will be illustrated in the results chapter.

To incorporate the influence of freestream turbulence intensity on the boundary layer transition from laminar-to-turbulent, the amplification factor, N_{crit}, of the e^N method employed by the software is adjusted using the following formula [144]:

$$N_{\text{crit}} = -8.43 - 1.4 \cdot \ln\left(\frac{2.5}{100}\tanh\left(\frac{\text{TI}\%}{2.5}\right)\right) \tag{3.4}$$

3.3.5 Grid convergence study

Four grids are employed to carry out a grid convergence study, as depicted in Table 3.6. The effect of grid refinement on the results is illustrated in Figure 3.11, which visualizes the blade's torque coefficient variation for the last rotation cycle. Since there are no notable changes between the results from Grid 3 and Grid 4, Grid 3 is chosen as the reference grid, ensuring that the results are grid-independent.

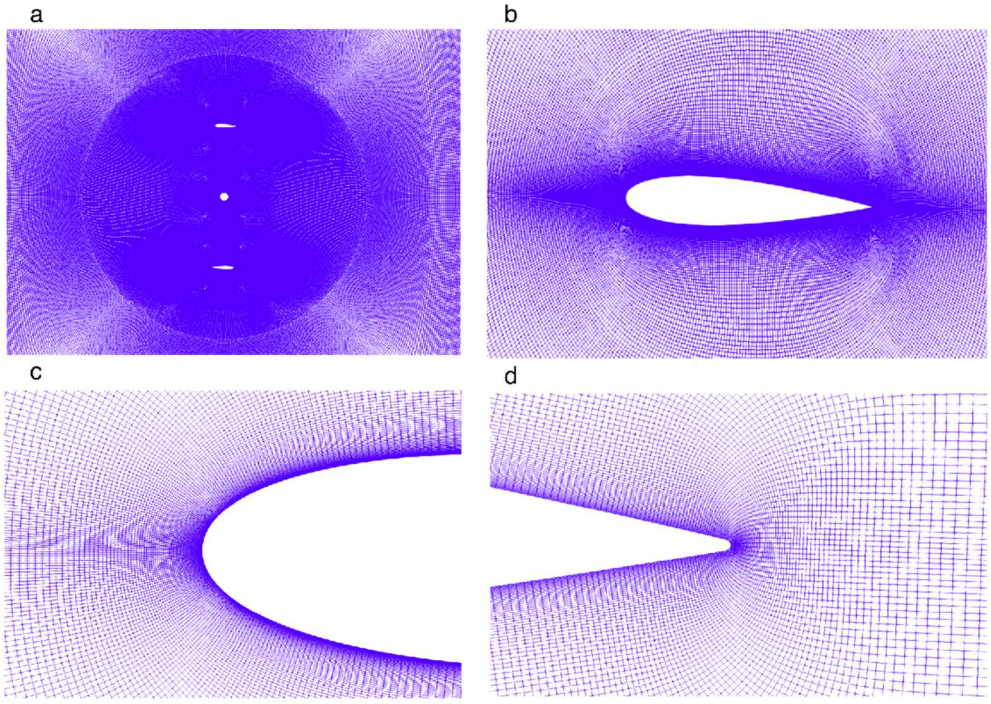

Figure 3.10: The computational grid used in the numerical simulations: detailed grid: around the rotor (a), around the airfoil (b), near the airfoil leading edge (c), near the airfoil trailing edge (d).

Table 3.6: List of the computational grids used for grid sensitivity study.

Grid	**Number of cells**	**Number of nodes on the airfoil**	**Growth ratio**
Grid 1	286312	352	1.04
Grid 2	569720	500	1.04
Grid 3	982316	706	1.04
Grid 4	1744682	1000	1.04

To confirm that the viscous sublayer within the boundary layer is entirely resolved, the maximum y^+ value on the blade surfaces using the reference grid for both cases with SST and SSTLM turbulence models is illustrated in Figure 3.12 as a function of the blade's azimuthal position. In both cases, the maximum y^+ value is found to be less than unity.

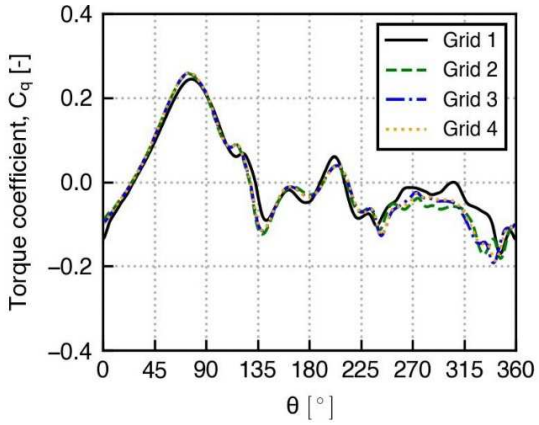

Figure 3.11: Impact of the grid refinements on blade 1 torque coefficient over the last 26th rotation cycle, using the SST model.

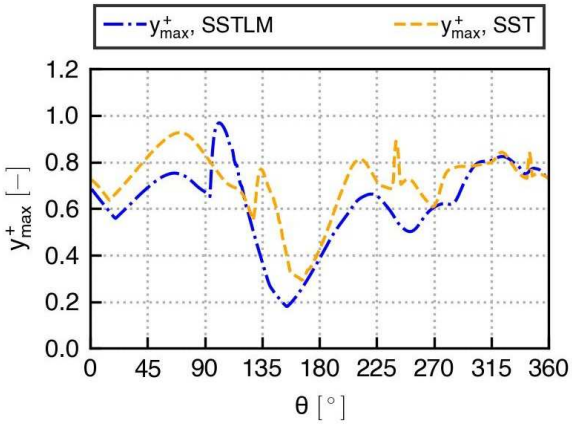

Figure 3.12: The azimuthal variation of the maximum y^+ on blade 1 surface over the last 26th rotation cycle using the SST and SSTLM models. The results are presented employing the reference grid.

3.3.6 Time step sensitivity analysis

A sensitivity analysis regarding the time step is performed to identify the optimal time step for the numerical computations. This is achieved by using four time steps: $\Delta t = 9 \times 10^{-6}$s, $\Delta t = 1 \times 10^{-5}$s, $\Delta t = 2 \times 10^{-5}$s, and $\Delta t = 3 \times 10^{-5}$s. These correspond to azimuthal increments: $\Delta\theta = 0.0351°$, $\Delta\theta = 0.039°$, $\Delta\theta = 0.078°$, and $\Delta\theta = 0.117°$, respectively. The impact of the time step (and thus the azimuthal increment) on the torque coefficient, C_q, of blade 1, during the last rotation cycle, is depicted in Figure 3.13. Given that there are negligible differences in C_q between $\Delta t = 9 \times 10^{-6}$s and $\Delta t = 1 \times 10^{-5}$s (corresponding to

$\Delta\theta = 0.0351°$ and $\Delta\theta = 0.039°$), the second time step, $\Delta t = 1 \times 10^{-5}$s, is chosen for the simulations.

Each simulation conducted on the Compute Canada clusters required approximately 45 days to 2 months to complete.

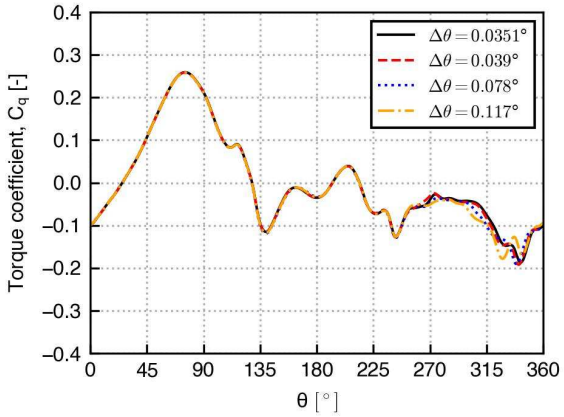

Figure 3.13: Impact of the azimuthal increments on blade 1 torque coefficient over the last 26th turbine revolution.

3.4 Numerical and experimental studies of the wake

In this section, we present another study that focuses on the analysis of the wake dynamics of a small H-type VAWT using a combination of numerical and experimental approaches. For the numerical study, we use three eddy viscosity turbulence models to assess the flow behavior around the VAWT and the effect of vortex structures on the wake. In parallel with the numerical approach, we also conducted an experimental study using Particle Image Velocimetry (PIV) to measure and visualize the wake behind the wind turbine. The combination of these two methods provides insight into understanding the characteristics of VAWT wakes.

3.4.1 Motivation

As mentioned in Chapter 1, among the motivations for the renewed research in VAWTs is the potential for more efficient land use in energy extraction. This is based on the evidence suggesting that arrays of closely-spaced VAWTs may outperform the industry-standard HAWTs in terms of energy extraction per unit of land area. Dabiri [11] reported a power density of 10 to 30 W/m^2, in contrast to the 1 to 3 W/m^2 output of HAWT farms [145]. Field

experiments conducted by Brownstein et al. [146] showed that the average rotor performance in an array was 20% higher than that of a single isolated turbine. Another study by Scherl et al. [147] further supports the findings by demonstrating a 30% increase in average rotor output in an array of two turbines compared to the performance of an isolated turbine.

Given the importance of optimal turbine spacing in VAWT farms for maximizing power density, this study employs PIV and URANS simulations to study the wake dynamics of a small H-type VAWT.

3.4.2 The VAWT prototype

Both experimental and numerical studies are based on the use of a small H-type VAWT with two blades. This VAWT is manufactured using 3D printing. The turbine consists of a rotor with a diameter of 250 mm and two straight blades. Each blade has a chord of 40 mm and a span of 250 mm. The blades are designed with a NACA0015 airfoil.

The VAWT prototype is shown in Figure 3.14, and its schematic view is illustrated in Figure 3.15.

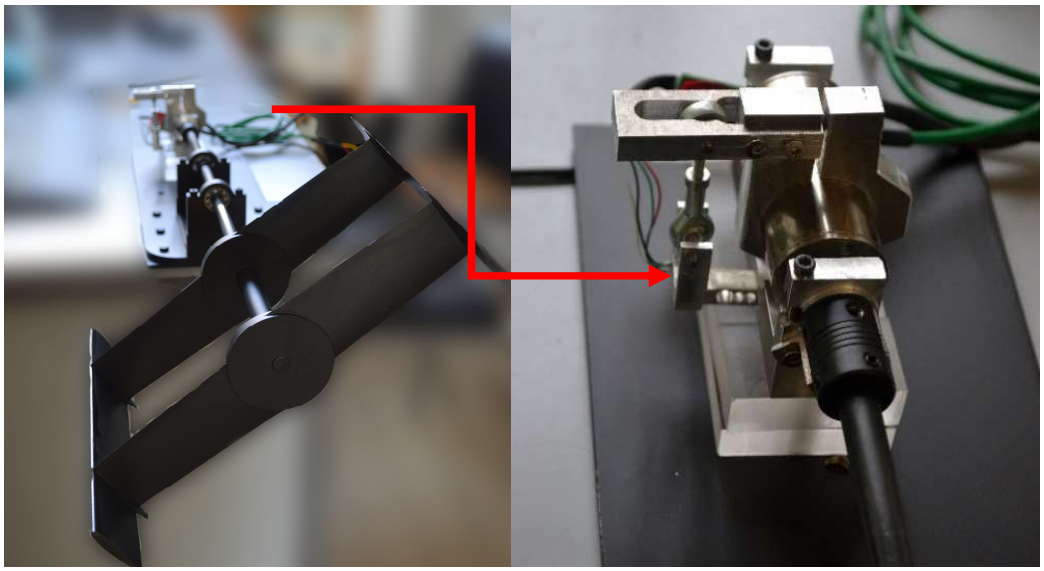

Figure 3.14: The VAWT prototype.

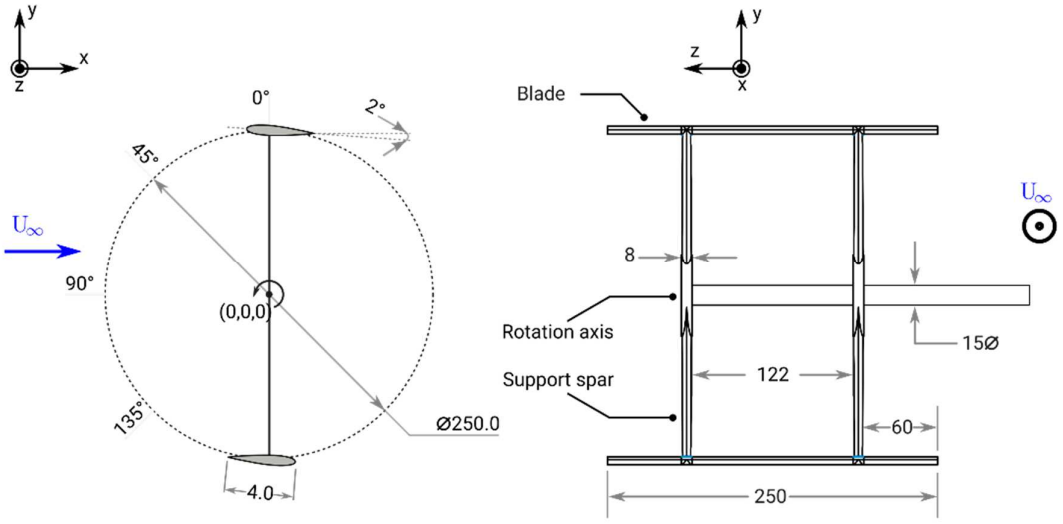

Figure 3.15: Schematic views of the VAWT prototype.

3.4.3 The wind tunnel.

The wind tunnel of the LIFSE laboratory at École Nationale Supérieure d'Arts et Métiers (ENSAM) (Figure 3.16) is designed as a closed-loop that can generate wind speeds reaching up to 40 m/s, equivalent to about 145 km/h, in its test section. The air flow in this section is of high quality, benefiting from the presence of both a settling chamber and a converging section with a high contraction ratio of 12.5, which results in notably low turbulence levels, approximately 0.5%.

The flow in the wind tunnel is initiated by an axial fan with a 3 m diameter, powered by a 120 kW motor, and regulated by a variable frequency drive. The test section, spanning between the floor and ceiling, has a rectangular shape measuring 1.65 m by 1.35 m, with a length of 1.80 m. A rotating platform of 1.21 m in diameter is included to adjust the angle of the model under test. The dimensions of the return channel are 3 m by 3 m by 6 m. Each section of the tunnel is fitted with a three-axis robotic probe system for conducting hot-wire velocity measurements [148].

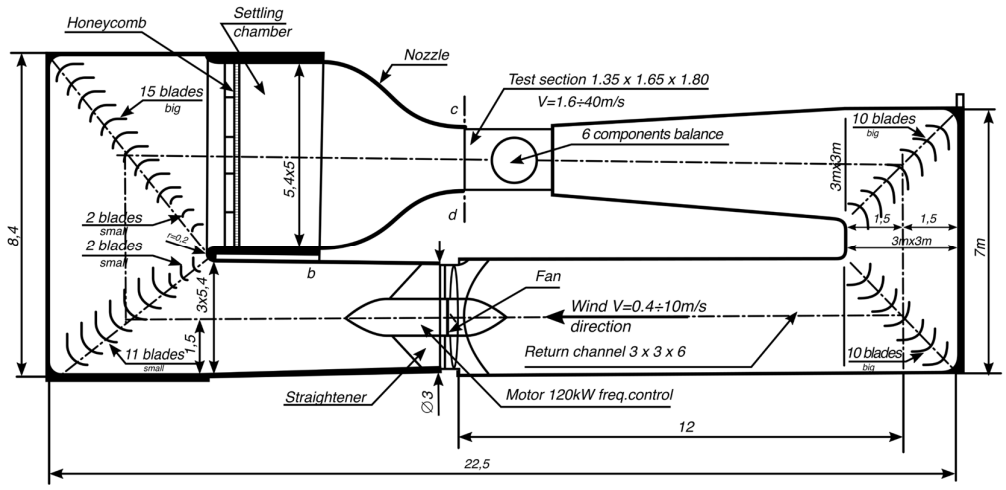

Figure 3.16: Schematic representation of the wind tunnel at the LIFSE laboratory, ENSAM. Redrawn from [148] .

3.4.4 PIV measurements

Particle Image Velocimetry (PIV) is a non-intrusive optical measurement technique used in fluid mechanics to obtain velocity measurements and related properties in fluids. The fundamental principle of PIV involves seeding the flow with tracer particles that are small enough to follow the fluid's motion. These particles are illuminated by a laser sheet, and their movement is captured by cameras at high frame rates. The process involves taking pairs of images in quick succession. The displacement of the particles between these two images, captured within a very short time interval, is measured. By knowing the time between the shots and the scale of the image, the local velocity of the flow can be calculated. This technique provides instantaneous velocity vector fields in the plane of the laser sheet. PIV is widely used for its ability to provide detailed quantitative data of flow patterns, especially in complex flows, without disturbing the flow itself [149].

In our experimental setup (shown in Figure 3.17) for investigating the wake behind a small VAWT, the PIV system was operated using Dantec Dynamics software DynamicStudio v4. Image acquisition was performed using a Nd-YAG laser (Litron Nano-L 200-15) (see Figure 3.18), with an impulse power of 200 mJ. The setup included two CCD (Charge-Coupled Device) cameras (Dantec FlowSense 4M), each with a resolution of 2048x2048 pixels, and equipped with MicroNikkor AF 60 mm f/2.8D lenses. Synchronization between the laser and

image acquisition was achieved using an NI PCI 6601 card. For visualizing the flow, micro-droplets of olive oil produced by a mist generator (Dantec 10F03), were used as seeding particles. These droplets had an average diameter of 2-5 μm. The exploratory field behind the VAWT was segmented into eight windows, as shown in Figure 3.19, each measuring approximately 250 mm x 250 mm. Additionally, the inlet velocity in the wind tunnel was set to 4.71 m/s, and the VAWT was rotating at 900 rpm, yielding a TSR of 2.5.

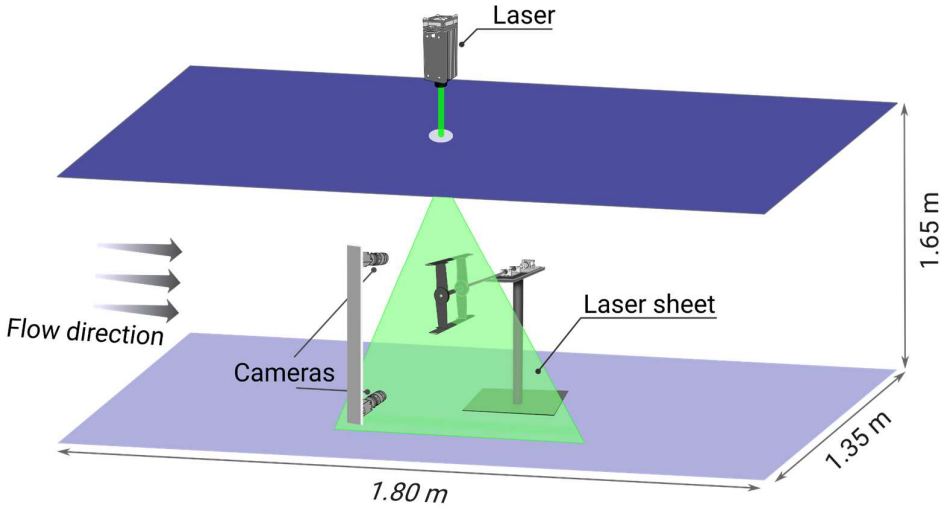

Figure 3.17: Schematic diagram of the experimental setup.

Figure 3.18: The wind turbine under the laser sheet.

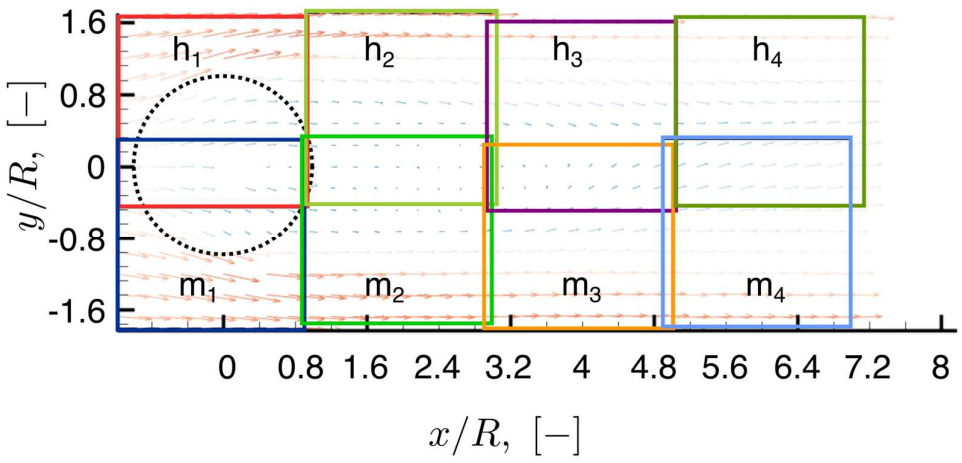

Figure 3.19: Interrogation windows in the midplane of the VAWT. The dotted circle is the trajectory of the blades.

3.4.5 Numerical simulations

For the numerical studies of the VAWT wake dynamics, we conduct 2D simulations with the computational domain illustrated in Figure 3.20 at the VAWT's mid-plane, with the operational conditions detailed in Table 3.7. This investigation makes use of three turbulence models: the k-ω SST (SST), γ-Re_θ (SSTLM), and Spalart-Allmaras (SA) models (Table 3.8). The numerical methods applied in this study are analogous to those described in Section 3.3.4.3, and for the sake of brevity, they are not reiterated here.

Table 3.7: Geometrical characteristics and operational conditions of the simulations.

Parameter	Value
Airfoil	NACA0015
Number of blades, N [-]	2
Aspect ratio, h/d [-]	1
Shaft diameter [m]	0.015
Chord, c [m]	0.04
Diameter, d [m]	0.25
Solidity, σ [-]	0.32
Tip speed ratio, λ [-]	2.5
Rotational speed, Ω [rpm]	900
Freestream velocity, U_∞ [m/s]	4.71
Freestream turbulence intensity, TI [%]	0.5

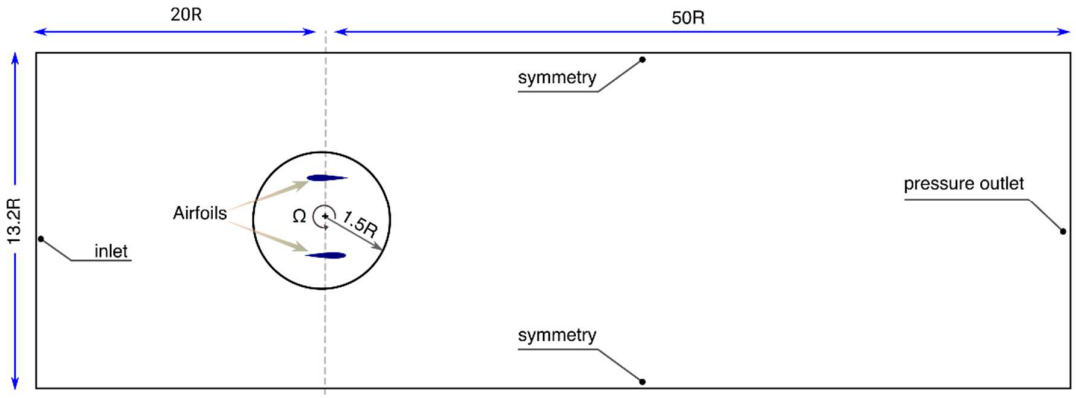

Figure 3.20: The computational domain of the CFD simulations for the wake study.

Table 3.8: The URANS turbulence models used for the present analysis.

Turbulence model	**Abbreviation**	**Transition modeling**
k-ω SST	SST	No
γ-Re_θ k-ω SST	SSTLM	Yes
Spalart-Allmaras	SA	No

Chapter 4

Results and Discussion

4.1 Introduction

In this section, we present and discuss the findings of the studies described in the previous chapter. The first study evaluates the eddy viscosity turbulence models for the prediction of the unsteady separated flows around an oscillating airfoil that induces deep dynamic stall. The second examines methods for estimating the angle of attack and relative velocity of VAWT blades from CFD simulations. This analysis provides insights into blade performances under dynamic stall and blade-vortex interactions. The third study combines CFD computations with experimental data to investigate the wake dynamics of a VAWT.

4.2 Evaluating RANS models for deep dynamic stall prediction

4.2.1 Static cases

Figure 4.1 presents the results of the 2D steady-state RANS simulations, which employed the $k-\omega$ SST turbulence model to determine the static stall angle, α_{ss}, of the NACA0015 airfoil. The aerodynamic coefficients against the AoA, α.

The numerical results are validated against the quasi-steady experimental measurements of Piziali [94]. It is worth mentioning again that these quasi-steady measurements were performed at a low frequency, specifically $\Omega \leq 0.04$ Hz, leading to the classification of the observed stall as a static stall.

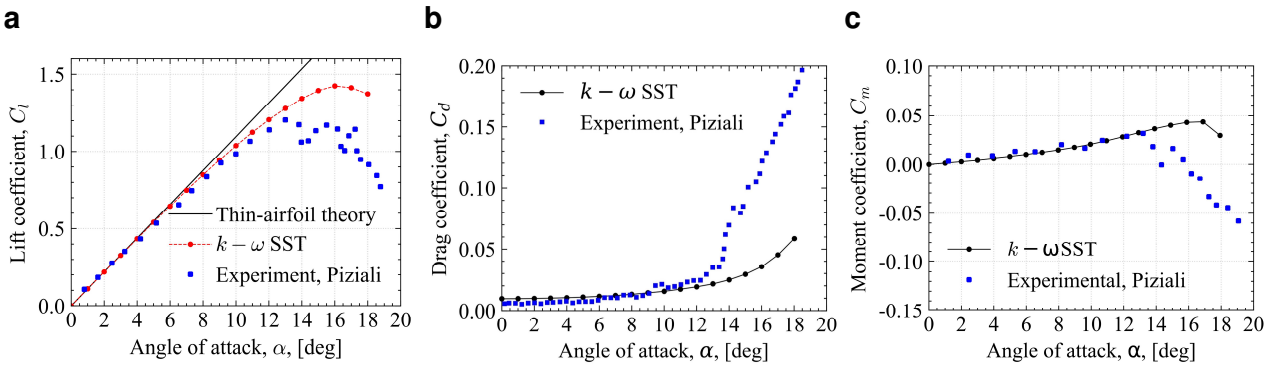

Figure 4.1: Variations of the aerodynamic coefficients with AoA for a NACA0015 airfoil using $k-\omega$ SST model at $Re_c = 1.95 \times 10^6$: (a): lift coefficient, (b): drag coefficient, and (c): pitching moment coefficient, compared against the experimental data of Piziali [94].

In Figures 4.1a to 4.1c, only the upstroke phase of the experimental data is plotted. At lower AoAs, specifically when $\alpha \leq 8°$, the lift coefficient, C_l, aligns closely with the experimental values. The behavior of both curves is linear with a slope, $dC_l/d\alpha \approx \pi^2/90$ aligning with predictions from thin airfoil theory. Yet, at higher AoAs, the k-ω SST model begins to overpredict C_l as the AoA increases. The divergence of the C_l curve from the linear behavior can be attributed to the thickening of the boundary layer on the suction side of the airfoil, which is a consequence of adverse pressure gradients [20]. The discrepancy between the two curves is markedly apparent when $\alpha > 13°$. Specifically, the experimental data indicate that the onset of static stall occurs at $\alpha \approx 13°$, ($C_{l,max} \approx 1.2$), while the model predicts a higher static stall at roughly $\alpha \approx 16°$ ($C_{l,max} \approx 1.42$). This inconsistency could be attributed to the delayed prediction of the turbulent boundary layer separation on the suction side of the airfoil in the presence of adverse pressure gradients [150]. Wang and Xiao [150] also reported this tendency of the k-ω SST model to overestimate the lift coefficient and underestimate the drag coefficient near static stall conditions, with a tripped boundary layer on the airfoil's leading edge.

The variation in the drag coefficient with the AoA is presented in Figure 4.1b. Between $0° \leq \alpha \leq 9°$, the computed drag coefficient is slightly higher than the experimental values, although the two curves are somewhat congruent. This overestimation of the drag is likely because the measured forces did not include the contribution of viscous wall shear stress, as the forces were integrated from pressure data only. For larger AoAs, $\alpha > 9°$, C_d values are underestimated, and the difference becoming more pronounced beyond the static stall angle ($\alpha \approx 13°$).

The pitching moment, C_m, about the quarter-chord axis shown in Figure 4.1c matches reasonably well with experimental values for AoAs below static stall angle ($\alpha_{ss} \approx 13°$). However, beyond stall angle, the model overpredicts C_m values, resulting in a delayed stall prediction. Notably, the k-ω SST model predicts a consistently positive pitching moment coefficient across the AoA range, suggesting the center of pressure is located forward of the quarter chord position.

4.2.2 Dynamic stall cases

4.2.2.1 Aerodynamic coefficients

This section discusses the aerodynamic coefficients computed from the URANS simulations of the flow around the airfoil undergoing sinusoidal oscillation about its quarter-chord axis, employing the three turbulence models: k-ω SST, Spalart-Allmaras, and LS k-ϵ. It also compares these results with the experimental dataset from Piziali [94]. Following the terminology of McCroskey [151], the analysis categorizes dynamic stall into four distinct types:

- *No-stall*: In this regime, the AoA does not exceed the static stall angle, α_{ss}. A linear response is observed in the aerodynamic loads with slight hysteresis but with no negative nose-down pitching moment.
- *Stall onset*: In this regime, the AoA reaches the static stall angle. Under these conditions, the maximum useful lift is produced without excessive drag or pitching moment.
- *Light stall*: Or moderate stall, in which a mild hysteresis in aerodynamic loads is observed with a less severe increase in drag and generation of negative nose-down pitching moment.
- *Deep stall*: In this regime, severe hysteresis loops with significant peaks are observed in the aerodynamic loads. A pitching moment coefficient of as much as 0.15 or beyond constitutes a deep stall case.

The hysteresis loops for the dynamic lift coefficient predicted by the three turbulence models are illustrated in Figures 4.2a to 4.2c. For clarity, the aerodynamic coefficients from each model are plotted separately with the experimental values. It can be observed that the k-ω SST model (Figure 4.2a) predicts a higher lift coefficient during the upstroke phase, although its trend is consistent with the experimental data for AoAs up to $\alpha \approx 19.60° \uparrow$. Nonetheless, the stall angle lags behind the measured value by roughly 1°, with a maximum lift coefficient $C_{l,\max} = 1.72$ (at around $\alpha \approx 20.4° \uparrow$) that is 2.8% lower than the experimental maximum of about 1.77. Conversely, the SA model (Figure 4.2b) predicts lower C_l values as the AoA increases, with a maximum predicted $C_{l,\max} = 1.486$, which is 16%below the experimental peak. The LS k-ϵ model (Figure 4.2c) predicts a maximum $C_{l,max}$ (at $\alpha \approx 20.75° \uparrow$) very close to the experimental value, but it tends to overestimate the C_l curve considerably higher than the k-ω SST model during the upstroke phase. During the downstroke phase, the computed C_l

curve with k-ω SST shows a significant drop just pass stall ($\alpha \approx 22°$). It shows an oscillatory behavior with the lowest value, $C_{l,min} \approx 0.36$ (at $\alpha \approx 21.45° \downarrow$).

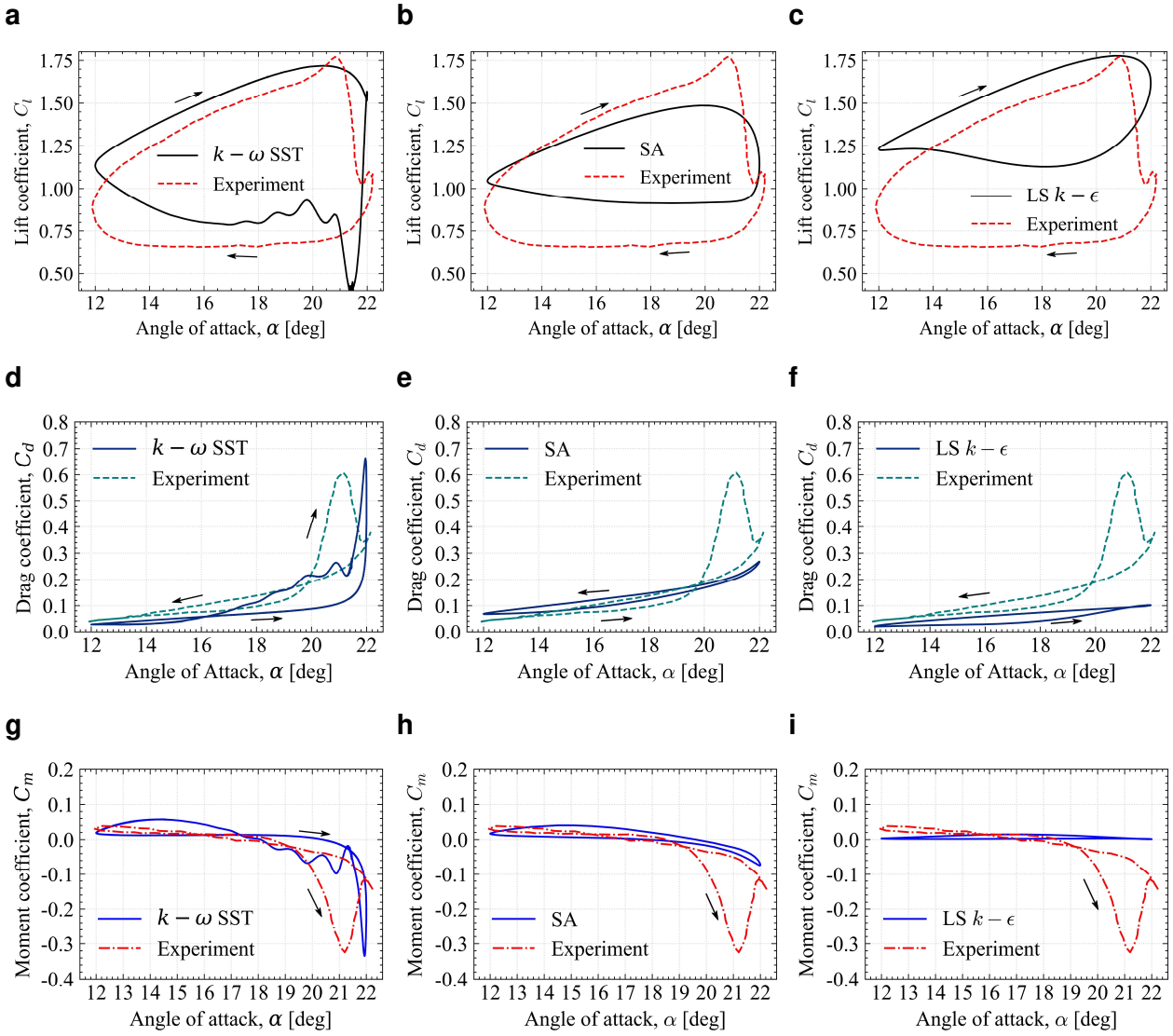

Figure 4.2: Lift, drag, and pitching moment coefficients of the NACA0015 airfoil plotted against the AoA at $Re_c = 1.95 \times 10^6$, employing three turbulence models: k-ω SST , SA, and LS k-ϵ . (a-c): Lift coefficient (d-f): Drag coefficient. (g-i): Pitching moment coefficient. The experimental data of Piziali [94] are used for comparison.

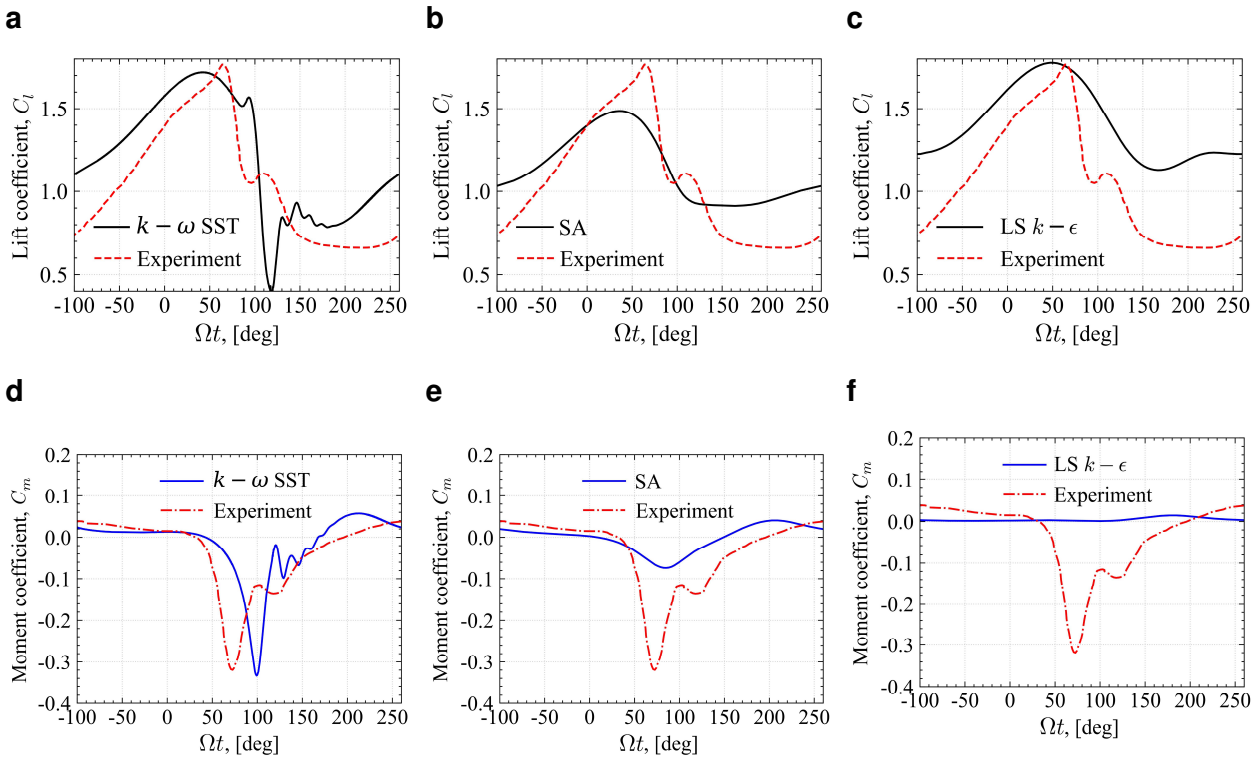

Figure 4.3: Variation of lift and pitching moment coefficients with the phase angle: (a-c): Lift coefficient computed using k-ω SST, SA, and LS k-ε models and (d-f): pitching moment coefficient computed using k-ω SST, SA, and LS k-ε models, respectively. The experimental dataset of Piziali [94] is used for comparison.

The oscillatory behavior of the lift coefficient curve during the downstroke motion has also been reported in the numerical simulations of dynamic stall by Geng et al. [85], Wang et al. [125], and Tseng and Cheng [152]. This oscillation could be linked to the intricate flow features in the post-stall phase characterized by vortex shedding, as demonstrated below by the contours of vorticity in Figure 4.4. The C_l curve exhibits a rapid increase for AoAs below the static stall, $\alpha_{ss} \approx 16°$ (computed by the static simulations), thereby recovering its linear behavior. In contrast, the SA model predicts considerably higher C_l values during the downstroke phase , with $C_{l,\min} \approx 0.91$ at $\alpha \approx 18.48°$, and the C_l curve remains relatively constant for a significant portion of the downstroke phase of motion, with AoAs down to $\alpha \approx 16°$. The LS k-ε model also considerably overestimates the C_l curve during the downstroke, surpassing the predictions of the SA model. It only drops to a $C_{l,\min}$ of 1.12 (at $\alpha \approx 18.11° \downarrow$), which is 39% above the experimental value ($C_{l,min} \approx 0.65$, at $\alpha \approx 15.67° \downarrow$). It is also noteworthy that the SA and the LS k-ε models predicted narrow and smooth lift coefficient

loops, lacking the abruptness seen in the C_l hysteresis loop predicted by the k-ω SST model. This pattern is similarly observed in the coefficients of drag and pitching moment.

Figures 4.2d to 4.2f show the drag coefficients, C_d, computed using the three turbulence models. The k-ω SST model predicts C_d that closely matches experimental results for AoAs under the static stall angle of approximately 16° but underestimates it at higher AoAs. Near stall, the predicted drag peak ($C_{d,\max} \approx 0.66$ at $\alpha \approx 21.95°$), whereas the experimental peak is $C_{d,\max} \approx 0.6$, at $\alpha \approx 21.15° \uparrow$, with a slight delay of 0.8°. The SA model's drag coefficient, shown in Figure 4.2e, aligns with experimental data up to an AoA of 20° during the upstroke, though it does not accurately capture the maximum C_d. Interestingly, the C_d curves for the upstroke and downstroke phases almost coincide. The LS k-ε model, presented in Figure 4.2f, also mirrors this trend but with lower drag values. The pitching moment coefficients, C_m, depicted in Figures 4.2g and 4.2i using all three models, show that for AoAs below 16° during the upstroke, the k-ω SST model (Figure 4.2g) provides a close match to the experimental C_m, with a computed peak around -0.33, nearly identical to the measured value of -0.32. Conversely, the LS k-ε model significantly diverges in capturing the experimental C_m loop, showing positive values throughout the upstroke phase ($C_{m,\min} = 0.001$, at $\alpha \approx 21.91° \uparrow$). The SA model offers an improvement over LS k-ε, yet it fails to accurately predict the steep drop in the nose-down pitching moment, with the lowest C_m being only -0.07 (at $\alpha \approx 21.97° \uparrow$).

The results indicate that results of LS k-ε and SA models lack deep dynamic stall features that are characterized by abrupt transition near the stall angle in the aerodynamic forces and pitching moment, suggesting only a "stall onset" for the former model and a "moderate stall" for the latter model, with the maximum magnitude of nose-down pitching moment not exceeding 0.15 [153]. The coefficients of lift and pitching moment plotted against the phase angle, Ωt, (Figures 4.3a to 4.3f) reveal distinct behaviors. For the k-ω SST model, the pitching moment coefficient (Figure 4.3d) shows a sharp drop between $50° < \Omega t < 100°$, while the lift coefficient drops between $100° < \Omega t < 150°$. This indicates a movement in the center of pressure on the suction side of the airfoil, leading to moment-stall before lift-stall. The SA model shows a smooth decrease in the pitching moment (Figure 4.3e) between $20° < \Omega t < 80°$ and in lift between $40° < \Omega t < 110°$, suggesting an earlier center of pressure shift but with a milder impact than in the k-ω SST case. The LS k-ε model predicts a C_m (Figure 4.3f) that is nearly constant for all phase angles, while the lift coefficient exhibits a smooth decrease between $50° < \Omega t < 110°$. This pattern suggests that the flow separation on the

suction side is not pronounced enough to significantly shift the center of pressure, likely due to the model's excessive diffusivity and inability to accurately predict the adverse pressure gradients in the turbulent boundary layer near the trailing edge.

4.2.2.2 Dynamic stall process

The unsteady flow characteristics predicted by the URANS computations are visualized in Figure 4.4 through contours of the spanwise (i.e., z-direction) vorticity component field. These contours are shown at several representative AoAs during the entire cycle of oscillation, highlighting the main flow features related to the dynamic stall phenomenon exhibited by the oscillating NACA0015 airfoil.

4.2.2.3 The $k-\omega$ SST model

The spanwise vorticity contours computed using the k-ω SST model, shown in Figure 4.4a, reveal the flow characteristics during the upstroke stage of the motion. Initially, $12° \leq \alpha \leq 16.5°$, the flow remains attached on the suction side of the airfoil. As the AoA continues to increase, the turbulent boundary layer separation gradually spreads from the trailing edge toward the leading edge, eventually covering the entire suction surface of the airfoil. The separated shear layer rolls up and forms a dynamic stall vortex (DSV), accompanied by the development of a counter-clockwise secondary vortex near the trailing edge. The DSV attains its maximum size and intensity at $\alpha \approx 22°$. During its residence over the airfoil, the DSV induces an additional lift force, as observed in Figure 4.3a. The shedding of the primary trailing-edge vortex (TEV) into the wake causes a drop in the lift curve and a significant overshoot in the nose-down pitching moment coefficient.

In the downstroke phase, the flow remains fully separated on the airfoil's upper surface, characterized by vortex shedding. This vortex shedding causes oscillations in the aerodynamic forces (Figures 4.2a and 4.2d) and the pitching moment coefficient (Figure 4.2g). The flow on the suction surface appears more complex, particularly near the leading edge, where a pair of counter-rotating vortices emerges around $\alpha \approx 21.4° \downarrow$. As the airfoil continues pitching down, the boundary layer begins to reattach from the leading edge toward the trailing edge. However, this gradual reattachment process is slow, as observed at $\alpha \approx 14.32° \downarrow$, where the turbulent boundary layer has not yet been fully reattached.

The sequence of stall events predicted by the k-ω SST model indicates that the NACA0015 airfoil exhibits a trailing-edge stall rather than a leading-edge stall, consistent with the findings of Rhee [126,153]. This type of stall is typically linked with relatively thick airfoil sections, while thin airfoils are prone to leading-edge dynamic stall, often triggered by the bursting of a laminar separation bubble near the leading edge [127].

4.2.2.4 The Spalart-Allmaras Model

The spanwise vorticity contours obtained from the SA model are depicted in Figure 4.4b. During the upstroke motion, the flow remains attached to the airfoil's suction surface up to AoAs below approximately 18.75°. As the AoA increases beyond this value, flow separation initiates from the trailing edge and progresses upstream (see $\alpha \approx 19.49° \uparrow$), accompanied by the emergence of a secondary counter-clockwise vortex at the trailing edge ($\alpha \approx 21.96° \uparrow$). The flow separation reaches its maximum extent at around 22° before the airfoil begins the downstroke motion. However, in contrast to the k-ω SST model predictions, the separation does not extend to the leading edge.

Furthermore, the Spalart-Allmaras model fails to predict the detachment of the primary vortex within the separated flow region on the airfoil's suction surface. Note that the slope of the lift curve computed by the SA model (Figure 4.2b) is lower than that predicted by the k-ω SST model (Figure 4.2a). Conversely, the drag coefficient is higher, which can be attributed to the slightly earlier flow separation observed in the SA predictions compared to the k-ω SST model (see $\alpha \approx 18.75° \uparrow$). As the airfoil continues to pitch down, the flow reattaches smoothly without inducing severe vortical structures, in contrast to the post-stall phase predicted by the k-ω SST model (for comparison, see, $\alpha \approx 18.24° \downarrow$ and $\alpha \approx 16.50° \downarrow$). This behavior results in a smooth variation of the aerodynamic coefficients, as seen in Figures 4.2b, 4.2e, and 4.2h.

4.2.2.5 The LS $k - \varepsilon$ model

Figure 4.4c depicts the spanwise vorticity contours of the flow computed using the LS k-ε model. Unlike the k-ω SST and the SA models, this model predicts a boundary layer that exhibits a less pronounced separation on the suction side of the airfoil throughout much of the upstroke phase of the oscillation, specifically for $\alpha > 18.75°$. At the peak AoA of the cycle, $\alpha = 22°$, the separation region at the trailing edge extends over approximately half of the airfoil chord.

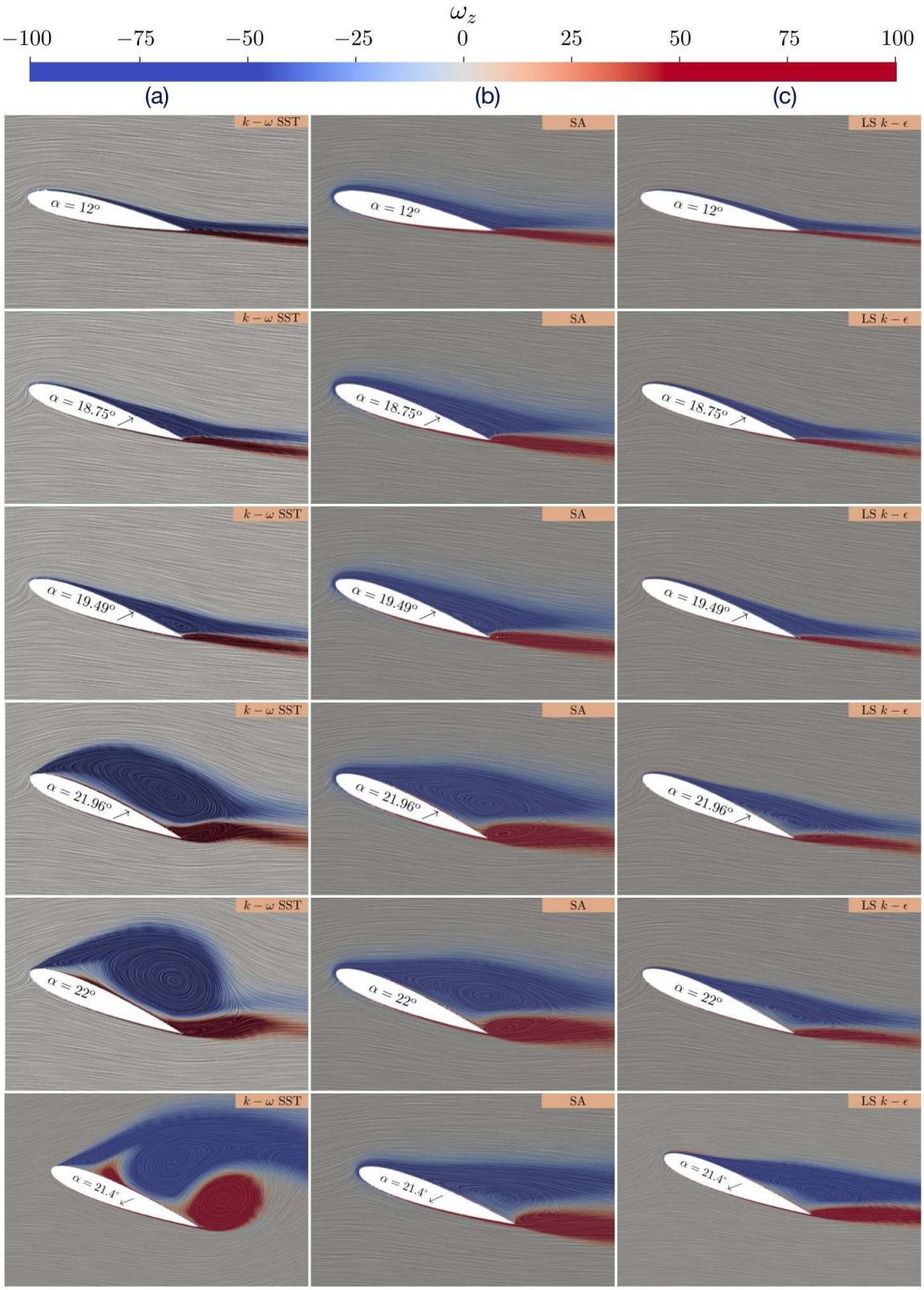
ω_z
−100
−75
−50
−25
0
25
50
75
100
(a)
(b)
(c)
$k-\omega$ SST
SA
LS $k-\epsilon$
$\alpha = 12^o$
$\alpha = 18.75^o$
$\alpha = 19.49^o$
$\alpha = 21.96^o$
$\alpha = 22^o$
$\alpha = 21.4^*$

Cont.

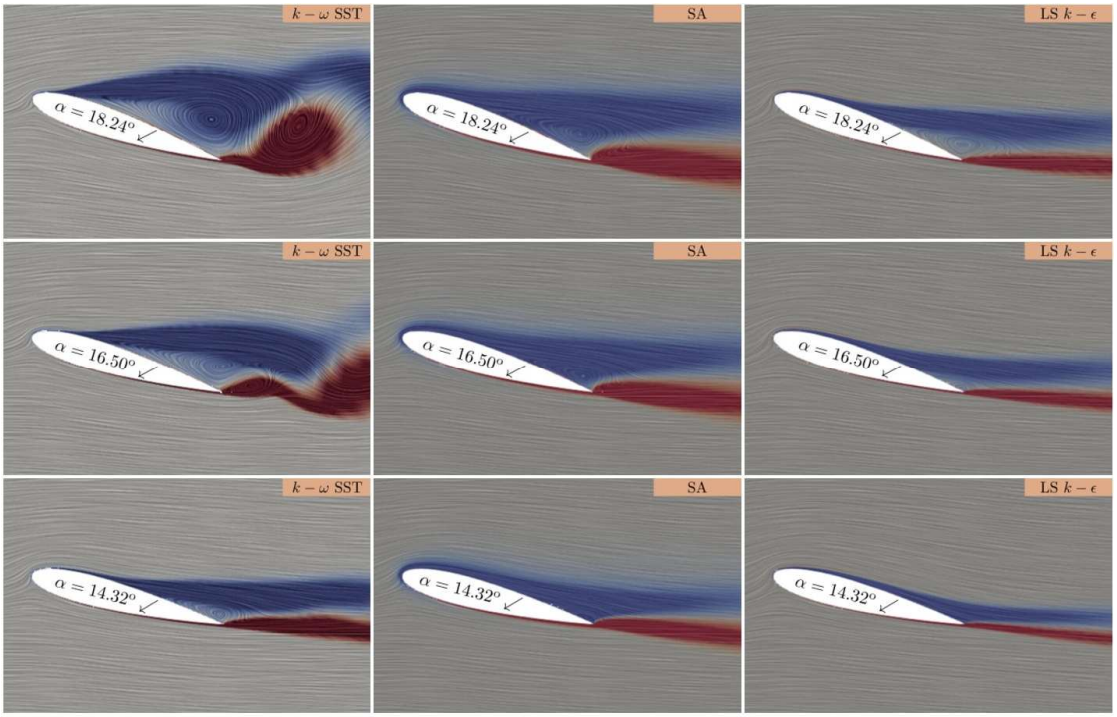

Figure 4.4: Vorticity contours for the oscillating airfoil, $\alpha(t) = 17 + 5\ \sin(\Omega t)$ with $\kappa = 0.1$, about $x/c = 25\%$ axis, at $Re_c = 1.95 \times 10^6$, using three turbulence models: (a) k-ω SST, (b) Spalart Allmaras (SA), and (c) LS k-ϵ.

Subsequently, during the downstroke phase, the reattachment of the boundary layer occurs more rapidly than predicted by the SA model, observable in the AoA range from $\alpha = 22°$ to $\alpha \approx 14.32° \downarrow$. This mild separation of the boundary layer contributes to maintaining a relatively high lift coefficient throughout the downstroke phase while the drag remains low. Moreover, the pitching moment coefficient shows minimal variations, suggesting a slight impact on the center of pressure movement.

4.2.3 Influence of the pitching axis location

In this section, we discuss the impact of translating the oscillation axis downstream to the mid-chord location ($x/c = 50\%$). The k-ω SST model is used in the simulation due to its relatively accurate predictions of the unsteady flow compared to the other two models. The study includes a comparison of the lift coefficient and the pitching moment coefficient. The results are plotted against the phase angle, Ωt, as illustrated in Figures 4.5a and 4.5b. The results from the previous study at the quarter-chord position ($x/c = 25\%$) are also presented for comparison.

Figure 4.5a indicates that translating the oscillation axis to the mid-chord position results in a decreased lift during the upstroke phase compared to the quarter-chord axis location. This effect is likely due to the reduction in the effective AoA and the relative velocity at the leading edge and trailing edge of the airfoil [154]. The pitching moment coefficient before the stall shows little difference between the two axis locations, as depicted in Figure 4.5b.

During the downstroke phase, the airfoil oscillating around the mid-chord axis exhibits more substantial variations in lift. Furthermore, the airfoil oscillating at $x/c = 50\%$ experiences a marked increase in the nose-down pitching moment, $C_m \approx -0.5$. Comparative flow development around the airfoil for both axes, focusing on the spanwise vorticity component, is provided in Figure 4.6. Throughout the upstroke phase, $12° \leq \alpha \leq 22° \uparrow$, the flow patterns remain similar for both positions. Nevertheless, the onset of flow separation near the trailing edge is slightly delayed in the airfoil oscillating about its mid-chord axis, as observed at $\alpha = 18.75° \uparrow$ and $\alpha = 19.49° \uparrow$.

This is also observable at $\alpha = 22°$ regarding the development of the DSV. Even though the DSV forms later as the airfoil pitches downward, the principal flow patterns characteristic of the post-stall phase, such as vortical formations on the suction side of the airfoil and their shedding into the wake, remain qualitatively similar.

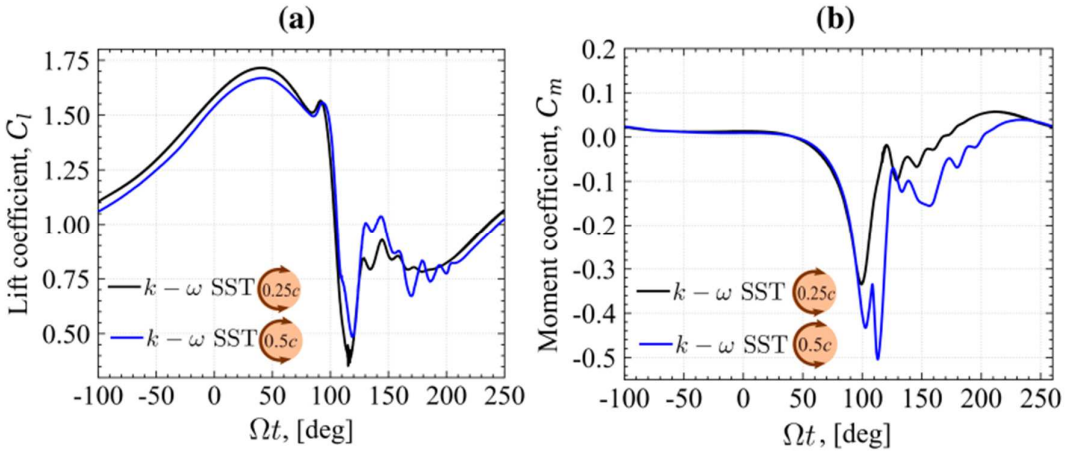

Figure 4.5: Comparison between the lift coefficient and the pitching moment coefficient of the oscillating airfoils at $x/c = 25\%$, and $x/c = 50\%$ (a) Lift coefficients. (b) pitching moment coefficients. The moment coefficients are calculated at the quarter-chord location.

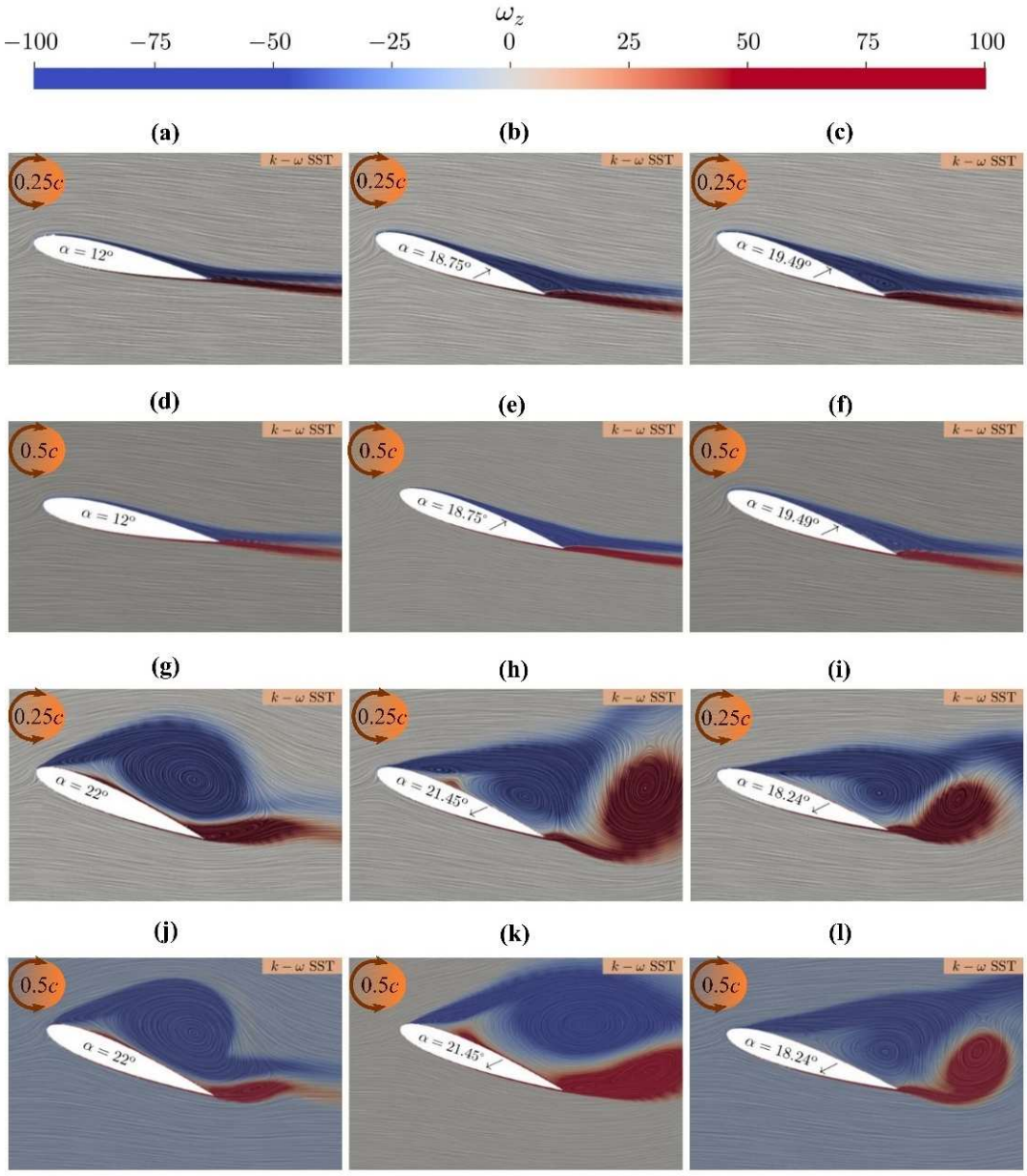

Figure 4.6: Vorticity contours of NACA 0015 airfoil oscillating about $x/c = 25\%$ and $x/c = 50\%$ axes at $Re_c = 1.95 \times 10^6$, $\kappa = 0.1$ using the k-ω SST model. (a)-(l): Comparison at angles: 12°, 18.75° ↗, 19.49° ↗, 22°, 21,45° ↙, and 18.24° ↙.

4.3 Estimating VAWT Blade AoA and relative velocity from CFD Data

This section presents the results of the numerical computations conducted in the second study for the estimation of VAWT blade AoA and relative velocity.

4.3.1 Validation of the CFD simulations

To evaluate the accuracy of CFD simulations, the flow near the blade is compared with the PIV data from Ferreira et al. [21]. This comparison highlights the dynamic stall process by tracking the evolution of the leading-edge and trailing-edge vortices. In the work of Ferreira et al. [21], the experimental setup is comparable to the present study, with similar geometric characteristics and operating conditions (a turbine with two NACA0015 profiled blades, $\kappa = 0.24$, and $Re_c = 50000$). For a straightforward comparison, the spanwise vorticity fields computed with CFD are mapped to the coordinate system used by Ferreira et al. where the VAWT blades rotate clockwise.

Figure 4.7 presents the development of the leading-edge vortex (LEV) at the azimuthal angles of $\theta = 72°$, $\theta = 90°$, $\theta = 108°$, $\theta = 133°$, $\theta = 158°$, and $\theta = 233°$. Similarly, Figure 4.8 shows the trailing-edge vortex at azimuthal angles of $\theta = 121°$, $\theta = 158°$, and $\theta = 218°$.

Both the SST and SSTLM models are capable of capturing the main aspects of the dynamic stall, including the formation, growth, and detachment of the DSV as it moves over the suction side of the blade facing the turbine shaft. Nevertheless, the following observations are worth noting:

- The SST model tends to predict a delayed onset of the stall, which can be attributed to the underlying assumption of the fully turbulent boundary layer on the airfoil. It is well established that a fully turbulent boundary layer is generally more resistant to flow separation.
- At azimuthal angles of $\theta = 133°$ and $\theta = 158°$, the SSTLM model predicts the coalescence of the DSV with a secondary vortex (DSV-SV), which is consistent with the CFD studies by Jain and Saha [155] on a VAWT blade using NACA0018 airfoil. This could be linked to the complex events occurring in the boundary layer involving the transition from laminar to turbulent flow.

Moreover, both models successfully predict the appearance of the trailing vortex, aligning with the experimental observations.

4.3.2 Angle of attack

Figure 4.9a displays a comparison between the geometric AoA, α_g, calculated using Eq. (1.1) and the AoA from CFD results with the SST turbulence model, utilizing the two approaches: method 1 [139] and method 2 [140]. The AoAs are plotted against the azimuthal angle, θ, of

blade 1 during the last 26th turbine rotation cycle. Employing method 1 reveals a notable discrepancy between the geometric AoA, α_g, and the estimated AoA throughout the entire rotation cycle. Conversely, the AoA computed using method 2 aligns closely with the geometric one, especially in the windward quartile of the azimuthal angle range ($315° \leq \theta < 45°$).

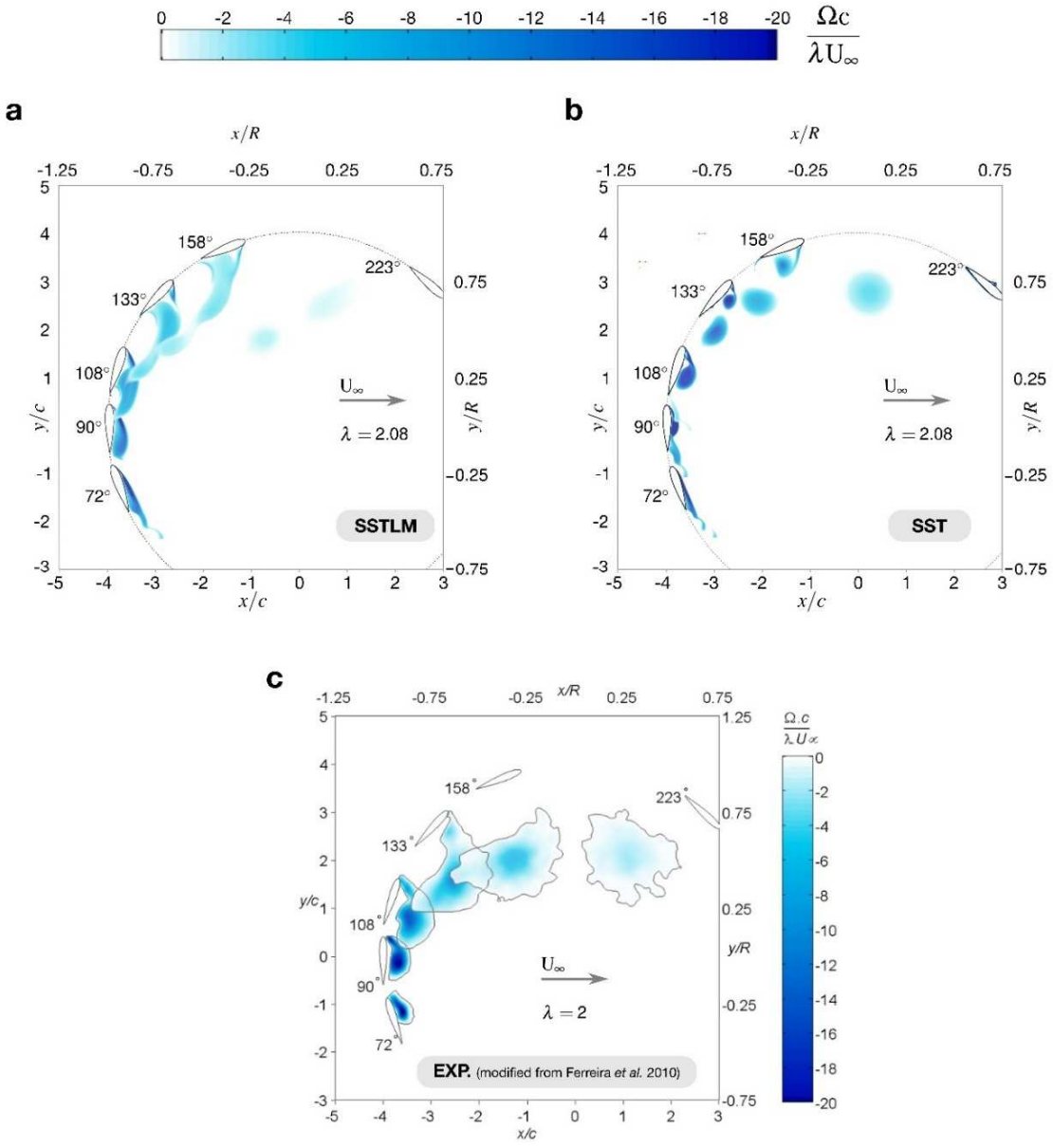

Figure 4.7: Comparison of the evolution of the leading-edge vortex (LEV) between SSTLM and SST model with the PIV data of Ferreira et al. [21], for λ≈2 at several azimuthal angles of blade 1.

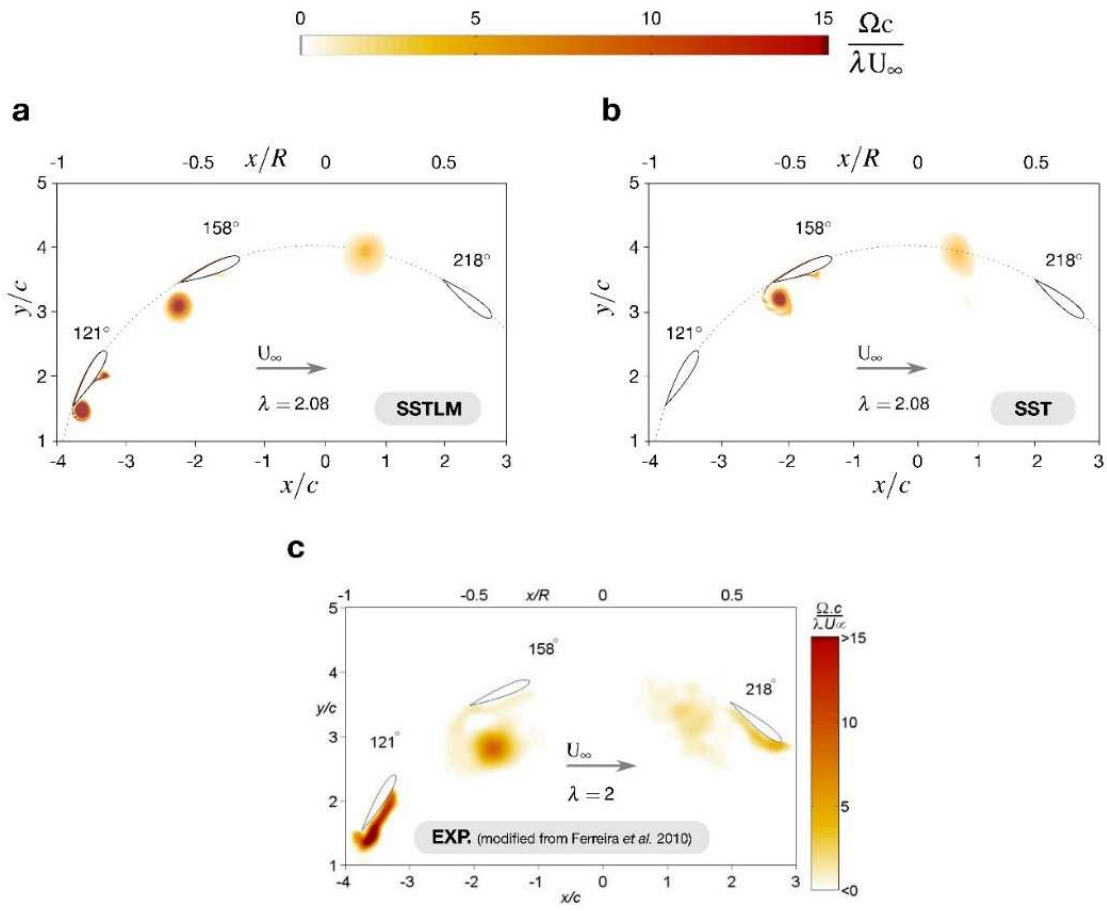

Figure 4.8: Comparison of the trailing-edge separated vortex (TEV) evolution between SST & SSTLM results and the PIV data, for λ≈2 at several azimuthal locations of blade 1. The results of the present study are transformed to match the coordinates system of the experimental data by Ferreira et al. [21].

Furthermore, in the upwind quartile ($45° \leq \theta < 135°$), the deviation becomes more pronounced as θ increases. This behavior is attributed to the streamtube expansion [156], which results in a decrease in the incoming flow velocity. Consequently, this increases the effective TSR, λ, leading to a decrease in the AoA (refer to Figure 1.6 for the impact of λ on the AoA amplitude). The peak values of both geometric and estimated AoA significantly surpass the static stall angle of the NACA0018 airfoil, $\alpha_{ss} = 10°$ (discussed below), reaching approximately 26.73° at $\theta = 119°$, and 23° at $\theta = 115°$ respectively.

In a similar manner, Figure 4.9b illustrates the results obtained using the SSTLM model. The estimated AoA closely mirrors the SST case but varies in peak values and their corresponding azimuthal positions, with the highest predicted AoA being around 24° at $\theta = 118°$.

Within the leeward quartile ($180° \leq \theta < 225°$), specifically in the second half, the estimated AoA using method 2 exhibits a notable drop in magnitude for both SST and SSTLM cases. The reduction is likely caused by the interaction between the blade and the vortices shed by the blade on the upwind side of the rotation. In the downwind quadrant ($225° \leq \theta < 315°$), ripples in AoA are apparent due to the complex flow encountered by the blade, characterized by the interaction with the wake of the upstream blade and the wake produced by the turbine shaft [140,157]. The turbine considered in this study has a shaft diameter to the turbine diameter ratio, δ, of 6% with 0.5% freestream turbulence, the change in AoA magnitude is consistent with the findings of Rezaeiha et al. [158], who showed increased blade-wake interaction for large δ (> 4%) and low inlet turbulence intensity in the downstream half of the rotation cycle. Method 2 predicts maximum AoAs (in magnitude) of 25.57° (at $\theta = 207°$) and 28.65° (at $\theta = 212°$) for SSTLM and SST cases, respectively, compared to 30.73° for α_g at $\theta = 241°$. On the other hand, Method 1 predicts much higher AoA values at much earlier azimuthal angles, likely because its sampling point is over two chord lengths from the blade, not accounting or the high solidity characteristic of the present VAWT.

Edwards [156] performed CFD simulations employing the SST turbulence model under similar conditions, considering a VAWT with NACA0018 airfoils at $\lambda = 2$ and an average $Re_c = 37000$. The same author suggested a method to estimate the AoA, with the results plotted in Figure 4.10. Comparing Figure 4.10 with Figure 4.9 (using method 2) indicates a consistent pattern on both upwind and downwind sides of the rotation. On the upwind side, the AoA in both figures is lower in magnitude than the geometric AoA. A similar observation is made on the downwind half, where the estimated AoA is also less than the geometric AoA.

Nevertheless, the reduction in AoA within Figure 4.10 is more moderate compared to method 2 in Figure 4.9. This can be explained by the inherent limitations in the approach used by Edwards that involves a cut-out of the annular region surrounding the blade, defined between $R - 2c$ and $R + 2$, with the velocity field being interpolated for this excluded zone. Furthermore, in this approach, the obtained AoA is smoothed using a moving average. The latter step neglects the flow field unsteadiness and discards the vortices near the blades, which could explain the mild reduction in AoA magnitude compared to method 2 on the downwind side.

4.3.3 Relative velocity

Figures 4.11a and 4.11b display the dimensionless relative velocities experienced by the blade, estimated by the two methods during the last turbine rotation cycle, in the CFD simulations utilizing the SST and SSTLM turbulence models, respectively. These results are compared with those derived from geometric relationships, i.e., without induction effect. Method 2 predicts trends in relative velocity comparable to the geometric counterpart for a large portion of the first half of the rotation cycle, as indicated by the values listed below, which are also summarized in Table 4.1:

- In the SST case, the maximum value of $U_{\text{rel}}/\lambda U_{\infty} = 1.45$ at $\theta = 8°$ and the minimum value $U_{\text{rel}}/\lambda U_{\infty} = 0.58$ at $\theta = 166°$.
- In the SSTLM case, the maximum value $U_{\text{rel}}/\lambda U_{\infty} = 1.49$ at $\theta = 13°$ and the minimum value $U_{\text{rel}}/\lambda U_{\infty} = 0.53$ at $\theta = 165°$.
- From the geometric expression: the maximum value $U_{\text{rel}}/\lambda U_{\infty} = (\lambda + 1)U_{\text{rel}}/\lambda U_{\infty} = 1.48$ at $\theta = 0°$ and the minimum value $(\lambda - 1)U_{\text{rel}}/\lambda U_{\infty} = U_{\text{rel}}/\lambda U_{\infty} = 0.519$ at $\theta = 180°$.

Table 4.1: Extrema of the non-dimensional relative velocity: Maximum and Minimum values.

Case	**Geometric**	**SST**	**SSTLM**
Maximum $U_{\text{rel}}/\lambda U_{\infty}$	1.48	1.45	1.49
Minimum $U_{\text{rel}}/\lambda U_{\infty}$	0.519	0.58	0.53
Azimuthal angle of the Max. $U_{\text{rel}}/\lambda U_{\infty}$	0°	8°	13°
Azimuthal angle of the Min. $U_{\text{rel}}/\lambda U_{\infty}$	180°	166°	165°

During the second half of the rotation cycle, extending up to $\theta = 270°$, the relative velocities for both SST and SSTLM exceed, in magnitude, those derived geometrically. Around $\theta = 270°$, a notable reduction is observed, which can be attributed to the interaction of the blade with the wake produced by the shaft [156].

Except for the second half of the downwind quadrant of the rotation, method 1 exhibits a substantial underestimation of the relative velocities for both SST and SSTLM cases. The results obtained from the SST case appear to be phase-shifted by approximately -45° in relation to the geometric values during the first half of the rotation cycle.

Given these findings, subsequent discussions will focus exclusively on the results obtained using method 2.

Figure 4.12 illustrates the variations of the chord-based Reynolds number, Re_c, over the last turbine revolution, plotted against the azimuthal angle, θ. During its rotation, the blade encounters a range of Re_c values, varying from 11780 to 33592. To define a single representative number for the static computations in XFOIL, the average value in the windward quadrant is computed:

$$\overline{Re}_c = \frac{2}{\pi} \int_{-\pi/4}^{\frac{\pi}{4}} Re_c \, d\theta \simeq 3.3 \times 10^4 \tag{4.1}$$

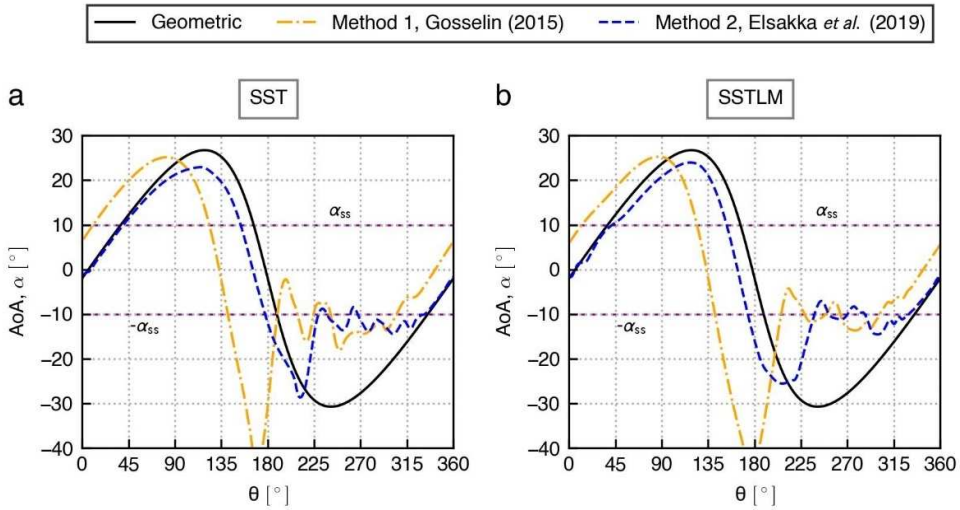

Figure 4.9: Comparison of the estimated AoA for blade 1 from CFD data using method 1 [139], method 2 [140], and the geometric AoA, over the last turbine revolution: (a) SST case, (b) SSTLM case.

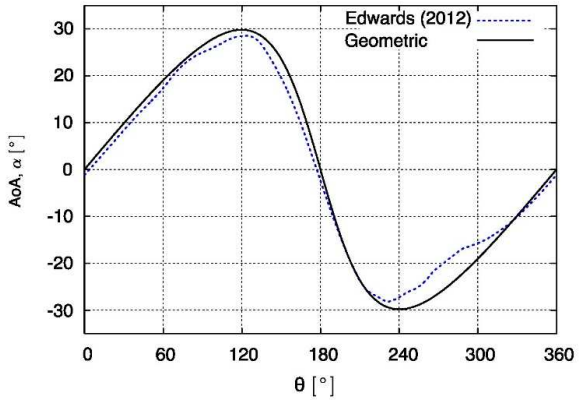

Figure 4.10: Estimation of the AoA using the method of Edwards [156].

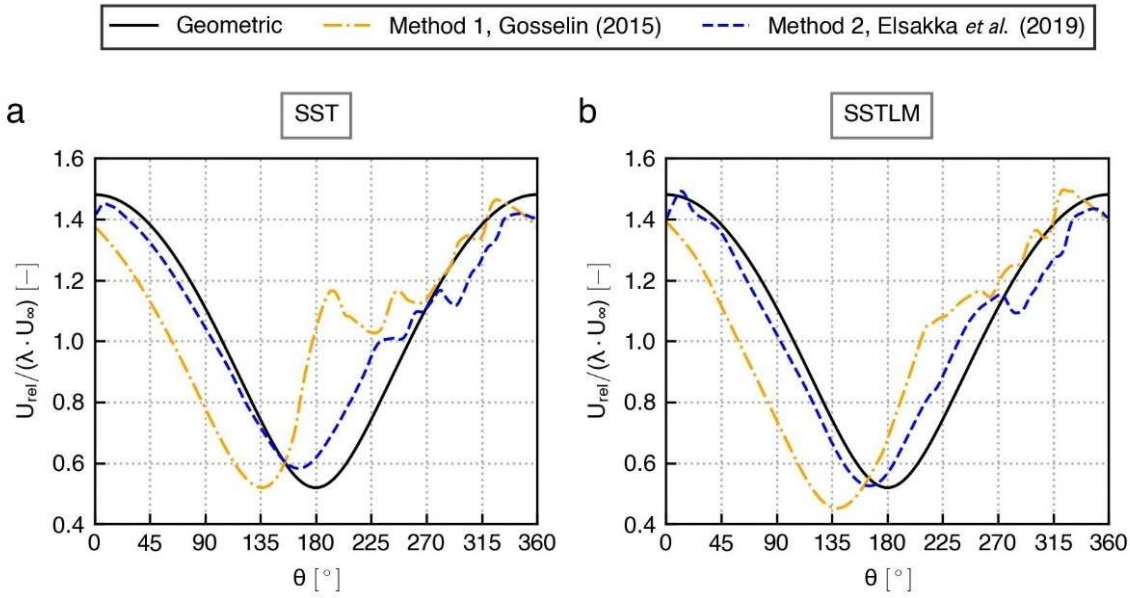

Figure 4.11: Comparison of the estimated non-dimensional relative velocity for blade 1 using method 1 [139], method 2 [140], and the geometrically-derived relative velocity for the last turbine revolution: (a) SST case, (b) SSTLM case.

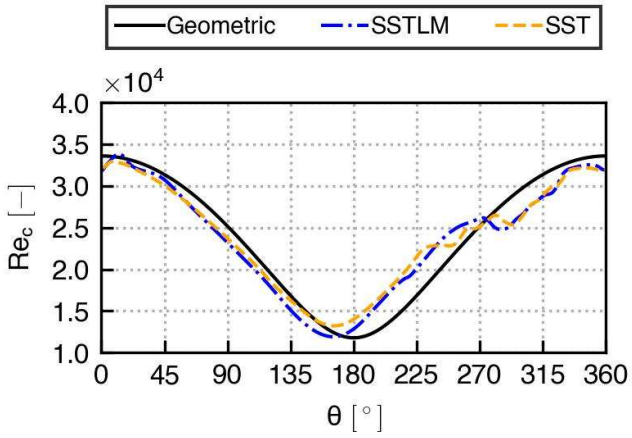

Figure 4.12: Variations of Reynolds number for blade 1 over the last rotation cycle: comparison of the results of SST & SSTLM cases using method 2 [140] and the geometric expression.

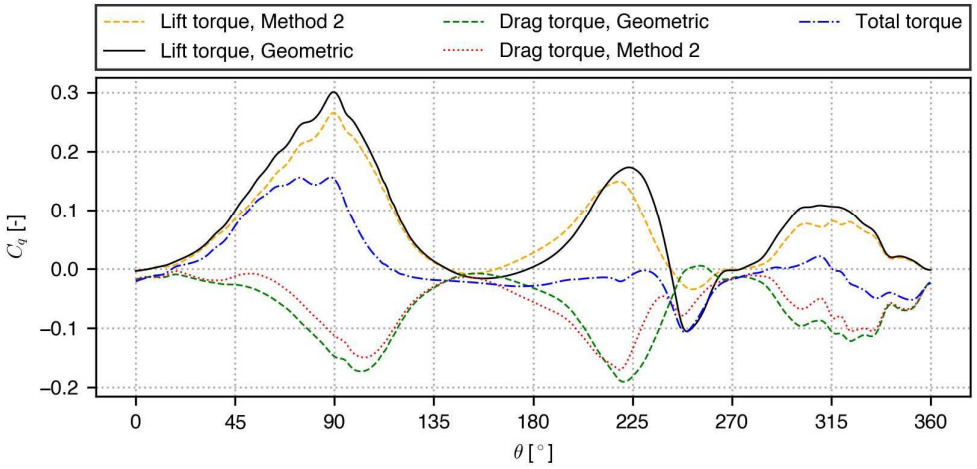

Figure 4.13: Comparison of the lift and drag components of torque using method 2 [140] for the SSTLM case and the geometrically derived expression for blade 1 during the last turbine revolution.

4.3.4 Dynamic loads on the blades

The resultant aerodynamic force acting on the blade, which is computed irrespective of the AoA estimation method, can be resolved into its lift and drag components using either method 2 or the geometric expression of AoA. The impact of the method chosen for this purpose is illustrated in Figure 4.13. The figure presents the contributions of these components to the torque acting on the blade throughout the entire rotation cycle. The high geometric AoA results in a notable overestimation of the lift component of the torque compared to method 2, particularly on the downwind part. This overestimation is more pronounced at $\theta = 225°$ and $\theta = 310°$, with relative deviations are 35% and 55%, respectively. In contrast, in the upwind part, the overestimation is less pronounced, attaining 15% at $\theta = 90°$. Additionally, the drag component is significantly overestimated when using the geometric AoA, reaching as high as 200% at $\theta = 54°$ in the upwind region and 100% at $\theta = 290°$ in the downwind region.

Subsequent analysis employs method 2 to resolve the aerodynamic forces acting on the blade into lift and drag coefficients. See (Eq. 3.1) and (Eq. 3.2). The dynamic coefficients C_l and C_d are depicted in Figures 4.14a and 4.14b, respectively.

During the fore half of the rotation cycle, C_l and C_d display large amplitudes of variations, suggesting the occurrence of dynamic stall. The SSTLM model predicts dynamic stall at

earlier azimuthal positions. The sharp drop in lift is observed at approximately $\theta = 90°$, while the SST model indicates stall occurring around $\theta = 108°$.

To provide more details about the dynamic stall occurrence on the blade surface, the non-dimensional spanwise vorticity contours are presented in Figure 4.15 at five azimuthal angles: $\theta = 45°$, $\theta = 90°$, $\theta = 108°$, $\theta = 212°$, $\theta = 233°$ for the SST and, $\theta = 45°$, $\theta = 90°$, $\theta = 108°$, $\theta = 219°$, $\theta = 245°$ for SSTLM cases, respectively. The following observations are made:

- At $\theta = 45°$: the SST model predicts a slightly separated boundary layer (BL), whereas the SSTLM model predicts a mildly separated BL near the trailing edge of the blade that starts to progress toward the leading edge of the blade.
- At $\theta = 90°$, the large leading-edge vortex (LEV) is about to shed from the blade's surface, but it is still building up in the SST case, which explains the delay in stall occurrence between the two cases.
- At $\theta = 108°$: the DSV in the SST case is about to shed. In the SSTLM case, the dynamic stall vortex (DSV) is convecting away from the blade's suction surface with the formation of a Trailing Edge Vortex (TEV) near the trailing edge of the blade.

The azimuthal angles from $\theta = 212°$ to $\theta = 233°$ in the SST case and from $\theta = 219°$ to $\theta = 245°$ in the SSTLM case correspond to the blade interacting with the vortex shed by the preceding blade. Notably, these ranges align with a marked decrease in the magnitude of the estimated AoA using method 2 (Figure 4.9a and 4.9b), which correlates with reductions in both lift and drag coefficients.

Given that in this study the reduced frequency $\kappa = 0.29$, computed using Eq. (1.13) is relatively high, hysteresis loops in the aerodynamic coefficients C_l and C_d are expected. To demonstrate this behavior, the dynamic coefficients C_l and C_d obtained from the CFD simulations using method 2 with SST and SSTLM turbulence models, are displayed alongside the static coefficients from the experimental data by Laneville and Vittecoq [22] and XFOIL computations in Figure 4.16.

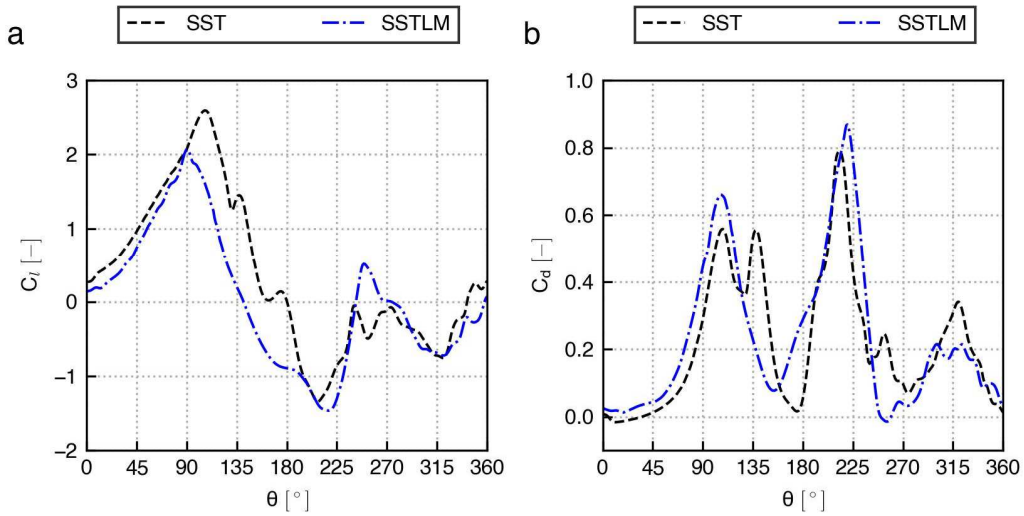

Figure 4.14: Variations of dynamic coefficients for one blade throughout one revolution cycle using method 2 [140] employing SST and SSTLM turbulence models: a) lift coefficient, b) drag coefficient.

The following observations can be made:

- **Static coefficients:**

The C_l computed using XFOIL increases linearly with AoA, α, and follows the trend of the experimentally measured C_l by Laneville and Vittecoq [22] up to $\alpha = 4°$. Although XFOIL accurately predicts the static stall angle at $\alpha_{ss} = 10°$ (where $C_{l,max} = 0.71$) as the experimental value, it tends to overestimate the lift beyond this angle. This overestimation of lift, particularly for thick airfoils, is a known limitation of the code where lift overprediction is more pronounced [159]. Conversely, the drag coefficient C_d predicted by XFOIL aligns closely with the experimental data for pre-stall AoAs. However, for post-stall AoAs, the C_d is underestimated.

- **Dynamic coefficients:**
  - SST case: Figures 4.16a and 4.16c

The computed C_l is in close alignment with the experimental values for AoAs ranging from $\alpha = 5°$ to $\alpha = 8°$. It is important to note that the predicted C_l at zero AoA is not zero. In fact, at $\alpha = 0$, $C_l = 0.37$. This is attributed to flow curvature effects due to the rotation of the blades. Under such conditions, a symmetrical airfoil appears to have a virtual camber. This observation is consistent with prior studies by Laneville and Vittecoq [22] and Amet et al.

[54], who have reported similar lift effects at zero AoA for symmetrical airfoils. As α increases beyond the static stall angle, α_{ss}, the dynamic C_l continues to increase linearly but at a steeper rate, achieving a maximum $C_{l,max} = 2.6$ at $\alpha = 22.5°$ (corresponding to an azimuthal angle of $\theta = 105°$).

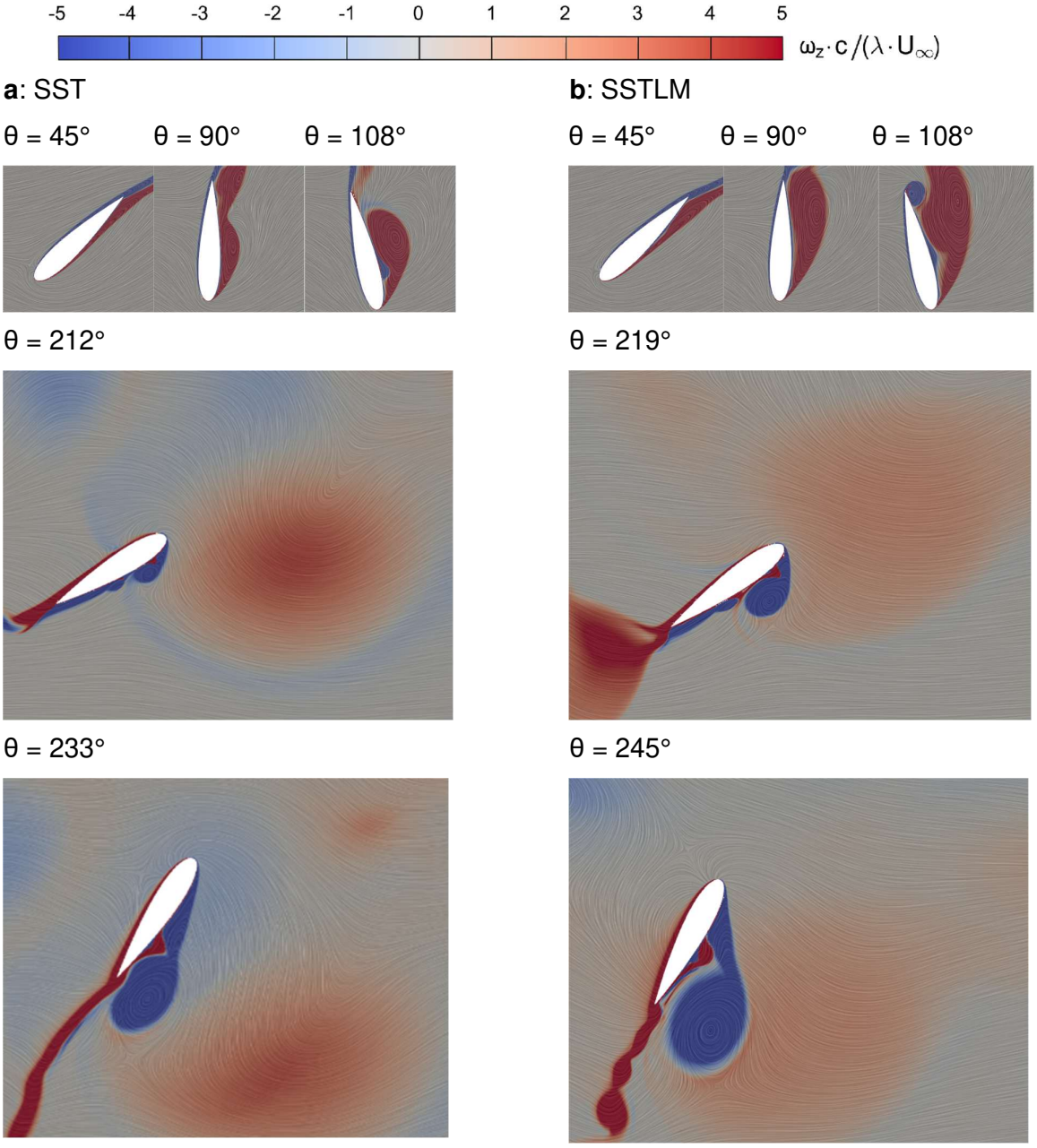

Figure 4.15: Contours of non-dimensional spanwise vorticity around the blade at θ = 45°, θ = 90°, and θ = 108°, θ = 212°, θ = 233° (for the SST case), and θ = 45°, θ = 90°, and θ = 108°, θ = 219°, θ = 245° (for the SSTLM case).

The maximum value is approximately 3.66 times that of the static airfoil's $C_{l,max}$. The increase in lift is accompanied by a rise in drag, which is slightly in phase. The drag coefficient reaches a maximum of $C_{d,max} = 0.56$ at $\alpha = 22.7°$ (at $\theta = 108°$). Following the peak, both C_l and C_d exhibit a substantial drop. These patterns of lift and drag are indicative of deep dynamic stall occurring on the blade surface facing the shaft. The dynamic stall is linked to the boundary layer events characterized by the growth of a leading-edge vortex (LEV), its detachment, and convection. The decrease in dynamic coefficients occurs as this vortex passes beyond the blade's trailing edge.

The abrupt increase in C_l and C_d during the downstroke as the AoA continues to decrease near $\alpha = 20.6°$ ($\theta = 131°$) is associated with the formation of a secondary vortex. Following its shedding, C_l (C_d) continues to decrease, reaching lower (higher) levels compared to their upstroke counterparts at the same AoAs. For negative AoAs, corresponding roughly to the aft half of the blade rotation ($\theta = 180°$ to $360°$), the C_d curve reaches a much higher value of 0.79 at $\alpha = -28.4°$ ($\theta = 213°$), while the C_l only reaches a value of -1.33 at $\alpha = -26.7°$ ($\theta = 208°$). It is worth noting that the DSV, visible within the ranges of $\theta = 212°$ to $233°$ (for SST) and $\theta = 219°$ to $245°$ (for SSTLM), as depicted in Figure 4.15, emerges from the leading edge of the blade's outer surface. This differs from the upwind angles where the DSV originates from the trailing edge and progresses toward the leading edge. This manifestation of the DSV is likely due to the boundary layer eruption due to blade-vortex interaction, as documented in studies like those by Rival et al. [160] and Peng and Gregory [161]. The fluctuations in the curves at increasing angles are linked to blade-vortex interactions [157], which are more pronounced between $225° < \theta < 315°$ (See Figure 4.9).

- SSTLM case, Figures 4.16b and 4.16d

The results from the SSTLM model indicate roughly similar hysteresis loops for C_l and C_d. Observations from these results include:

- The lift generation predicted from $\alpha = 0°$ to α_{ss} is lower than the static values, while the drag coefficient aligns closely with the experimental data for the static airfoil. This likely results from delayed boundary layer re-attachment to the blade surface at low azimuthal angles.
- The maximum lift coefficient reaches $C_{l,max} = 2.1$, which is 2.9 times the maximum C_l for the static airfoil, at $\alpha = 20.8°$ ($\theta = 90°$).

- C_d reaches a maximum value of $C_{d,max} = 0.66$ at $\alpha = 23.2°$ (at $\theta = 106°$).
- In the aft half of the rotation, C_l attains a value of -1.46 at $\alpha = -24.8°$ (at $\theta = 219°$), while the maximum $C_d = 0.87$ at $\alpha = -24.4°$ ($\theta = 220°$) is 10% higher than the value predicted by the SST model for this region.

The predicted hysteresis loops of dynamic lift and drag for a VAWT blade, as shown in Figure 4.16, match those of an airfoil undergoing sinusoidal pitching. For example, Figure 4.17 from the study by Lee and Gerontakos [93] depicts experimental results for an oscillating NACA0012 airfoil where $\alpha(t) = 10° + 15° \sin(\omega t)$, at a reduced frequency $\kappa = \omega c/2U_\infty = 0.1$, and a Reynolds number of 1.35×10^5. There is a clear similarity in the trends of hysteresis loops for lift and drag coefficients between the VAWT blade in the present study (for both SST and SSTLM cases) and the oscillating airfoil shown in Figure 4.17. This similarity is particularly pronounced as the AoA increases beyond the static stall angle ($\alpha_{ss} = 13°$ in the experiment). Both lift and drag coefficients exhibit increases to peak values followed by sharp decreases due to dynamic stall phenomenon, reflecting common aerodynamic characteristics between the VAWT blade and the oscillating airfoil. These findings indicate that changes in the perceived AoA are primary contributors of the flow unsteadiness that leads to significant boundary layer phenomena on the surface of the blade [142].

4.3.5 Modified Gosselin Method

In subsection 4.3.2, a comparative analysis was conducted between the two methods by Gosselin [139] (method 1) and Elsakka *et al.*[140] (method 2) for estimating the blade AoA. A noticeable phase difference between the two methods was observed. To quantitatively assess this difference, we employ cross-correlation. This statistical methodology evaluates the degree of similarity between two time-series datasets (or signals) as a function of the lag of one series relative to the other.

If we represent the AoA dataset computed using method 1 as $X[n]$ and that from method 2 as $Y[n]$, with each set containing N samples, then the cross-correlation $R_{XY}[m]$ is defined as:

$$R_{XY}[m] = \sum_{n=0}^{N-1} X[n] \cdot Y[n+m] \tag{4.2}$$

Where m denotes the lag between the two signals. The summation is carried out over all n, ranging from 0 to $N-1$. When the maximum value of $R_{XY}[m]$ is identified; it corresponds to a shift in the azimuthal angle, denoted as $\theta[m]$.

In applying this method to both the SST and SSTLM cases, we observe an azimuthal shift of 34° in the SST case and 33° in the SSTLM case. These results are outlined in Table 4.2 and illustrated in Figure 4.18.

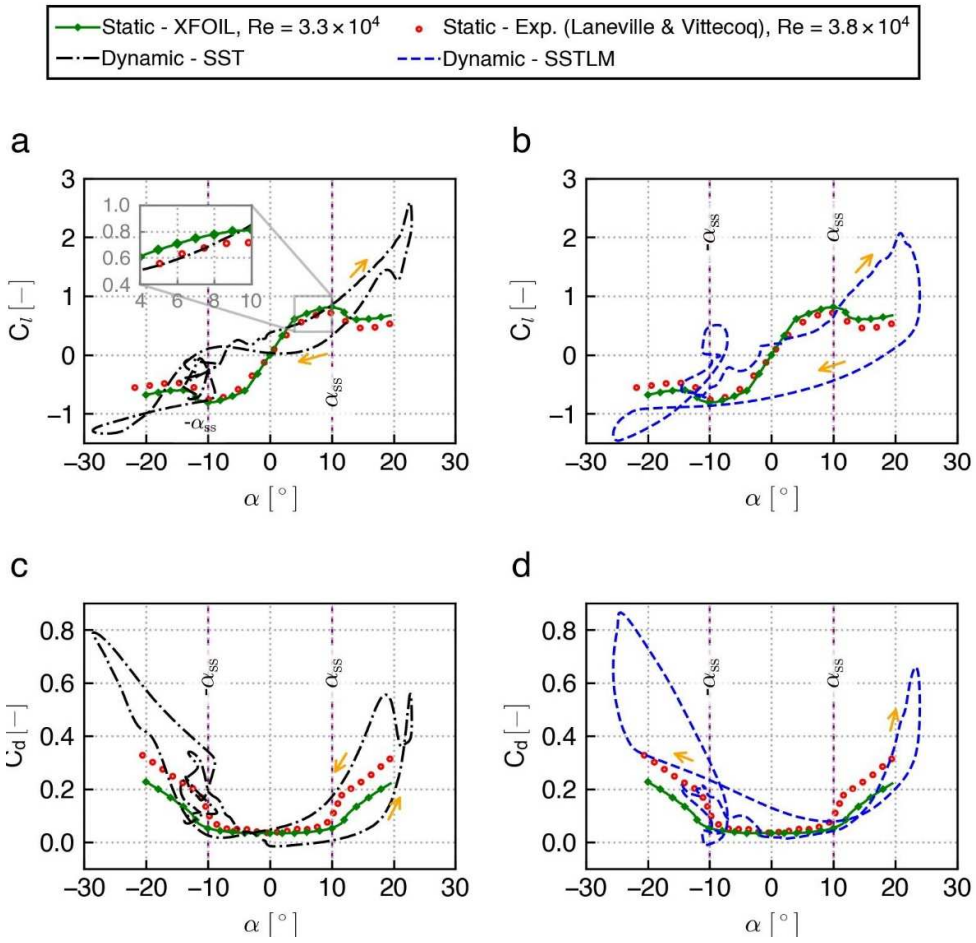

Figure 4.16: Comparison of dynamic coefficients of blade 1 using method 2 [140] with static coefficients from XFOIL and the experimental data of Laneville and Vittecoq [22] . Lift coefficient: a) SST, b) SSTLM turbulence models. Drag coefficient: c) SST, d) SSTLM turbulence model.

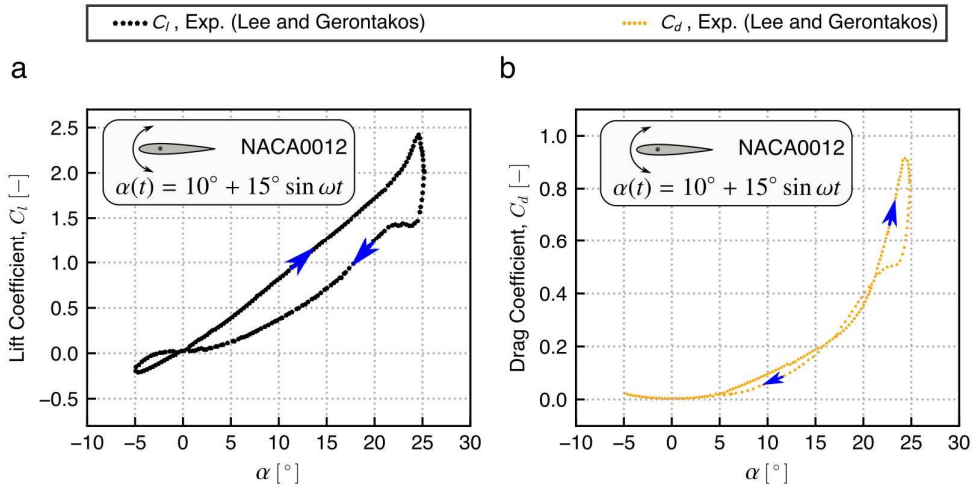

Figure 4.17: Dynamic coefficients of NACA0012 airfoil from the experiment of Lee and Gerontakos [93]. (a): Lift coefficient, (b): Drag coefficient.

Table 4.2: Azimuthal shifts for Modified Method 1 in SST and SSTLM cases.

Case	**Azimuthal shift, $\theta[m]$**
SST	34°
SSTLM	33°

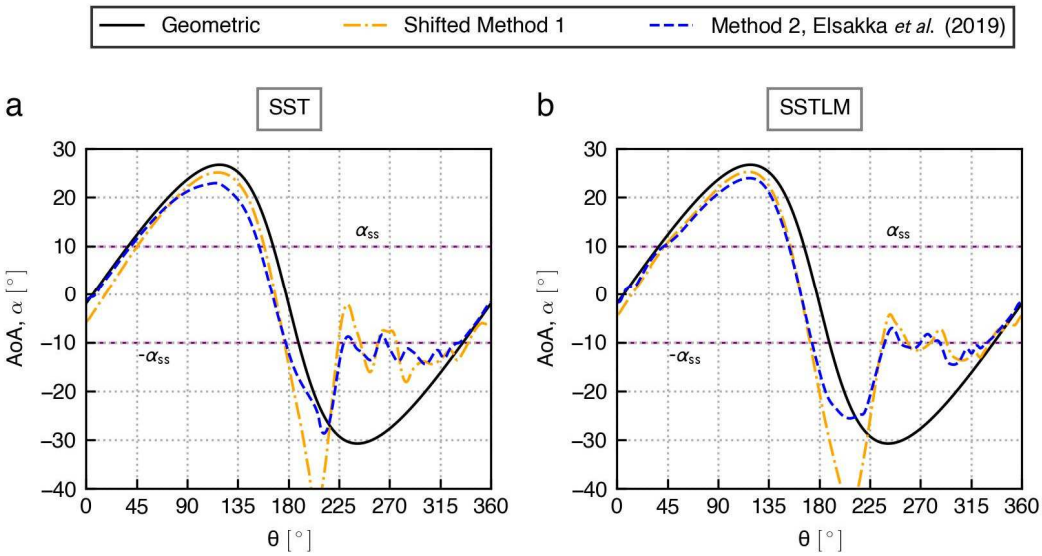

Figure 4.18: Comparison of the Modified Method 1 using Cross-Correlation Analysis with Method 2: (a) SST case (b) SSTLM case.

Figures 4.18a and 4.18b present a comparison of the adjusted method 1 with method 2 for the SST and SSTLM results, respectively. The modification of method 1 demonstrates a high

level of similarity to method 2, indicating a substantial enhancement in the predictions of method 1n as it more closely aligns with the trends observed in method 2. The similarity is notable across nearly the full rotation cycle, aside from the range $\theta \in [180°, 225°]$, where the discrepancy between the two methods is large, which is inherently present in the original method 1. It should be noted that the observed azimuthal shift for the SST and SSTLM cases, approximately 34° and 33°, respectively, correlates with the relative azimuthal angle of the probing location of method 1 to the blade, which is calculated as $2c/R$. The latter is approximately 36.67° in the present study.

4.4 Numerical and experimental studies of the wake

In this section, we discuss the findings from the third study, which focuses on the characterization of VAWT wakes using both numerical simulations and PIV measurements.

It is pertinent to mention that the data from the numerical simulations are time-averaged over the last turbine revolution (21st revolution). For streamwise, u, and lateral, v, velocities, this can be expressed as follows:

$$\overline{u} = \frac{1}{T}\int_0^T u \, \mathrm{d}t$$

$$\overline{v} = \frac{1}{T}\int_0^T v \, \mathrm{d}t$$

Where T is the rotation cycle, i.e., the time required for the turbine to complete a full rotation. The averaging is computed for each cell in the computational grid. Special care is required to compute these averages over the rotating zone correctly. The results must be sampled to a fixed, sufficiently refined plane at each time step. The time averages are then computed over this plane.

On the other hand, the PIV results show a phase-average of over 200 turbine revolutions.

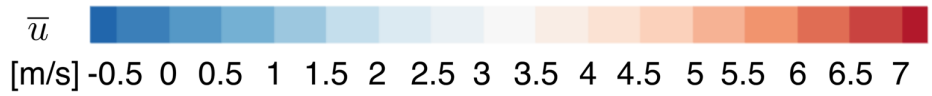

a: Experimental, PIV

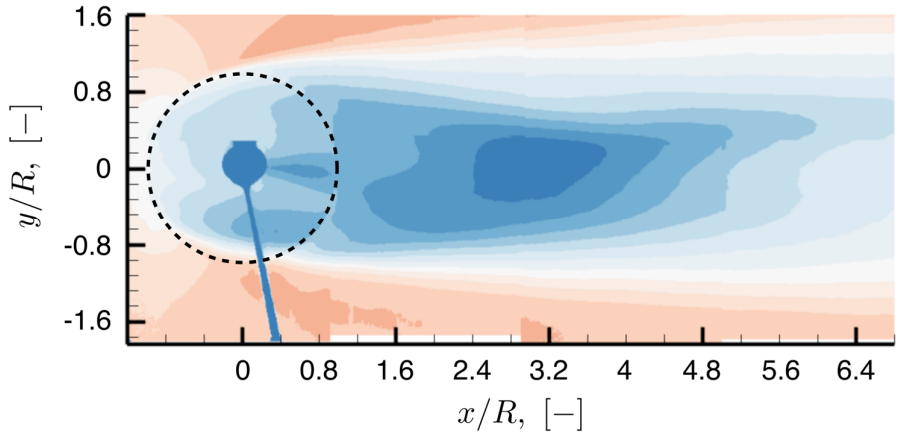

b: SSTLM

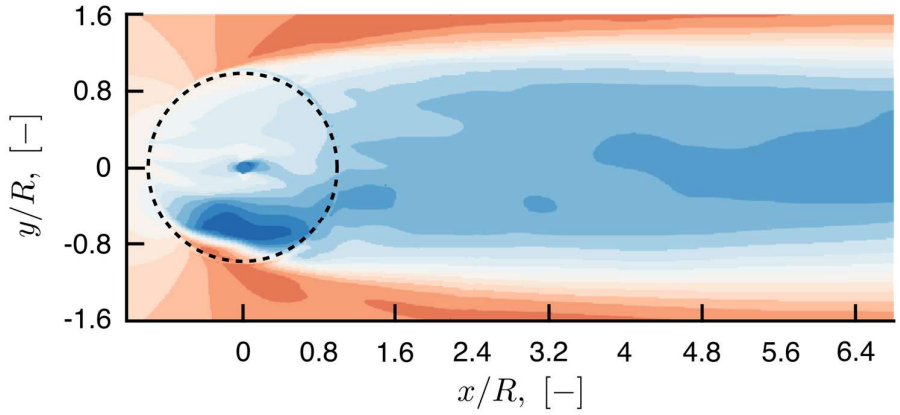

c: SST

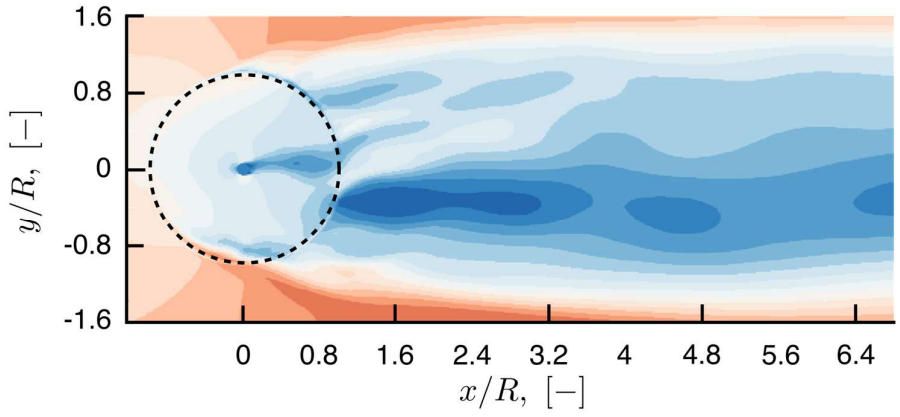

d: SA

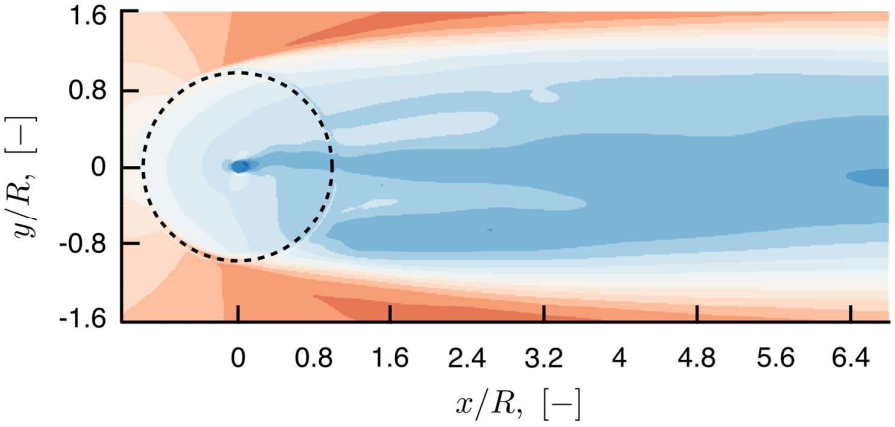

Figure 4.19: Averaged streamwise velocity contours in the wake at TSR = 2.5. Comparison between the PIV results (phase-averaged over 200 turbine revolutions) and numerical computations (time-averaged over the last 21st turbine revolution). (a): PIV results, (b): SSTLM results, (c): SST model, (d): Spalart-Allmaras model.

Figure 4.19 presents a comparison of the streamwise averaged velocity contours between experimental data obtained through PIV and numerical computations using different turbulence models. The figure is divided into four sub-figures, with Figure 4.19a depicting the phase-averaged streamwise velocity contours from PIV measurements (over 200 turbine revolutions), Figure 4.19b, Figure 4.19c, and Figure 4.19d representing the numerical results, time-averaged over the last turbine revolution, from SSTLM, SST, and SA models respectively.

In evaluating the fidelity of the turbulence models, it is observed that each model exhibits a varying degree of accuracy in predicting the wake velocity deficit in terms of the length of the near-wake region and the wake expansion in the lateral direction y.

For a detailed analysis of the wake, Figure 4.21 depicts the profiles of the normalized time-averaged streamwise velocity, $\bar{u}/U_\infty$, along the lateral direction, $-1.6 \leq y/R \leq 1.6$ at several downstream locations, x/R. as shown in Figure 4.20.

Figure 4.20: Diagram of wake locations downstream of the wind turbine.

The figures indicate that all turbulence models tend to underpredict the streamwise velocity deficit up to $x/R = 4.8$. Specific observations are as follows:

- On the retreating side of rotation (i.e., $y/R < 0$), the SSTLM model demonstrates a reasonable accuracy in predicting velocity, closely aligning with the experimental measurements. The SA model also performs well in this region, though it is slightly less accurate than SSTLM. However, predictions by the SST model exhibit noticeable discrepancies with large ripples, which warrants further discussion below.
- On the advancing side, $y/R > 0$, the performance of all models is less satisfactory when compared to the experimental data. This indicates a challenge for the models in accurately capturing the dynamic on this side of the turbine rotation.

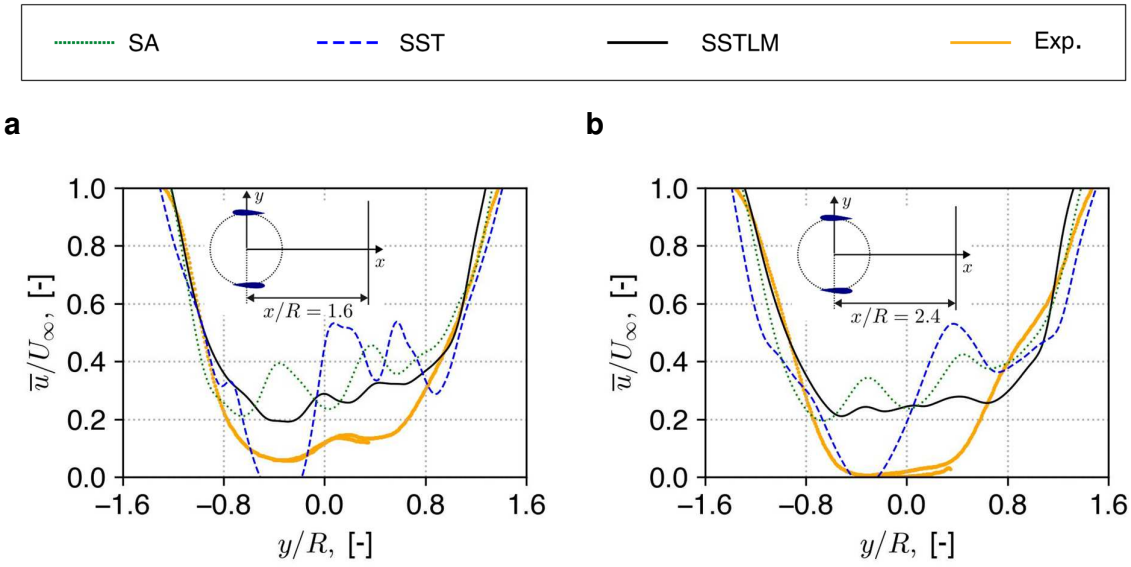

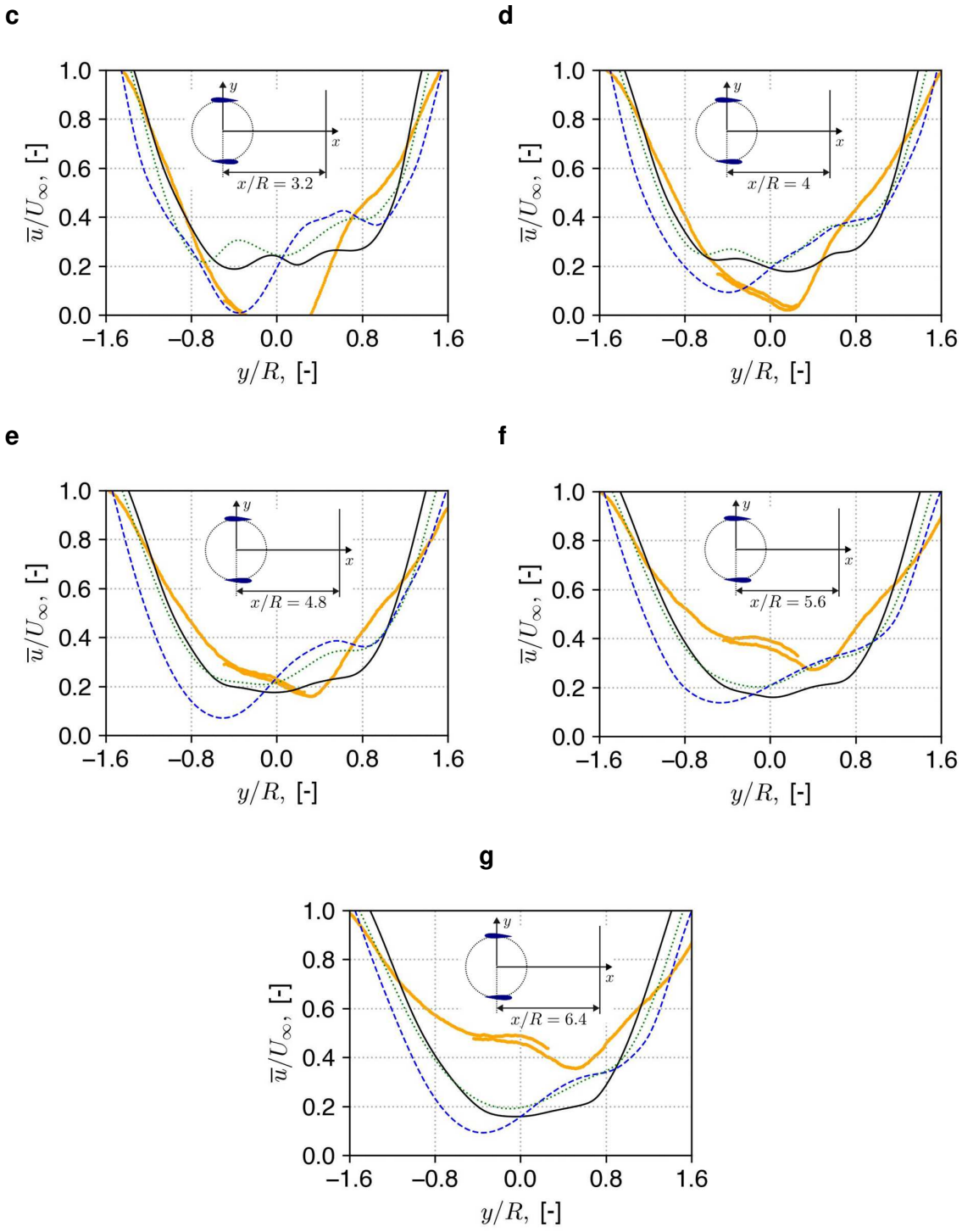

Figure 4.21: Normalized time-averaged streamwise velocity over the last turbine revolution, in the lateral direction y at different downstream positions: $x/R = 1.6$ (a), $x/R = 2.4$ (b), $x/R = 3.2$ (c), $x/R = 4$ (d), $x/R = 4.8$ (e), $x/R = 5.6$ (f), and $x/R = 6.4$ (g). Results are compared with the PIV data (phase-averaged over 200 turbine revolutions). TSR = 2.5.

- Further downstream, beyond $x/R = 4.8$, all the models tend to overpredict the velocity deficit in this region. Contrary to these predictions, the experimental results indicate a clear recovery in the wake. Moreover, the experimental results reveal a distinct asymmetry about $y/R = 0$. Specifically, there is a noticeable velocity deficit on the advancing side ($y/R > 0$) compared to the retreating side ($y/R < 0$). This asymmetry, however, is not captured by the models.

Figure 4.22 depicts the normalized time-averaged lateral velocity profiles, $\overline{v}/U_\infty$, in the wake of the turbine. The comparison with PIV data reveals that all the models demonstrate less satisfactory agreement. Notably, the SA and SSTLM predictions are closely aligned with each other.

Overall, the above observations necessitate a detailed examination to elucidate the underlying factors contributing to the variations observed between the numerical computations and the PIV data, particularly regarding wake recovery and asymmetry.

These observed differences can be attributed to a range of factors, such as:

- The simplifications in the numerical computations regarding the actual geometry of the turbine. In these simulations, structural elements such as struts and the finite aspect ratio of the blades (blade chord to the blade span) are not represented.
- The PIV data are phase-averaged over 200 turbine revolutions, while the simulations are time-averaged over only the last turbine revolution (21st revolution), a constraint imposed by the high computational costs.
- The inability of the 2D simulations to accurately capture the wake recovery predicted in the experiment is not surprising. This limitation arises mainly from the inherent nature of 2D modeling, which cannot account for the spanwise motions (i.e., in the z-direction). Such spanwise motions and the vortices shed from the blades' tips play a considerable role in the wake recovery process by propelling the fluid toward the wake center [162,163].
- The simulations not adequately capturing the wake asymmetry could be due to inherent limitations in the RANS approach [164].
- The observed ripples in the streamwise velocity deficit, more pronounced in the results of the SST model at $x/R = 1.6$ (Figure 4.21a), and $x/R = 2.4$ (Figure 4.21b), can be attributed to strong vortices shed from the blades and the shaft and convected

downstream as shown in Figure 4.23b. The intensity of these vortices is likely overestimated by the SST model compared to the SA (Figure 4.23c) and the SSTLM (Figure 4.23a) models. This is in agreement with the findings of Bianchini et al. [165], who also noted similar behavior of the SST model. In the latter models, the vortices appear more diffused, resulting in fewer ripples in the velocity deficit. It should be noted that the contours depicted in Figure 4.23 are from instantaneous snapshots at an azimuthal location $\theta = 260°$ to illustrate the distinct vortices rather than representing averaged contours.

It is worth noting that wake asymmetry in VAWTs is subject to various conflicting explanations in the literature. Araya et al. [166] attribute the asymmetry to stronger shear layers on the advancing side of the turbine. Bachant and Wosnik [163] link it to the vortex shedding asymmetry between the advancing and the retreating sides due to different AoAs perceived by the blades. Hohman et al. [167] suggest that the momentum deficit on the advancing side results from the majority of power being generated there. Strom et al. [168] offer an alternative explanation based on the power distribution within the turbine. They suggest that the torque production from the tangential force on the blade, predominantly on the upstream side of the rotor, results in a time-average rotor force in the opposite direction due to momentum conservation.

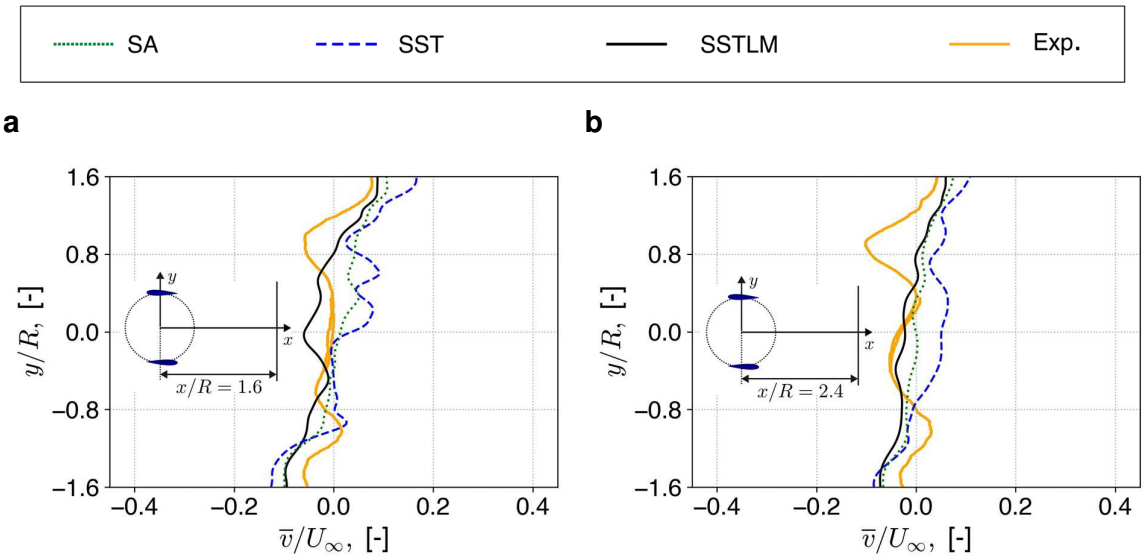

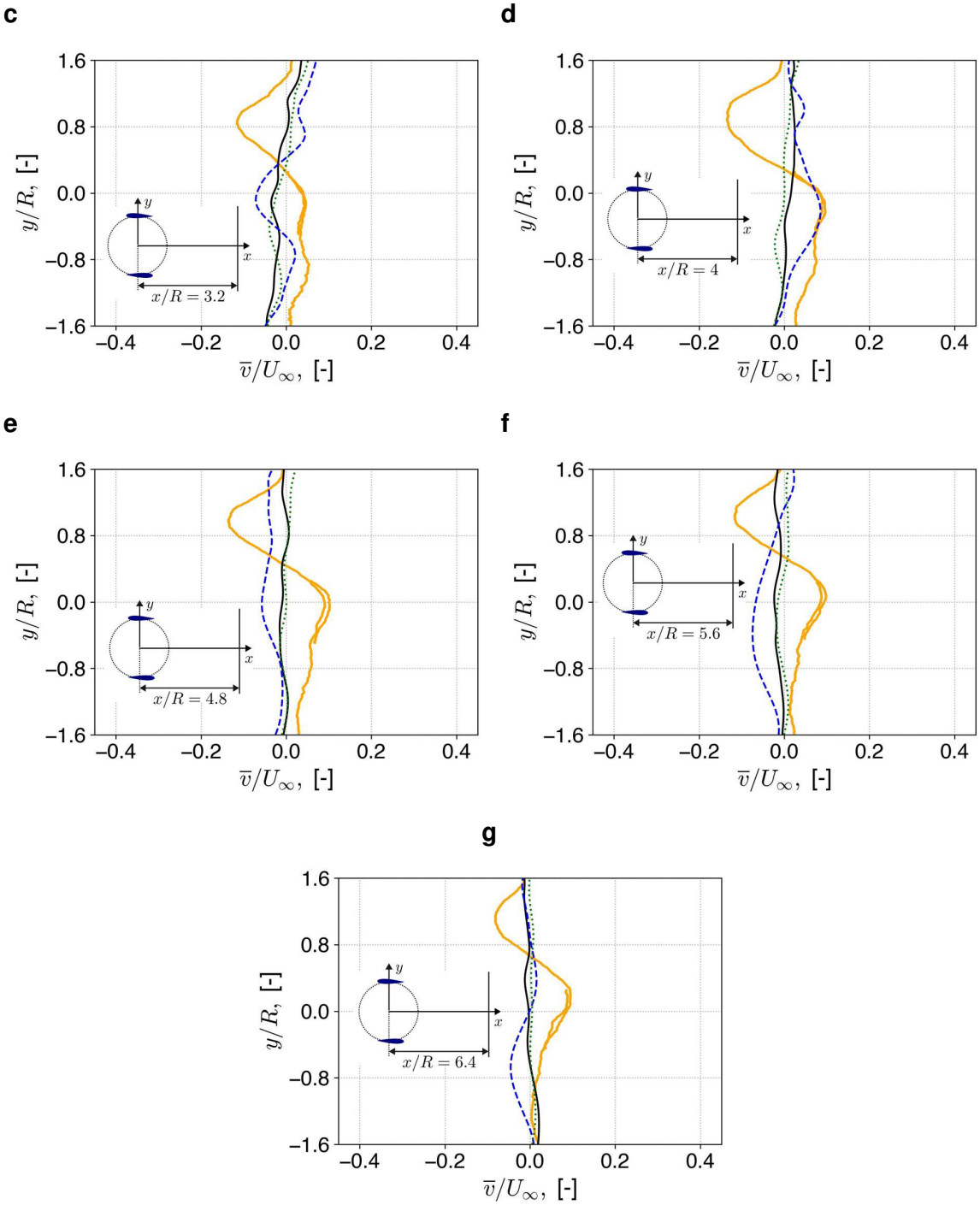

Figure 4.22: Normalized time-averaged, over the last rotation cycle, lateral velocity along the lateral direction y at different downstream positions in the turbine wake. Results are compared with the PIV data (phase-averaged). TSR = 2.5.

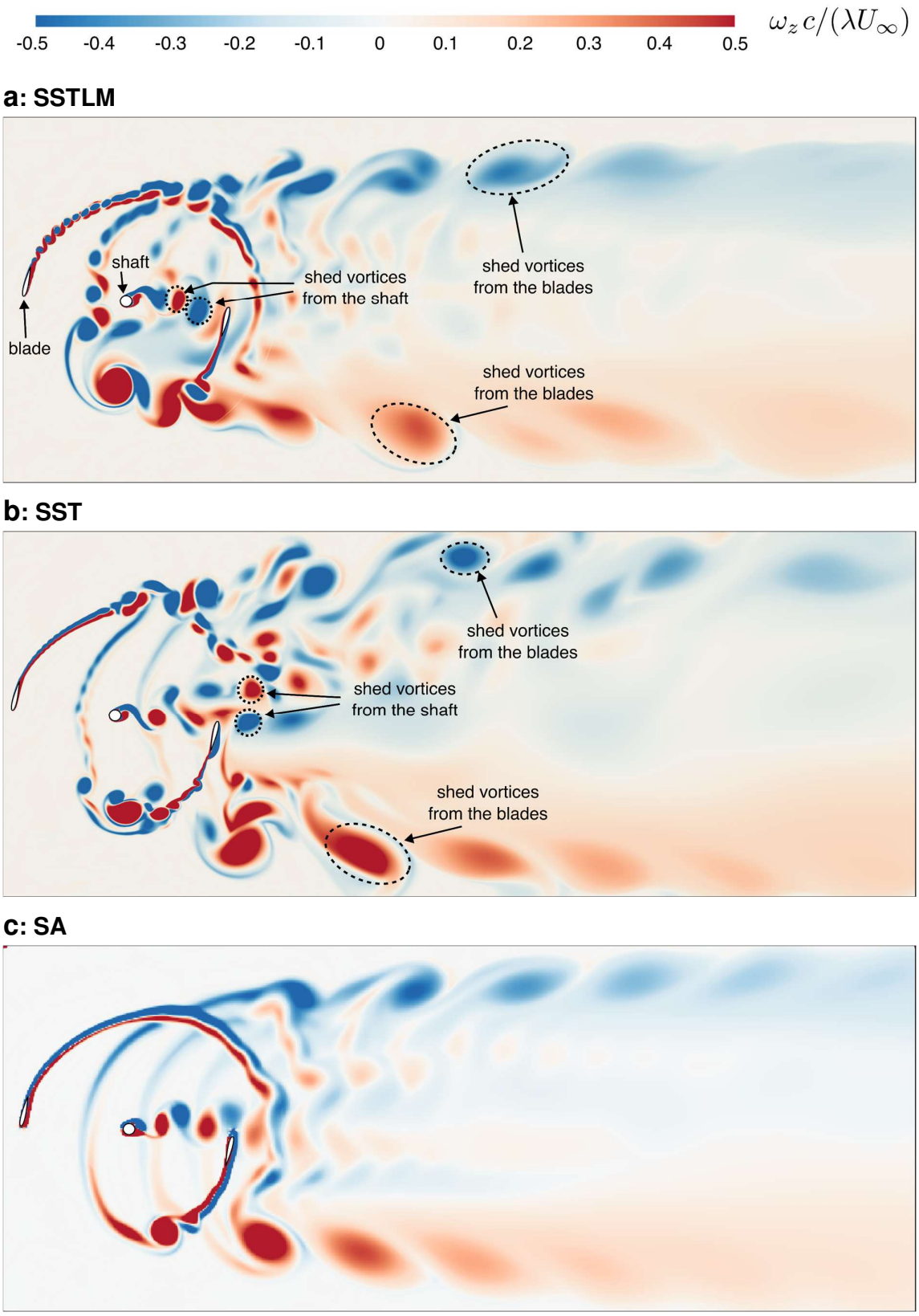

Figure 4.23: Contours of the instantaneous normalized spanwise vorticity at $\theta = 260°$. TSR = 2.5.

From the experimental results of this study, it becomes apparent that 3D effects play a significant role in the dynamics of VAWT wakes. While it is increasingly recognized that 3D simulations are essential to accurately capture these effects, particularly for correct prediction of wake recovery and assessment of the RANS approach's suitability for predicting wake asymmetry, there are practical challenges to their adoption.

Examination of 3D studies in the literature reveals that most of these studies on VAWT wakes often employ coarse meshes and large time steps, and the simulations are run only for a few turbine revolutions. This raises concerns about the statistical convergence of the results. A notable study by Balduzzi et al. [73] highlights the promise of high-fidelity 3D simulations, employing high-resolution meshes and suitable time steps to yield more reliable results. However, their simulations, which modeled only half of the rotor, with a single blade, using a symmetry boundary condition at the mid-span of the blade, required the use of at least 16000 CPU cores for approximately one month. This considerable demand for computational resources is the primary reason our study opted for 2D simulations.

4.5 Summary

In this chapter, we presented the results of various numerical studies conducted as part of this work. Initially, we explored the significant impact of turbulence model selection on predicting the deep dynamic stall phenomenon. Secondly, we demonstrate the importance of accurately resolving aerodynamic forces on VAWT blades into lift and drag components. This necessitated estimating the angle of attack and relative velocity perceived by the blades, a particularly challenging aspect of VAWT operation. We also emphasized the importance of using a turbulence model that accounts for laminar-to-turbulent transition in the development of dynamic stall and its effects on the blade vortex interactions on the downwind side of the rotation. Lastly, we investigated the wake of a small VAWT through both numerical studies and PIV. These results highlighted the complexity inherent in characterizing VAWT wakes and the substantial computational resource for accurate predictions for such analyses.

Conclusions and Perspectives

5.1 General conclusions

VAWTs present several advantages over HAWTs and have the potential to contribute significantly to the wind energy field. While HAWTs have traditionally dominated due to their efficiency and mature technology, VAWTs offer unique benefits. For instance, VAWTs eliminate the need for a yaw mechanism, as they can accept wind from any direction, thereby reducing mechanical complexity and potential failure points. They have a lower center of gravity, which contributes to increased stability and potentially lower installation and maintenance costs. Furthermore, VAWTs have been found to exhibit higher efficiency in highly turbulent winds and have high potential in wind farms as they offer higher energy density per unit of land area compared to HAWTs.

However, despite these advantages, VAWTs suffer from complex aerodynamics that have limited their broader adoption. The complexity primarily arises from critical aerodynamic phenomena such as dynamic stall and blade-wake interactions, among others, which significantly impact turbine performance. A thorough understanding of their aerodynamics is imperative to address these challenges and harness the full potential of VAWTs. From a modeling perspective, this requires high-fidelity simulations based on the solution of Navier-Stokes equations to provide insights into these phenomena and their effects on the wake dynamics for better spacing of the wind turbines in farms.

The present work, therefore, opts for numerical simulations based on the URANS approach to study these complex phenomena. The first study was a detailed analysis of unsteady separated flows around an oscillating airfoil associated with the deep dynamic stall. The aim was to identify the most suitable eddy viscosity turbulence model for such conditions. Three turbulence models were evaluated: Launder Sharma k-ε, Spalart-Allmaras, and the k-ω SST. The results included a comparison of the predicted integral quantities, i.e., aerodynamic loads such as lift, drag, and pitching moment coefficients, with the experimental measurements from the literature for an airfoil with a tripped boundary layer at the leading edge. This study's findings highlight the effectiveness of the k-ω SST model in comparison to other evaluated models, particularly in its ability to predict the hysteresis loops of aerodynamic forces, the pitching moment, and the formation and convection of the dynamic stall vortex. This is evident in two main aspects:

- The k-ω SST model successfully predicts a peak in the pitching moment coefficient of 0.15 or higher, characteristic of a deep stall scenario.

- The model accurately predicts the onset mechanism of dynamic stall for the NACA0015 airfoil. This prediction aligns with experimental findings that demonstrate a trailing-edge type dynamic stall under the conditions considered in the study.

In the second study, we tackled a particularly challenging aspect of VAWT aerodynamics, namely the estimation of the angle of attack (AoA) and relative velocity perceived by the blades. This task is notably complex due to the ambiguity in defining these quantities, especially when considering the variety of complex flows in which VAWT blades operate, such as curvature effects and blade-vortex interactions. To address this, we implemented two methods within the OpenFOAM framework for estimating the AoA and relative velocity. These methods allow monitoring of these quantities during the simulation runtime and in post-processing modes. Consequently, this enables the resolution of aerodynamic forces on the blades into lift and drag, facilitating a comprehensive analysis of the blade's aerodynamics throughout the entire rotation cycle. 2D URANS computations were conducted employing the k-ω SST and the four-equations transitional γ-Re_θ models. The results were validated against experimental datasets for the static stall and topology of the dynamic stall experienced by the blades.

The following points summarize the key findings of the study:

- It was found that the dynamic stall exhibited by VAWT blades has characteristics similar to those encountered by oscillating airfoils in terms of stall delay, development of dynamic stall vortex, and its convection.
- Investigations revealed that the technique involving velocity sampling at two reference points on either side of the blade outperformed the approach that samples the flow fields in front of the blade’s path. A proposed correction to the latter method might rectify the estimations.
- The AoA calculated using geometrical relationships tends to overestimate the actual AoA experienced by the blades, as it does not consider the induction effect on the incoming velocity.
- On the downwind side of rotation, the interaction between the blade and the shed vortices significantly influences the AoA. Consequently, determining the AoA solely through geometrical expressions results in substantial errors.

- Variations in AoA are a significant factor in flow unsteadiness, contributing to complex flow phenomena like dynamic stall, which notably impacts the dynamic loads on the blades at higher reduced frequencies.
- The techniques employed for estimating the AoA and relative velocities hold considerable promise for enhancing VAWT performance. These methods could lead to the development/improvements of/in low-order models.
- Notably, this study could be of substantial value as a guide for researchers in selecting an efficient method for estimating AoA and relative velocity. This is particularly important given that most methods described in the literature require extensive post-processing efforts.

The third study focused on examining the wake dynamics of a small VAWT through a detailed comparative analysis between experimental data obtained from Particle Image Velocimetry (PIV) and numerical computations using various turbulence models, namely k-ω SST (SST), γ-Re_θ (SSTLM), and Spalart-Allmaras (SA) models. This analysis involved examining the performance of each turbulence model in predicting the wake velocity deficit. The velocity profiles are plotted along the lateral (crosswise) direction at several downstream locations to assess the wake asymmetry and recovery observed in the PIV measurements. The investigation also explored the inherent limitations of 2D simulations and their challenges in accurately capturing the complex 3D dynamics of VAWT wakes. Additionally, the study provided a critical examination of the contributing factors to the observed discrepancies between the numerical models and the experimental results, such as geometrical simplifications in the simulations, differences in averaging methods, and the inherent limitations of the RANS approach.

Key findings of the study include:

- The SSTLM model showed reasonable accuracy in predicting streamwise velocity on the retreating side of the turbine rotation, closely aligning with the experimental measurements. The SA model also exhibited noticeably fewer discrepancies compared to the SST models.
- All models demonstrated less satisfactory performances on the advancing side of the turbine rotation compared to experimental data. The latter revealed distinct asymmetry in the wake, which was not captured by the models. Beyond a certain downstream

distance, all models overpredicted the velocity deficit, contrasting with experimental data that indicated wake recovery.

- Discrepancies between the models and experimental data were attributed to factors such as geometrical simplifications in the simulations, differences in averaging methods, and limitations of 2D modeling that do not account for 3D effects (tip vortices) and vertical motions that have a significant role in wake recovery.
- To accurately account for these effects, at least 3D simulations are required. However, such simulations require significant computational resources.
- Conflicting theories in the literature regarding wake asymmetry causes were noted.

Overall, it is important to recognize that CFD modeling of the aerodynamics of VAWTs at low TSRs using sliding meshes, even in 2D, demands a significant amount of computing resources. This requirement primarily stems from the need for detailed mesh refinements around the blades, shaft and within the rotor region. The mesh refinements in the rotor region are essential to minimize numerical diffusion, mainly because this area is characterized by the presence of shed vortices. Capturing the convection of these vortices and their interactions with the passing blades in the downstream region of the rotation is essential for accurate simulations. Reflecting this, the numerical simulations carried out in this thesis consumed approximately 280 core-years of CPU time on the Digital Research Alliance of Canada clusters.

5.2 Limitations

While the present research has provided insights into the aerodynamics of VAWTs, the following points highlight the limitations of the studies:

- The use of 2D URANS simulations in the present work may not wholly represent the complex flow structures such as the dynamic stall phenomenon, which is inherently 3D in nature.
- The study's findings are specific to the tested conditions and configurations and may require further validation for different VAWT designs and environments.
- The experimental setup, particularly the PIV, might not replicate all operational conditions of large, commercial-scale VAWTs.

5.3 Perspectives

Future research in this field could focus on the following aspects to further advance the study of VAWTs and address the current limitations:

- To address the limitations of 2D URANS simulations, future research should consider 3D simulations.
- Future studies should explore high-fidelity turbulence modeling, including hybrid RANS/LES approaches.
- Expanding research to include a variety of VAWT designs and operational conditions, including fluctuating turbulent flows and skewed flows, among others.
- Further studies are necessary to enhance our understanding of VAWTs operating at low Reynolds numbers, where the transition from laminar to turbulent flow plays a significant role.
- Integrating CFD computations with optimization algorithms to create novel airfoil designs for VAWTs.
- Addressing the scalability issues with OpenFOAM linear solvers is important. Exploring and integrating advanced linear solvers from highly optimized external libraries could substantially reduce the extensive time demands associated with simulations.

Bibliography

[1] International Energy Agency. World Energy Outlook 2022. 2022.

[2] Energy Institute. Statistical Review of World Energy. 2023.

[3] Global Wind Energy Council. Global Wind Report 2024. 2024.

[4] Erik Möllerström. Vertical Axis Wind Turbines Tower Dynamics and Noise. Master's thesis. Uppsala University, 2015.

[5] Belabes B, Paraschivoiu M. Numerical study of the effect of turbulence intensity on VAWT performance. Energy 2021;233:121139. https://doi.org/10.1016/j.energy.2021.121139.

[6] Carbó Molina A, De Troyer T, Massai T, Vergaerde A, Runacres MC, Bartoli G. Effect of turbulence on the performance of VAWTs: An experimental study in two different wind tunnels. Journal of Wind Engineering and Industrial Aerodynamics 2019;193. https://doi.org/10.1016/j.jweia.2019.103969.

[7] Peng HY, Lam HF, Liu HJ. Power performance assessment of H-rotor vertical axis wind turbines with different aspect ratios in turbulent flows via experiments. Energy 2019;173:121–32. https://doi.org/10.1016/j.energy.2019.01.140.

[8] Fields J, Oteri F, Preus R, Baring-Gould I. Deployment of Wind Turbines in the Built Environment: Risks, Lessons, and Recommended Practices. 2016. https://doi.org/10.2172/1260340.

[9] Mertens S, van Kuik G a. M, van Bussel GJW. Performance of an H-Darrieus in the Skewed Flow on a Roof. Journal of Solar Energy Engineering 2003;125:433. https://doi.org/10.1115/1.1629309.

[10] Du L, Ingram G, Dominy RG. A review of H-Darrieus wind turbine aerodynamic research. Proceedings of the Institution of Mechanical Engineers, Part C: Journal of Mechanical Engineering Science 2019;233:7590–616. https://doi.org/10.1177/0954406219885962.

[11] Dabiri JO. Potential order-of-magnitude enhancement of wind farm power density via counter-rotating vertical-axis wind turbine arrays. Journal of Renewable and Sustainable Energy 2011;3:043104. https://doi.org/10.1063/1.3608170.

[12] Tong W, editor. Wind power generation and wind turbine design. Southampton ; Boston: WIT Press; 2010.

[13] Hand B, Cashman A. A review on the historical development of the lift-type vertical axis wind turbine: From onshore to offshore floating application. Sustainable Energy Technologies and Assessments 2020;38:100646. https://doi.org/10.1016/j.seta.2020.100646.

[14] Borg M, Shires A, Collu M. Offshore floating vertical axis wind turbines, dynamics modelling state of the art. part I: Aerodynamics. Renewable and Sustainable Energy Reviews 2014;39:1214–25. https://doi.org/10.1016/j.rser.2014.07.096.

[15] Möllerström E, Gipe P, Beurskens J, Ottermo F. A historical review of vertical axis wind turbines rated 100 kW and above. Renewable and Sustainable Energy Reviews 2019;105:1–13. https://doi.org/10.1016/j.rser.2018.12.022.

[16] D.A.M. De Tavernier. Aerodynamic advances in vertical-axis wind turbines. Doctoral Dissertation. TU Delft University, 2021.

[17] QuietRevolution. QR6 Vertical Axis Wind Turbine 2020.

[18] Chen W-L, Li Z-C, Lin Y-S, Huang B-X. Control and performance identification for small vertical axis wind turbines. IET Conference on Renewable Power Generation (RPG 2011) 2011:5. https://doi.org/10.1049/cp.2011.0210.

[19] Buchner AJ, Soria J, Honnery D, Smits AJ. Dynamic stall in vertical axis wind turbines: Scaling and topological considerations. Journal of Fluid Mechanics 2018;841:746–66. https://doi.org/10.1017/jfm.2018.112.

[20] Leishman JG. Principles of Helicopter Aerodynamics. Cambridge University Press; 2006.

[21] Simão Ferreira CJ, Van Zuijlen A, Bijl H, Van Bussel G, Van Kuik G. Simulating dynamic stall in a two-dimensional vertical-axis wind turbine: verification and validation with particle image velocimetry data. Wind Energy 2010;13:1–17. https://doi.org/10.1002/we.330.

[22] Laneville A, Vittecoq P. Dynamic Stall: The Case of the Vertical Axis Wind Turbine. Journal of Solar Energy Engineering 1986;108:140. https://doi.org/10.1115/1.3268081.

[23] Beaudet L. Etude expérimentale et numérique du décrochage dynamique sur une éolienne à axe vertical de forte solidité. Doctoral Dissertation. Universite de Poitiers, 2014.

[24] Glauert H. The Elements of Aerofoil and Airscrew Theory. 2nd ed. Cambridge University Press; 1948.

[25] Templin RJ. Aerodynamic performance theory for the NRC vertical-axis wind turbine. National Aeronautical Establishment, Ottawa, Ontario (Canada); 1974.

[26] Thé J, Yu H. A critical review on the simulations of wind turbine aerodynamics focusing on hybrid RANS-LES methods. Energy 2017;138:257–89. https://doi.org/10.1016/j.energy.2017.07.028.

[27] Wilson RE, Lissaman PBS. Applied aerodynamics of wind power machines. Department of Mechanical Engineering, Oregon State University; 1974.

[28] Strickland JH. The Darrieus Turbine: A Performance Prediction Model Using Multiple Streamtubes. Sandia Labs., Albuquerque, N.Mex.; 1975.

[29] Lapin EE. Theoretical performance of vertical axis wind turbines, Houston: 1975.

[30] Paraschivoiu I. Double-multiple streamtube model for Darrieus in turbines. In 2nd DOE/NASA Wind Turbine Dynamics Workshop, 1981.

[31] Paraschivoiu I, Fraunie P, Beguier C. Streamtube expansion effects on the Darrieus wind turbine. Journal of Propulsion and Power 1985;1:150–5. https://doi.org/10.2514/3.22773.

[32] Bedon G, Antonini EGA, De Betta S, Raciti Castelli M, Benini E. Evaluation of the different aerodynamic databases for vertical axis wind turbine simulations. Renewable and Sustainable Energy Reviews 2014;40:386–99. https://doi.org/10.1016/j.rser.2014.07.126.

[33] Simão Ferreira CJ. The near wake of the VAWT: 2D and 3D views of the VAWT aerodynamics. Doctoral Dissertation. Delft University of Technology, 2009.

[34] Hirsch IrH, Mandal AC. A Cascade Theory for the Aerodynamic Performance of Darrieus Wind Turbines. Wind Engineering 1987;11:164–75.

[35] Mandal AC, Burton JD. The Effects of Dynamic Stall and Flow Curvature on the Aerodynamics of Darrieus Turbines Applying the Cascade Model. Wind Engineering 1994;18:267–82.

[36] Islam M, Ting DSKK, Fartaj A. Aerodynamic models for Darrieus-type straight-bladed vertical axis wind turbines. Renewable and Sustainable Energy Reviews 2008;12:1087–109. https://doi.org/10.1016/j.rser.2006.10.023.

[37] Snel H. Review of the present status of rotor aerodynamics. Wind Energy 1998;1:46–69. https://doi.org/10.1002/(SICI)1099-1824(199804)1:1+<46::AID-WE3>3.3.CO;2-0.

[38] Leishman J. Challenges in modeling the unsteady aerodynamics of wind turbines. 2002 ASME Wind Energy Symposium, vol. 79, Reston, Virigina: American Institute of Aeronautics and Astronautics; 2002, p. 219–385. https://doi.org/10.2514/6.2002-37.

[39] Larsen HC. Summary of a vortex theory for the cyclogiro. In: Proceedings of the 2nd US national conferences on wind engineering research, Colorado State University: Colorado State University; 1975.

[40] Fanucci J, Walter R. Innovative wind machines: the theoretical performance of a vertical-axis wind turbine. In: Proceedings of the vertical-axis wind turbine technology workshop, vol. 3, USA: 1976, p. 61–95.

[41] Wilson RE. Wind-turbine aerodynamics. Journal of Wind Engineering and Industrial Aerodynamics 1980;5:357–72. https://doi.org/10.1016/0167-6105(80)90042-2.

[42] Strickland JH, Webster BT, Nguyen T. A Vortex Model of the Darrieus Turbine: An Analytical and Experimental Study. Journal of Fluids Engineering 1979;101:500–5. https://doi.org/10.1115/1.3449018.

[43] Strickland JH, Smith T, Sun K. A Vortex Model of the Darrieus Turbine: An Analytical and Experimental Study. Sandia National Laboratory; 1981.

[44] Cardona JL. Flow Curvature and Dynamic Stall Simulated with an Aerodynamic Free-Vortex Model for VAWT. Wind Engineering 1984;8:135–43.

[45] Jin X, Zhao G, Gao K, Ju W. Darrieus vertical axis wind turbine: Basic research methods. Renewable and Sustainable Energy Reviews 2015;42:212–25. https://doi.org/10.1016/j.rser.2014.10.021.

[46] Durbin PA. Some Recent Developments in Turbulence Closure Modeling. Annual Review of Fluid Mechanics 2018;50:77–103. https://doi.org/10.1146/annurev-fluid-122316-045020.

[47] Menter F, Hüppe A, Matyushenko A, Kolmogorov D. An Overview of Hybrid RANS–LES Models Developed for Industrial CFD. Applied Sciences 2021;11:2459. https://doi.org/10.3390/app11062459.

[48] Larsson J, Kawai S, Bodart J, Bermejo-Moreno I. Large eddy simulation with modeled wall-stress: recent progress and future directions. Mechanical Engineering Reviews 2016;3:15-00418-15–00418. https://doi.org/10.1299/mer.15-00418.

[49] Barnes A, Marshall-Cross D, Hughes BR. Towards a standard approach for future Vertical Axis Wind Turbine aerodynamics research and development. Renewable and Sustainable Energy Reviews 2021;148:111221. https://doi.org/10.1016/j.rser.2021.111221.

[50] Fertahi S ed-Dîn, Belhadad T, Kanna A, Samaouali A, Kadiri I, Benini E. A Critical Review of CFD Modeling Approaches for Darrieus Turbines: Assessing Discrepancies in Power Coefficient Estimation and Wake Vortex Development. Fluids 2023;8:242. https://doi.org/10.3390/fluids8090242.

[51] He J, Jin X, Xie S, Cao L, Wang Y, Lin Y, et al. CFD modeling of varying complexity for aerodynamic analysis of H-vertical axis wind turbines. Renewable Energy 2020;145:2658–70. https://doi.org/10.1016/j.renene.2019.07.132.

[52] Li Y, Yang S, Feng F, Tagawa K. A review on numerical simulation based on CFD technology of aerodynamic characteristics of straight-bladed vertical axis wind turbines. Energy Reports 2023;9:4360–79. https://doi.org/10.1016/j.egyr.2023.03.082.

[53] Bachant P, Goude A, Wosnik M. Actuator line modeling of vertical-axis turbines 2016:1–21.

[54] Amet E, Maître T, Pellone C, Achard JL. 2D numerical simulations of blade-vortex interaction in a darrieus turbine. Journal of Fluids Engineering, Transactions of the ASME 2009;131:1111031–11110315. https://doi.org/10.1115/1.4000258.

[55] Howell R, Qin N, Edwards J, Durrani N. Wind tunnel and numerical study of a small vertical axis wind turbine. Renewable Energy 2010;35:412–22. https://doi.org/10.1016/j.renene.2009.07.025.

[56] Untaroiu A, Wood HG, Allaire PE, Ribando RJ. Investigation of Self-Starting Capability of Vertical Axis Wind Turbines Using a Computational Fluid Dynamics Approach. Journal of Solar Energy Engineering 2011;133:041010. https://doi.org/10.1115/1.4004705.

[57] Raciti Castelli M, Englaro A, Benini E. The Darrieus wind turbine: Proposal for a new performance prediction model based on CFD. Energy 2011;36:4919–34. https://doi.org/10.1016/j.energy.2011.05.036.

[58] Mohamed MH. Performance investigation of H-rotor Darrieus turbine with new airfoil shapes. Energy 2012;47:522–30. https://doi.org/10.1016/j.energy.2012.08.044.

[59] Mohamed MH. Aero-acoustics noise evaluation of H-rotor Darrieus wind turbines. Energy 2014;65:596–604. https://doi.org/10.1016/j.energy.2013.11.031.

[60] Daróczy L, Janiga G, Petrasch K, Webner M, Thévenin D. Comparative analysis of turbulence models for the aerodynamic simulation of H-Darrieus rotors. Energy 2015;90:680–90. https://doi.org/10.1016/j.energy.2015.07.102.

[61] Lee YT, Lim HC. Numerical study of the aerodynamic performance of a 500W Darrieus-type vertical-axis wind turbine. Renewable Energy 2015;83:407–15. https://doi.org/10.1016/j.renene.2015.04.043.

[62] Joo S, Choi H, Lee J. Aerodynamic characteristics of two-bladed H-Darrieus at various solidities and rotating speeds. Energy 2015;90:439–51. https://doi.org/10.1016/j.energy.2015.07.051.

[63] Edwards JM, Angelo Danao L, Howell RJ. Novel Experimental Power Curve Determination and Computational Methods for the Performance Analysis of Vertical Axis Wind Turbines. Journal of Solar Energy Engineering 2012;134:031008. https://doi.org/10.1115/1.4006196.

[64] Castelli MR, Dal Monte A, Quaresimin M, Benini E. Numerical evaluation of aerodynamic and inertial contributions to Darrieus wind turbine blade deformation. Renewable Energy 2013;51:101–12. https://doi.org/10.1016/j.renene.2012.07.025.

[65] Danao LA, Edwards J, Eboibi O, Howell R. A numerical investigation into the influence of unsteady wind on the performance and aerodynamics of a vertical axis wind turbine. Applied Energy 2014;116:111–24. https://doi.org/10.1016/j.apenergy.2013.11.045.

[66] Almohammadi KM, Ingham DB, Ma L, Pourkashanian M. Modeling dynamic stall of a straight blade vertical axis wind turbine. Journal of Fluids and Structures 2015;57:144–58. https://doi.org/10.1016/j.jfluidstructs.2015.06.003.

[67] Bhargav MMSRS, Ratna Kishore V, Laxman V. Influence of fluctuating wind conditions on vertical axis wind turbine using a three dimensional CFD model. Journal of Wind Engineering and Industrial Aerodynamics 2016;158:98–108. https://doi.org/10.1016/j.jweia.2016.10.001.

[68] Meana-Fernández A, Solís-Gallego I, Fernández Oro JM, Argüelles Díaz KM, Velarde-Suárez S. Parametrical evaluation of the aerodynamic performance of vertical axis wind turbines for the proposal of optimized designs. Energy 2018;147:504–17. https://doi.org/10.1016/j.energy.2018.01.062.

[69] McLaren K, Tullis S, Ziada S. Computational fluid dynamics simulation of the aerodynamics of a high solidity, small-scale vertical axis wind turbine: CFD simulation

of the aerodynamics of a high solidity VAWT. Wind Energ 2012;15:349–61. https://doi.org/10.1002/we.472.

[70] Rossetti A, Pavesi G. Comparison of different numerical approaches to the study of the H-Darrieus turbines start-up. Renewable Energy 2013;50:7–19. https://doi.org/10.1016/j.renene.2012.06.025.

[71] Lam HF, Peng HY. Study of wake characteristics of a vertical axis wind turbine by two- and three-dimensional computational fluid dynamics simulations. Renewable Energy 2016;90:386–98. https://doi.org/10.1016/j.renene.2016.01.011.

[72] Arab A, Javadi M, Anbarsooz M, Moghiman M. A numerical study on the aerodynamic performance and the self-starting characteristics of a Darrieus wind turbine considering its moment of inertia. Renewable Energy 2017;107:298–311. https://doi.org/10.1016/j.renene.2017.02.013.

[73] Balduzzi F, Drofelnik J, Bianchini A, Ferrara G, Ferrari L, Campobasso MS. Darrieus wind turbine blade unsteady aerodynamics: a three-dimensional Navier-Stokes CFD assessment. Energy 2017;128:550–63. https://doi.org/10.1016/j.energy.2017.04.017.

[74] Rezaeiha A, Kalkman I, Blocken B. CFD simulation of a vertical axis wind turbine operating at a moderate tip speed ratio: Guidelines for minimum domain size and azimuthal increment. Renewable Energy 2017;107:373–85. https://doi.org/10.1016/j.renene.2017.02.006.

[75] Wekesa DW, Wang C, Wei Y, Danao LAM. Analytical and numerical investigation of unsteady wind for enhanced energy capture in a fluctuating free-stream. Energy 2017;121:854–64. https://doi.org/10.1016/j.energy.2017.01.041.

[76] Rezaeiha A, Montazeri H, Blocken B. Towards accurate CFD simulations of vertical axis wind turbines at different tip speed ratios and solidities: Guidelines for azimuthal increment, domain size and convergence. Energy Conversion and Management 2018;156:301–16. https://doi.org/10.1016/j.enconman.2017.11.026.

[77] Rezaeiha A, Montazeri H, Blocken B. Characterization of aerodynamic performance of vertical axis wind turbines: Impact of operational parameters. Energy Conversion and Management 2018;169:45–77. https://doi.org/10.1016/j.enconman.2018.05.042.

[78] Zhu C, Yang H, Qiu Y, Zhou G, Wang L, Feng Y, et al. Effects of the Reynolds number and reduced frequency on the aerodynamic performance and dynamic stall behaviors of a vertical axis wind turbine. Energy Conversion and Management 2023;293:117513. https://doi.org/10.1016/j.enconman.2023.117513.

[79] Li C, Zhu S, Xu Y-L, Xiao Y. 2.5D large eddy simulation of vertical axis wind turbine in consideration of high angle of attack flow. Renewable Energy 2013;51:317–30. https://doi.org/10.1016/j.renene.2012.09.011.

[80] Ghasemian M, Nejat A. Aero-acoustics prediction of a vertical axis wind turbine using Large Eddy Simulation and acoustic analogy. Energy 2015;88:711–7. https://doi.org/10.1016/j.energy.2015.05.098.

[81] Peng HY, Lam HF. Turbulence effects on the wake characteristics and aerodynamic performance of a straight-bladed vertical axis wind turbine by wind tunnel tests and large eddy simulations. Energy 2016;109:557–68. https://doi.org/10.1016/j.energy.2016.04.100.

[82] Lei H, Zhou D, Bao Y, Li Y, Han Z. Three-dimensional Improved Delayed Detached Eddy Simulation of a two-bladed vertical axis wind turbine. Energy Conversion and Management 2017;133:235–48. https://doi.org/10.1016/j.enconman.2016.11.067.

[83] Patil R, Daróczy L, Janiga G, Thévenin D. Large eddy simulation of an H-Darrieus rotor. Energy 2018;160:388–98. https://doi.org/10.1016/j.energy.2018.06.203.

[84] Migliore PG, Wolfe WP, Fanucci JB. Flow Curvature Effects on Darrieus Turbine Blade Aerodynamics. Journal of Energy 1980;4:49–55. https://doi.org/10.2514/3.62459.

[85] Geng F, Kalkman I, Suiker ASJ, Blocken B. Sensitivity analysis of airfoil aerodynamics during pitching motion at a Reynolds number of 1.35×105. Journal of Wind Engineering and Industrial Aerodynamics 2018;183:315–32. https://doi.org/10.1016/j.jweia.2018.11.009.

[86] McNaughton J, Billard F, Revell A. Turbulence modelling of low Reynolds number flow effects around a vertical axis turbine at a range of tip-speed ratios. Journal of Fluids and Structures 2014;47:124–38. https://doi.org/10.1016/j.jfluidstructs.2013.12.014.

[87] Leishman JG. Challenges in modelling the unsteady aerodynamics of wind turbines. Wind Energy 2002;5:85–132. https://doi.org/10.1002/we.62.

[88] Carr LW, Mcalister KW, Mccroskey WJ. Analysis of the development of dynamic stall based on oscillating airfoil experiments. 1977.

[89] McCroskey WJ, McAlister KW, Carr LW, Pucci SL, Lambert O, Indergrand RF. Dynamic Stall on Advanced Airfoil Sections. Journal of the American Helicopter Society 1981;26:40–50. https://doi.org/10.4050/jahs.26.40.

[90] Gharali K, Gharaei E, Soltani M, Raahemifar K. Reduced frequency effects on combined oscillations, angle of attack and free stream oscillations, for a wind turbine blade element. Renewable Energy 2018;115:252–9. https://doi.org/10.1016/j.renene.2017.08.042.

[91] Thakor M, Kumar G, Das D, De A. Investigation of asymmetrically pitching airfoil at high reduced frequency. Physics of Fluids 2020;32:053607. https://doi.org/10.1063/5.0006659.

[92] Sangwan J, Sengupta TK, Suchandra P. Investigation of compressibility effects on dynamic stall of pitching airfoil. Physics of Fluids 2017;29:076104. https://doi.org/10.1063/1.4995457.

[93] Lee T, Gerontakos P. Investigation of flow over an oscillating airfoil. Journal of Fluid Mechanics 2004;512:313–41. https://doi.org/10.1017/S0022112004009851.

[94] Piziali RA. 2-D and 3-D Oscillating Wing Aerodynamics for a Range of Angles of Attack Including Stall. National Aeronautics and Space Administration (NASA), Ames Research Center; 1994.

[95] Lee T, Su YY. Surface Pressures Developed on an Airfoil Undergoing Heaving and Pitching Motion. Journal of Fluids Engineering 2015;137. https://doi.org/10.1115/1.4029443.

[96] Gharali K, Johnson DA. Dynamic stall simulation of a pitching airfoil under unsteady freestream velocity. Journal of Fluids and Structures 2013;42:228–44. https://doi.org/10.1016/j.jfluidstructs.2013.05.005.

[97] Gupta R, Ansell PJ. Investigation of the Effects of Reynolds Number on the Unsteady Flow Physics of Airfoil Dynamic Stall. 2018 AIAA Aerospace Sciences Meeting, American Institute of Aeronautics and Astronautics; 2018. https://doi.org/10.2514/6.2018-0354.

[98] Petot D. Differential equation modeling of dynamic stall. La Recherche Aerospatiale 1989:59–72.

[99] Tarzanin FJ. Prediction of Control Loads Due to Blade Stall. J Am Helicopter Soc 1972;17:33–46. https://doi.org/10.4050/JAHS.17.33.

[100] Leishman JG, Beddoes TS. A Semi-Empirical Model for Dynamic Stall. Journal of the American Helicopter Society 1989;Volume 34. https://doi.org/10.4050/JAHS.34.3.3.

[101] Ekaterinaris JA, Platzer MF. Computational prediction of airfoil dynamic stall. Progress in Aerospace Sciences 1998;33:759–846. https://doi.org/10.1016/S0376-0421(97)00012-2.

[102] Richez F. Analysis of Dynamic Stall Mechanisms in Helicopter Rotor Environment. J Am Helicopter Soc 2018;63:1–11. https://doi.org/10.4050/JAHS.63.022006.

[103] Hand B, Kelly G, Cashman A. Aerodynamic design and performance parameters of a lift-type vertical axis wind turbine: A comprehensive review. Renewable and Sustainable Energy Reviews 2021;139:110699. https://doi.org/10.1016/j.rser.2020.110699.

[104] Ramírez L, Foulquié C, Nogueira X, Khelladi S, Chassaing J-C, Colominas I. New high-resolution-preserving sliding mesh techniques for higher-order finite volume schemes. Computers & Fluids 2015;118:114–30. https://doi.org/10.1016/j.compfluid.2015.06.008.

[105] Zhang B, Liang C. A simple, efficient, and high-order accurate curved sliding-mesh interface approach to spectral difference method on coupled rotating and stationary domains. Journal of Computational Physics 2015;295:147–60. https://doi.org/10.1016/j.jcp.2015.04.006.

[106] Jasak H. Dynamic Mesh Handling in OpenFOAM. 47th AIAA Aerospace Sciences Meeting including The New Horizons Forum and Aerospace Exposition, American Institute of Aeronautics and Astronautics; 2009. https://doi.org/10.2514/6.2009-341.

[107] Ouchene S, Smaili A, Fellouah H. Assessment of Turbulence Models for Unsteady Separated Flows Past an Oscillating NACA 0015 Airfoil in Deep Stall. Journal of Applied Fluid Mechanics 2023;16:1544–59. https://doi.org/10.47176/jafm.16.08.1718.

[108] Durbin PA, Reif BAP. Statistical Theory and Modeling for Turbulent Flows. 1st ed. Wiley; 2010. https://doi.org/10.1002/9780470972076.

[109] Wilcox DC. Turbulence modeling for CFD. 3rd ed. La Cãnada, Calif: DCW Industries; 2006.

[110] Cress J, Gordeyev S, Jumper E. Aero-Optical Measurements in a Heated, Subsonic, Turbulent Boundary Layer. 48th AIAA Aerospace Sciences Meeting Including the New Horizons Forum and Aerospace Exposition, Orlando, Florida: American Institute of Aeronautics and Astronautics; 2010. https://doi.org/10.2514/6.2010-434.

[111] Davidson PA. Turbulence: an introduction for scientists and engineers. Second edition. Oxford, United Kingdom ; New York, NY, United States of America: Oxford University Press; 2015.

[112] Menter FR. Review of the shear-stress transport turbulence model experience from an industrial perspective. International Journal of Computational Fluid Dynamics 2009;23:305–16. https://doi.org/10.1080/10618560902773387.

[113] Spalart P, Allmaras S. A one-equation turbulence model for aerodynamic flows. Recherche Aerospatiale 1994;1:5–21.

[114] Spalart PR, Rumsey CL. Effective Inflow Conditions for Turbulence Models in Aerodynamic Calculations. AIAA Journal 2007;45:2544–53. https://doi.org/10.2514/1.29373.

[115] Rumsey CL. Apparent transition behavior of widely-used turbulence models. International Journal of Heat and Fluid Flow 2007;28:1460–71. https://doi.org/10.1016/j.ijheatfluidflow.2007.04.003.

[116] Jones WP, Launder BE. The prediction of laminarization with a two-equation model of turbulence. International Journal of Heat and Mass Transfer 1972;15:301–14. https://doi.org/10.1016/0017-9310(72)90076-2.

[117] Patel VC, Rodi W, Scheuerer G. Turbulence models for near-wall and low Reynolds number flows - A review. AIAA Journal 1985;23:1308–19. https://doi.org/10.2514/3.9086.

[118] Launder BE, Sharma BI. Application of the energy-dissipation model of turbulence to the calculation of flow near a spinning disc. Letters in Heat and Mass Transfer 1974;1:131–7. https://doi.org/10.1016/0094-4548(74)90150-7.

[119] Menter FR. Two-equation eddy-viscosity turbulence models for engineering applications. AIAA Journal 1994;32:1598–605. https://doi.org/10.2514/3.12149.

[120] Menter FR, Kuntz M, Langtry R. Ten Years of Industrial Experience with the SST Turbulence Model. Heat and Mass Transfer, 2003.

[121] Langtry RB, Menter FR. Correlation-Based Transition Modeling for Unstructured Parallelized Computational Fluid Dynamics Codes. AIAA Journal 2009;47:2894–906. https://doi.org/10.2514/1.42362.

[122] Wang S, Ingham DB, Ma L, Pourkashanian M, Tao Z. Numerical investigations on dynamic stall of low Reynolds number flow around oscillating airfoils. Computers and Fluids 2010;39:1529–41. https://doi.org/10.1016/j.compfluid.2010.05.004.

[123] Leishman JG. Dynamic stall experiments on the NACA 23012 aerofoil. Experiments in Fluids 1990;9:49–58. https://doi.org/10.1007/BF00575335.

[124] Gerakopulos R, Boutilier M, Yarusevych S. Aerodynamic Characterization of a NACA 0018 Airfoil at Low Reynolds Numbers. 40th Fluid Dynamics Conference and Exhibit, Chicago, Illinois: American Institute of Aeronautics and Astronautics; 2010. https://doi.org/10.2514/6.2010-4629.

[125] Wang S, Ingham DB, Ma L, Pourkashanian M, Tao Z. Turbulence modeling of deep dynamic stall at relatively low Reynolds number. Journal of Fluids and Structures 2012;33:191–209. https://doi.org/10.1016/j.jfluidstructs.2012.04.011.

[126] Rhee M. Evaluation of grid convergence and turbulence model constant changes for the airfoil flow simulation. Collection of Technical Papers - 45th AIAA Aerospace Sciences Meeting, vol. 19, 2007, p. 13037–60. https://doi.org/10.2514/6.2007-1082.

[127] Sharma A, Visbal M. Numerical investigation of the effect of airfoil thickness on onset of dynamic stall. Journal of Fluid Mechanics 2019;870:870–900. https://doi.org/10.1017/jfm.2019.235.

[128] OpenCFD ESI. OpenFOAM v2212 User Guide. 2022.

[129] Chan WM, Steger JL. Enhancements of a three-dimensional hyperbolic grid generation scheme. Applied Mathematics and Computation 1992;51:181–205. https://doi.org/10.1016/0096-3003(92)90073-A.

[130] Bos FM, Oudheusden BWV, Bijl H. Radial basis function based mesh deformation applied to simulation of flow around flapping wings. Computers and Fluids 2013;79:167–77. https://doi.org/10.1016/j.compfluid.2013.02.004.

[131] Storms BL, Ross JC, Heineck JT, Walker SM, Driver DM, Zilliac GG. An Experimental Study of the Ground Transportation System (GTS) Model in the NASA Ames 7-by 10-Ft Wind Tunnel. National Aeronautics and Space Administration (NASA), Ames Research Center; 2001.

[132] Carr LW, Chandrasekhara MS. Compressibility effects on dynamic stall. Progress in Aerospace Sciences 1996;32:523–73. https://doi.org/10.1016/0376-0421(95)00009-7.

[133] Corke TC, Thomas FO. Dynamic stall in pitching airfoils: Aerodynamic damping and compressibility effects. Annual Review of Fluid Mechanics 2015;47:479–505. https://doi.org/10.1146/annurev-fluid-010814-013632.

[134] Issa RI. Solution of the implicitly discretised fluid flow equations by operator-splitting. Journal of Computational Physics 1986;62:40–65. https://doi.org/10.1016/0021-9991(86)90099-9.

[135] Patankar SV, Spalding DB. A calculation procedure for heat, mass and momentum transfer in three-dimensional parabolic flows. International Journal of Heat and Mass Transfer 1972;15:1787–806. https://doi.org/10.1016/0017-9310(72)90054-3.

[136] Gardner AD, Jones AR, Mulleners K, Naughton JW, Smith MJ. Review of rotating wing dynamic stall: Experiments and flow control. Progress in Aerospace Sciences 2023;137:100887. https://doi.org/10.1016/j.paerosci.2023.100887.

[137] Melani PF, Balduzzi F, Ferrara G, Bianchini A. How to extract the angle attack on airfoils in cycloidal motion from a flow field solved with computational fluid dynamics? Development and verification of a robust computational procedure. Energy Conversion and Management 2020;223:113284. https://doi.org/10.1016/j.enconman.2020.113284.

[138] Bianchini A, Balduzzi F, Ferrara G, Ferrari L. A computational procedure to define the incidence angle on airfoils rotating around an axis orthogonal to flow direction. Energy Conversion and Management 2016;126:790–8. https://doi.org/10.1016/j.enconman.2016.08.010.

[139] Gosselin R. Analysis and optimization of vertical axis turbines. Doctoral Dissertation. Université Laval, 2015.

[140] Elsakka MM, Ingham DB, Ma L, Pourkashanian M. CFD analysis of the angle of attack for a vertical axis wind turbine blade. Energy Conversion and Management 2019;182:154–65. https://doi.org/10.1016/j.enconman.2018.12.054.

[141] Ouchene S, Smaili A, Fellouah H. On the estimation of the angle of attack for vertical axis wind turbines. International Journal of Numerical Methods for Heat & Fluid Flow 2023;ahead-of-print. https://doi.org/10.1108/HFF-09-2022-0566.

[142] Rezaeiha A, Kalkman I, Blocken B. Effect of pitch angle on power performance and aerodynamics of a vertical axis wind turbine. Applied Energy 2017;197:132–50. https://doi.org/10.1016/j.apenergy.2017.03.128.

[143] Drela M. XFOIL: An Analysis and Design System for Low Reynolds Number Airfoils. Low Reynolds Number Aerodynamics, vol. 54, Berlin, Heidelberg: Springer Berlin Heidelberg; 1989, p. 1–12. https://doi.org/10.1007/978-3-642-84010-4_1.

[144] Coder JG. Further Development of the Amplification Factor Transport Transition Model for Aerodynamic Flows. AIAA Scitech 2019 Forum, San Diego, California: American Institute of Aeronautics and Astronautics; 2019. https://doi.org/10.2514/6.2019-0039.

[145] Adams AS, Keith DW. Are global wind power resource estimates overstated? Environ Res Lett 2013;8:015021. https://doi.org/10.1088/1748-9326/8/1/015021.

[146] Brownstein ID, Kinzel M, Dabiri JO. Performance enhancement of downstream vertical-axis wind turbines. Journal of Renewable and Sustainable Energy 2016;8:053306. https://doi.org/10.1063/1.4964311.

[147] Scherl I, Strom B, Brunton SL, Polagye BL. Geometric and control optimization of a two cross-flow turbine array. Journal of Renewable and Sustainable Energy 2020;12:064501. https://doi.org/10.1063/5.0022428.

[148] La soufflerie aérodynamique | Laboratoire d'Ingénierie des Fluides et des Systèmes Énergétiques n.d. https://lifse.artsetmetiers.fr/infrastructure/la-soufflerie-aerodynamique (accessed August 7, 2023).

[149] Boutier A. Vélocimétrie laser pour la mécanique des fluides. Cachan: Hermès science publications-Lavoisier; 2012.

[150] Wang R, Xiao Z. Transition effects on flow characteristics around a static two-dimensional airfoil. Physics of Fluids 2020;32. https://doi.org/10.1063/1.5144860.

[151] McCroskey WJ. The Phenomenon of Dynamic Stall. Ames Research Center: National Aeronautics and Space Administration (NASA), Ames Research Center; 1981.

[152] Tseng C-C, Cheng Y-E. Numerical investigations of the vortex interactions for a flow over a pitching foil at different stages. Journal of Fluids and Structures 2015;58:291–318. https://doi.org/10.1016/j.jfluidstructs.2015.08.002.

[153] Rhee MJ. A Study of Dynamic Stall Vortex Development Using 2D Data from the AFDD Oscillating Wing Experiment. National Aeronautics and Space Administration (NASA), Ames Research Center; 2002.

[154] Visbal MR, Shang JS. Investigation of the flow structure around a rapidly pitching airfoil. AIAA Journal 1989;27:1044–51. https://doi.org/10.2514/3.10219.

[155] Jain S, Saha UK. On the influence of blade thickness-to-chord ratio on dynamic stall phenomenon in H-type Darrieus wind rotors. Energy Conversion and Management 2020;218:113024. https://doi.org/10.1016/j.enconman.2020.113024.

[156] Edwards JM. The Influence of Aerodynamic Stall on the Performance of Vertical Axis Wind Turbines. Doctoral Dissertation. University of Sheffield, 2012.

[157] LeBlanc B, Ferreira C. Estimation of blade loads for a variable pitch Vertical Axis Wind Turbine with strain gage measurements. Wind Energy 2022;25:1030–45. https://doi.org/10.1002/we.2713.

[158] Rezaeiha A, Kalkman I, Montazeri H, Blocken B. Effect of the shaft on the aerodynamic performance of urban vertical axis wind turbines. Energy Conversion and Management 2017;149:616–30. https://doi.org/10.1016/j.enconman.2017.07.055.

[159] Ramanujam G, Ozdemir H. Improving Airfoil Lift Prediction. 35th Wind Energy Symposium, American Institute of Aeronautics and Astronautics; 2017. https://doi.org/10.2514/6.2017-1999.

[160] Rival D, Manejev R, Tropea C. Measurement of parallel blade–vortex interaction at low Reynolds numbers. Exp Fluids 2010;49:89–99. https://doi.org/10.1007/s00348-009-0796-1.

[161] Peng D, Gregory JW. Vortex dynamics during blade-vortex interactions. Physics of Fluids 2015;27. https://doi.org/10.1063/1.4921449.

[162] Peng HY, Lam HF, Liu HJ. Numerical investigation into the blade and wake aerodynamics of an H-rotor vertical axis wind turbine. Journal of Renewable and Sustainable Energy 2018;10:053305. https://doi.org/10.1063/1.5040297.

[163] Bachant P, Wosnik M. Characterising the near-wake of a cross-flow turbine. Journal of Turbulence 2015;16:392–410. https://doi.org/10.1080/14685248.2014.1001852.

[164] Rezaeiha A, Montazeri H, Blocken B. On the accuracy of turbulence models for CFD simulations of vertical axis wind turbines. Energy 2019;180:838–57. https://doi.org/10.1016/j.energy.2019.05.053.

[165] Bianchini A, Balduzzi F, Bachant P, Ferrara G, Ferrari L. Effectiveness of two-dimensional CFD simulations for Darrieus VAWTs: a combined numerical and experimental assessment. Energy Conversion and Management 2017;136:318–28. https://doi.org/10.1016/j.enconman.2017.01.026.

[166] Araya DB, Colonius T, Dabiri JO. Transition to bluff-body dynamics in the wake of vertical-axis wind turbines. Journal of Fluid Mechanics 2017;813:346–81. https://doi.org/10.1017/jfm.2016.862.

[167] Hohman TC, Martinelli L, Smits AJ. The effects of inflow conditions on vertical axis wind turbine wake structure and performance. Journal of Wind Engineering and Industrial Aerodynamics 2018;183:1–18. https://doi.org/10.1016/j.jweia.2018.10.002.

[168] Strom B, Polagye B, Brunton SL. Near-wake dynamics of a vertical-axis turbine. J Fluid Mech 2022;935:A6. https://doi.org/10.1017/jfm.2021.1123.